UNIVERSITY OF ROCHESTER
LABORATORY FOR LASER ENERGETICS

Volume 125
October–December 2010
DOE/NA/28302-993

# LLE Review

## Quarterly Report

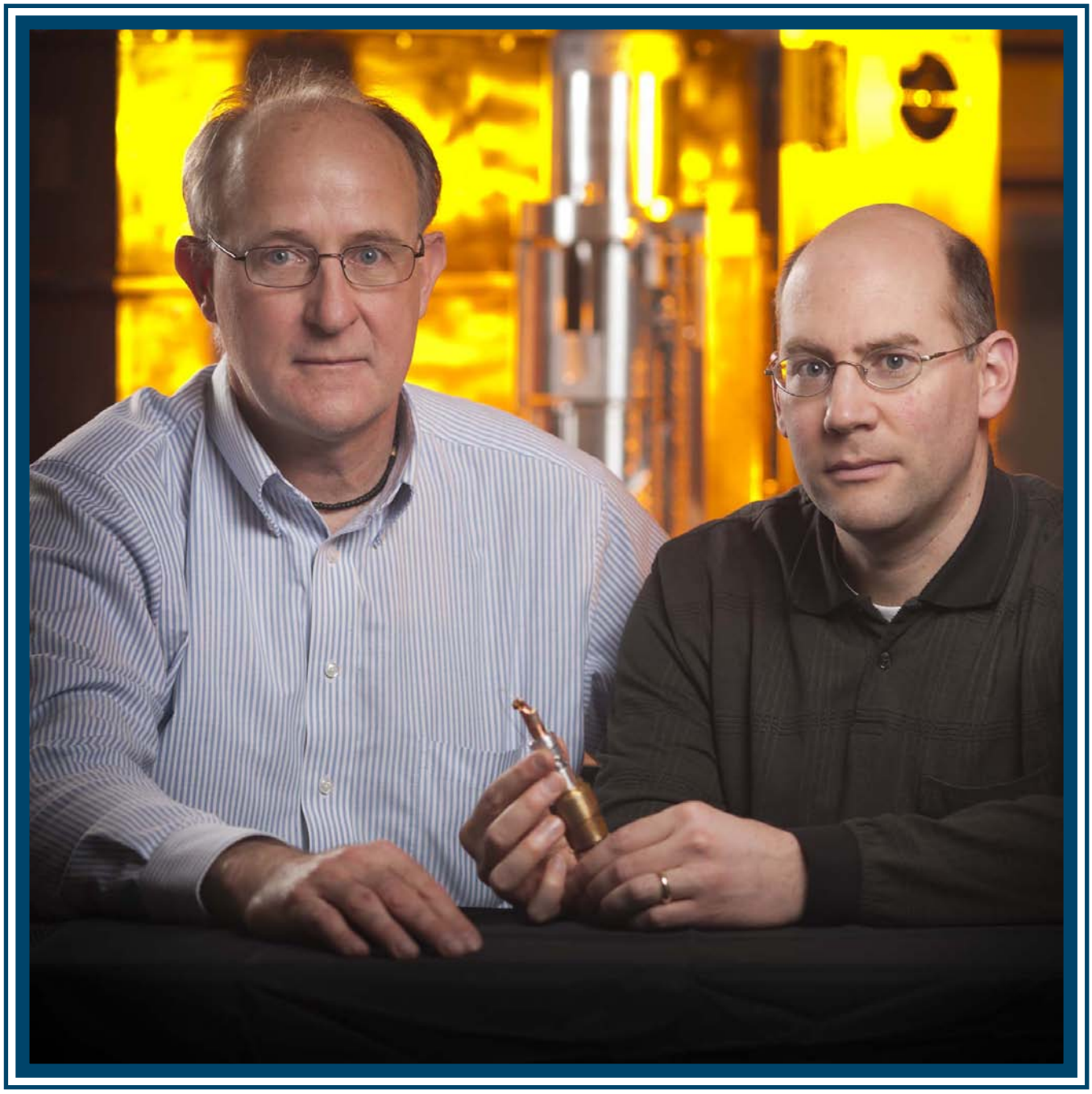

## About the Cover:

The cover photo shows Dr. Tom Boehly, the LLE Scientist who led the OMEGA shock-timing experiments reported on p. 1, and Mr. Mark Bonino, the Target Production Group Leader whose group built the targets, holding the assembly for a cryogenic cone-in-shell target. During experiments, this target assembly is installed on the moving cryostat seen in the background. These targets were used in the first experiments to time multiple, spherically converging shock waves in a liquid-deuterium–filled shell. These first experiments were performed on the OMEGA laser and demonstrated the ability to time and control shock waves to the precision needed for ignition experiments. This technique is currently being applied to hohlraum-driven ignition targets on the NIF.

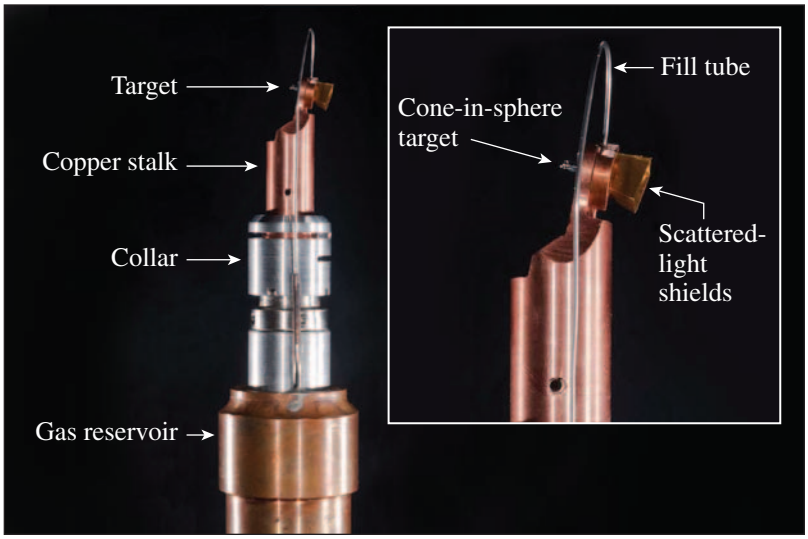


The photo at the left shows a target assembly for a cone-in-shell target used for shock-timing experiments. The 900-$\mu$m-diam CD shell has a re-entrant cone to provide access for VISAR to detect shocks in the deuterium contained within the shell. The cone is mounted on a copper stalk where the liquid deuterium is held at 19 K. It is a closed system utilizing a gas reservoir connected to the assembly through a large fill tube. The shields on the rear of the assembly protect the quartz VISAR window from scattered light and x rays that could photoionize the window material and cause it to become opaque.



The work described in this volume includes current research at the Laboratory for Laser Energetics, which is supported by New York State Energy Research and Development Authority, the University of Rochester, the U.S. Department of Energy Office of Inertial Confinement Fusion under Cooperative Agreement No. DE-FC52-08NA28302, and other agencies.

Printed in the United States of America
Available from
National Technical Information Services
U.S. Department of Commerce
5285 Port Royal Road
Springfield, VA 22161
www.ntis.gov

For questions or comments, contact Amy L. Rigatti, Editor, Laboratory for Laser Energetics, 250 East River Road, Rochester, NY 14623-1299, (585) 275-8016.
www.lle.rochester.edu

UNIVERSITY OF ROCHESTER
LABORATORY FOR LASER ENERGETICS

Volume 125
October–December 2010
DOE/NA/28302-993

# LLE Review

## Quarterly Report

UR LLE

## Contents

# In Brief

This volume of the LLE Review, covering October–December 2010, features "The Velocity and Timing of Multiple Spherically Converging Shock Waves in Liquid Deuterium" by T. R. Boehly, V. N. Goncharov, W. Seka, S. X. Hu, and J. A. Marozas (LLE); D. D. Meyerhofer (LLE and Departments of Mechanical Engineering and Physics, U. of Rochester); and P. M. Celliers, D. G. Hicks, G. W. Collins, and M. A. Barrios* [LLNL (*previously at LLE)]. In this article (p. 1), the authors report on experiments that measure the velocity and timing of multiple converging shock waves inside spherical targets filled with liquid (cryogenic) deuterium. The experiments were performed on the OMEGA Laser System and the velocity interferometry system for any reflector (VISAR) was used to detect a Doppler shift of an optical probe beam that reflects off the shock front. A streaked optical pyrometer (SOP) was also used to observe the optical self-emission from shocks in the deuterium, providing an independent measurement of shock timing. The results show that shock timing can be measured to better than the ±50-ps precision required for ignition targets and are best simulated when hydrodynamic codes use a nonlocal model for the transport of absorbed laser energy from the coronal plasma to the ablation surface. This technique is being directly applied to full-scale experiments to tune hohlraum-driven ignition targets on the NIF Laser System.

Additional highlights of research presented in this issue include the following:

- C. K. Li, F. H. Séguin, J. A. Frenje, M. J. Rosenberg, H. G. Rinderknecht, A. B. Zylstra, and R. D. Petrasso (Plasma Science and Fusion Center, MIT); P. A. Amendt, O. L. Landen, A. J. MacKinnon, R. P. J. Town, and S. C. Wilks (LLNL); R. Betti and D. D. Meyerhofer (LLE and Departments of Mechanical Engineering and Physics, U. of Rochester); J. M. Soures (LLE); and J. Hund, J. D. Kilkenny, and A. Nikroo (GA) present experimental data from OMEGA on the first time-gated proton radiography of the spatial structure and temporal evolution of how the fill gas compresses the wall-blowoff, inhibits plasma-jet formation, and impedes plasma stagnation in the hohlraum interior (p. 7). The results demonstrate the important roles of spontaneously generated electric and magnetic fields in the hohlraum dynamics and capsule implosion and provide novel insight into the effects of fill gas on x-ray–driven implosions. This will have an important impact on upcoming ignition experiments on the NIF.

- W. Theobald, A. A. Solodov, C. Stoeckl, K. S. Anderson, T. R. Boehly, R. S. Craxton, J. A. Delettrez, C. Dorrer, V. Yu. Glebov, J. P. Knauer, F. J. Marshall, K. L. Marshall, P. M. Nilson, T. C. Sangster, and W. Seka (LLE); R. Betti and D. D. Meyerhofer (LLE and Departments of Mechanical Engineering and Physics, U. of Rochester); J. A. Frenje and N. Sinenian (MIT); H. Habara and K. A. Tanaka (Osaka University, Japan); R. Lauck (Physikalisch-Technische Bundesanstalt, Germany); P. K. Patel and H. Chen (LLNL); T. Ma (LLNL and University of California, San Diego); F. N. Beg (University of California, San Diego); and E. Giraldez and R. B. Stephens (GA) report on the cone-in-shell fast-ignitor experiments conducted at the Omega Laser Facility using short-pulse OMEGA EP beams (p. 13). The cone-in-shell concept is a promising approach to bring the fast-electron source location as close as possible to the fuel assembly. The re-entrant cone allows for a high-energy petawatt laser pulse to propagate as close as possible to the dense core, avoiding the need to channel the laser beam through a large region of plasma material. For the smaller 10-$\mu$m tip diameter targets and a properly timed short-pulse, a factor-of-4 increase in neutron yield was observed by short-pulse heating in a narrow (~100-ps) time window close to peak compression. VISAR measurements show that the thicker cone wall (15-$\mu$m Au) targets used in the integrated shots are well shielded against x rays and are not affected by preheat. This work addresses a few key issues for fast ignition including cone survivability and the trade-off of matching the cone thickness to the fast-electron energy.

- S. Papernov, A. Tait, W. A. Bittle, A. W. Schmid, J. B. Oliver, and P. Kupinski (LLE) describe the use of photothermal heterodyne imaging (PHI) to evaluate the spatial distribution of absorbers in hafnia monolayers (p. 25). The metal-oxide layer is the weakest part of the thin-film coating and typically where damage is initiated. Insight into the nature and distribution of damage precursors is valuable to further improve the material's damage resistance. Gold nanoparticles embedded in a silica film were used to determine the system's resolution of ~5-nm particle size and an ~0.5-$\mu$m particle separation. PHI images of hafnia films prior to laser irradiation are structureless, pointing to absorber separations much smaller than the spatial resolution of this method. Using PHI data and atomic force microscopy mapping of damage-initiation sites, an upper limit for absorber separation was calculated to be ~0.1 $\mu$m. By comparing heterodyne signals for different film thicknesses, it was determined that hafnia/silica interfacial absorption is not a major factor in damage initiation, but the main contribution comes from absorption inside the hafnia film.

- A. S. Cross and R. Sobolewski (LLE); D. Kochanowska, M. Witkowska-Baran, and A. Mycielski (Polish Academy of Sciences, Poland); and M. Mikulics and D. Grützmacher (Jülich-Aachen Research Alliance, Germany) summarize the large tunable, terahertz electro-optic (EO) response in cadmium manganese telluride (Cd,Mn)Te single crystals (p. 33). This crystal is known as CMT and it is a well-studied semiconductor material because of its stable zinc-blend structure for high-Mn concentrations which provides a wide tuning range of the energy band gap. It exhibits a large magneto-optic Faraday effect and has a very high stopping power making it a great potential for x- and $\gamma$-ray detection. The measurements demonstrated CMT's exceptionally large EO Pockels effect and showed that the EO sensitivity can be magnified for a particular probe wavelength using band-gap engineering.

- M. J. Guardalben, L. J. Waxer, S.-W. Bahk, M. Barczys, C. Dorrer, E. Hill, and M Spilatro (LLE) review improvements to optimize the long-pulse, on-target energy of the OMEGA EP laser (p. 37). The improvement efforts involve procuring higher UV-damage-threshold beam-transport optics, obtaining better near-field beam profiles, and developing simulation tools to provide rapid prediction of laser-system performance during shot operations. Near-field beam-profile improvements include new apodizer designs in two laser stages, angular detuning of the frequency-conversion crystal to reduce $3\omega$ beam-intensity modulations, and installing a programmable spatial light modulator in the laser front end to provide closed-loop correction of the near-field beam amplitude. These enhancements have resulted in better beam quality, greater reliability, and improved efficiency during shot operations.

Amy L. Rigatti
*Editor*

# The Velocity and Timing of Multiple Spherically Converging Shock Waves in Liquid Deuterium

Inertial confinement fusion (ICF) target designs use a sequence of shocks to compress the shell and fuel assembly before they implode.[1] The fuel entropy can be controlled by optimizing the strength and timing of these shocks, thereby minimizing the required driver energy. The goal is to maintain the internal pressure of the fuel to ~1 to 2 times its Fermi-degenerate pressure. To achieve these optimal conditions, the four shocks must merge in a precise sequence at the inner surface of the fuel layer.[2,3] The National Ignition Campaign[4] for ICF ignition at the National Ignition Facility (NIF)[5] includes tuning experiments to verify shock timing as a method to set the laser to optimal drive conditions for hohlraum-driven ignition targets.[3] Similarly, the fusion program at LLE requires validation of the hydrodynamic codes used in direct-drive ICF implosions. In this article, we report on results of direct-drive experiments that mimic and exceed the conditions for the first three shocks in an ignition target. These experiments develop a shock-timing technique for ignition targets and validate simulations of direct-drive ICF targets.[6] The development was successful and this technique was applied to full-scale experiments to tune hohlraum-driven ignition targets on the NIF.[7] To model these experiments, the simulations incorporated a nonlocal model[6] to treat heat conduction in the coronal plasma. These simulations model shock velocity and timing quite well, providing confidence in the hydrodynamic codes used to design direct-drive ICF targets for OMEGA and the NIF.

In direct-drive ICF, the initial shocks are produced by short (~100-ps) laser pulses preceding the main pulse that drives the implosion.[8] Short individual pulses are desirable for direct-drive ICF because they are impulsive on hydrodynamic time scales. As a result, only the energy contained in the pulse matters, not the temporal shape. The simple temporal Gaussian pulses that high-power lasers readily produce are ideal for this purpose. Moreover, individual laser pulses provide discrete drive events that can be easily tuned to optimize shock-wave timing. The strength of those shocks depends on the energy in the pulses and on the details of the laser-target–coupling mechanisms. The strength (velocity) of those shocks is a very good measure of the efficiency of that coupling and, therefore, a sound metric for validating the hydrodynamic codes used to design ICF targets.

These experiments measured the velocity and timing of multiple converging shock waves *inside* spherical targets filled with liquid (cryogenic) deuterium. The drive laser produced a sequence of up to four shocks, whose strength and timing were designed so that later stronger shocks overtake earlier weaker ones to produce multiply shocked deuterium. These shocks ultimately coalesce about 200 $\mu$m into the deuterium, forming a single strong shock that converges toward the center of the targets. The shock velocities and the times of these mergers are measured with high precision using time-resolved velocity interferometry[9] and streaked optical pyrometry.[10] Shock velocity and timing are measured to better than the ~1% and ±50-ps precision required for ignition targets. This technique was used on full-scale NIF experiments to tune hohlraum-driven ignition targets.

The OMEGA results are best simulated when the hydrodynamic code uses a nonlocal model[6] to transport the absorbed laser energy from the coronal plasma to the ablation surface. The simulations replicate the measured shock velocities and shock merger times with high fidelity.

These experiments are the first to time multiple, spherically converging shock waves in liquid deuterium. They produced the highest-reported shock velocities in liquid deuterium and the first observation of an increase in shock strength (velocity) caused by spherical convergence.

These experiments were performed on OMEGA—a 60-beam, 351-nm laser designed to directly drive spherical-target implosions with high-irradiation uniformity.[11] The velocity interferometery system for any reflector (VISAR)[9] detects the Doppler shift of an optical (532-nm) probe beam that reflects off the shock front. To provide diagnostic access to the shock waves, spherical targets were fitted with a diagnostic cone similar to that used in the fast-ignition concept.[12] The targets are described in Ref. 7 and are shown in Fig. 125.1.

The spherical shell and cone were filled with liquid deuterium; VISAR observed the shocks on the inside of the shell through an aperture in the end of the cone.

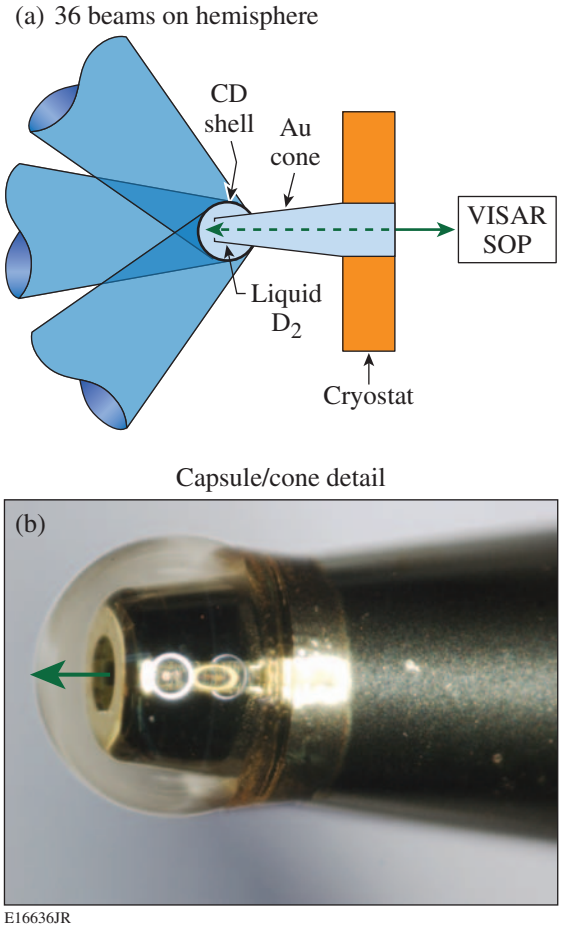


Figure 125.1
(a) Schematic of target and beam irradiation showing the 900-$\mu$m-diam CD sphere with a re-entrant cone [Fig. 125.1(b)], which is irradiated with 36 OMEGA beams. The target and cone are filled with cryogenic liquid deuterium.

The sphere was irradiated by 36 OMEGA beams on its hemisphere opposite the line of sight of VISAR. The beams were fitted with the same SG4-distributed phase plates[13] used for the 60-beam ICF implosion experiments. Two-dimensional simulations of the irradiation uniformity indicate that this configuration produces a uniform intensity distribution pattern that replicates the 60-beam irradiation uniformity in a region of ~±20° about the VISAR axis. (VISAR has an *f*/3 collection lens.) These experiments, therefore, produce an accurate surrogate for the shock-transit portion of a spherically symmetric ICF implosion. The liquid deuterium is surrogate for the deuterium–tritium ice layer in an ICF target; it provides an extended, uniform medium for the shocks to propagate. In addition to VISAR, a streaked optical pyrometer (SOP)[10] was used to observe the optical self-emission from the shocks in the deuterium.

Figure 125.2(a) shows VISAR data for a three-shock experiment (shot 59533) driven by three 100-ps laser pulses (at 0, 1, and 2 ns), which are depicted in the graph overlay in Fig. 125.2(a). The VISAR record is a 1-D image (vertical axis) of the target that is streaked in time (horizontal axis). Imposed on that image is a series of fringes whose vertical position (fringe phase) is proportional to the shock velocity. The image in Fig. 125.2(a) is a view of the shocks in the liquid deuterium

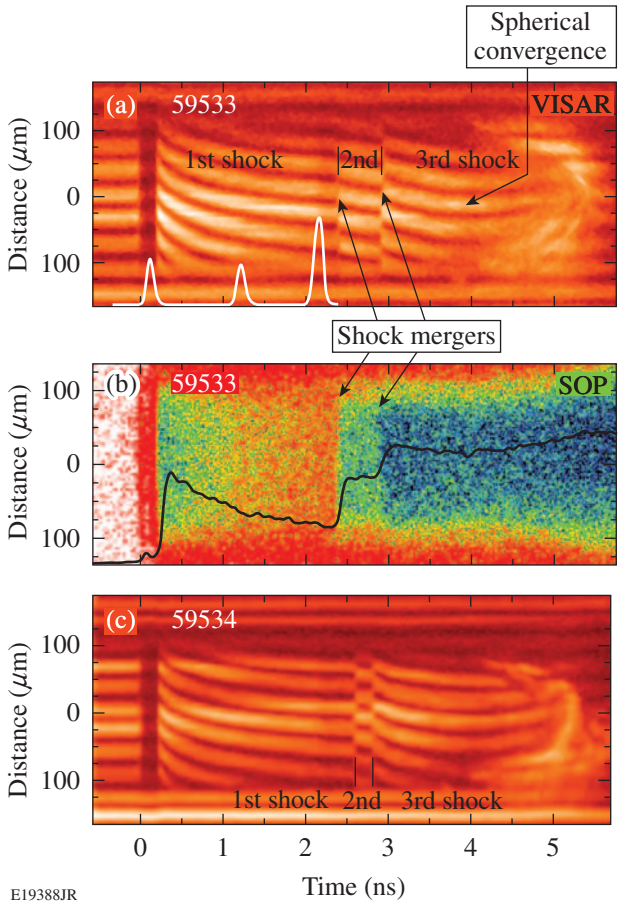


Figure 125.2
(a) VISAR data record (space versus time) with fringes that represent the velocity of the shocks produced by the laser pulse shown in the figure. The three shocks are observed as well as the jump in fringe position that occurs when the second and third shocks merge at 2.4 and 2.9 ns, respectively. (b) Streaked optical pyrometer (SOP) data showing the self-emission intensity (lineout in figure) follows the shock velocity and shock mergers, providing corroboration of shock timing. (c) VISAR data for shot with lower second pulse and higher third pulse; these delay the first merger and advance the second, illustrating the technique to time shock in a tight sequence.

contained in the shell as observed through the aperture in the re-entrant cone. The experiment was arranged so these shock waves spherically converged along the VISAR axis. VISAR was able to track this convergence until the shock impacted the front of the cone, which was 200 $\mu$m from the inside of the sphere.

Before $T = 0$, the fringes in Fig. 125.2(a) are horizontal because there was no shock or movement in the target. At $T = 0$ the signal disappears because the VISAR probe was absorbed by the 10-$\mu$m CD shell, which was photoionized by x rays from the laser-produced plasma. After the shock transited the CD and reached the deuterium (which remains transparent), the VISAR signal returns and the fringes abruptly shift in response to the shock velocity in the deuterium. At that time, the shock produced by the short pulse is unsupported and decelerating; the resulting VISAR fringes, therefore, exhibit curvature in time.

At 2.4 ns, the shock produced by the second laser pulse (at ~1 ns) overtakes the first shock. [VISAR did not detect the second shock until it overtook the first because the first shock was reflective (and opaque).] At that point, the coalesced shock (first and second shocks) was stronger and had a higher velocity; VISAR detected this sudden increase in velocity as a jump in fringe position. This is a shock-timing measurement. Since this shock was also unsupported, it decelerated as it traveled through the deuterium and the fringes are seen to slope downward. (The decay rate of this second shock is different than that of the first because the rarefaction wave that produces it now encounters double-shocked deuterium.) At 2.9 ns, the shock from the third pulse (at 2 ns) overtakes that coalesced shock and another jump in velocity occurs. This final shock is also unsupported and begins to decay, producing a downward motion of the fringes in time. At about 4 ns, the fringes curve upward, indicating acceleration. This increase in velocity is a result of spherical convergence. As this final shock (three coalesced shocks) spherically converges, its specific volume decreases and the shock strength increases, producing higher velocities. Lastly, at ~5 ns, the shock impinges on the face of the cone, producing a disturbance that propagates into the cone aperture and the VISAR line of sight. This produced the brighter signal at 5 ns that moves toward the center of the image as it fills the aperture at ~5.5 ns.

Figure 125.2(b) shows the SOP data acquired simultaneously with the VISAR data in Fig. 125.2(a). This is a color-scaled image (vertical axis) of the self-emission intensity streaked in time (horizontal axis). The solid black line through the image is a plot of the intensity (horizontal lineout) that represents the temporal profile of shock brightness (temperature), which is proportional to velocity. Note that in response to the various shocks, the SOP intensity decays and jumps in a fashion similar to the VISAR data. SOP provides an independent measure of shock strength and timing.

Figure 125.2(c) shows a VISAR image of a similar experiment (shot 59534) with a slightly modified drive pulse. The second shock was a bit weaker and the third stronger. Compared to Fig. 125.2(a), the first merger in these data occurs later (at 2.6 ns) and the second earlier (at 2.8 ns); this demonstrates a technique to produce a tight sequence of shock arrivals for an ICF target design.

On the NIF, shocks must merge in a tight sequence with a precision of ±50 ps. In the VISAR data, the shock mergers cause a fringe jump that occurs over, at most, two of the 10.6-ps pixels (i.e., ~22 ps). Calibration techniques and the temporal optical fiducials on these data allow one to calibrate the streak cameras to better than 1% precision. Together, they provide the necessary precision to time shock waves on OMEGA and the NIF to the ±50 ps required for ignition targets.

For direct-drive ICF target designs, radiation–hydrodynamic codes have long used a heuristic *flux-limiter* model to simulate the reduced flux of energy from the corona, where laser energy is deposited, to the ablation surface where pressure is applied to the target. To simulate many experimental results, the heat flux in some regions had to be limited to ~6% of that predicted by the Spitzer–Härm free-streaming limit. Recent direct-drive experiments with laser intensities $\geq 3 \times 10^{14}$ W/cm$^2$ were not well modeled using that flux limiter.[14,15] We find this is also true for the shock-velocity measurements.

Figure 125.3 shows the velocity profiles measured by VISAR (solid) recorded from a two-shock experiment where the two drive pulses had irradiation intensities of $3 \times 10^{14}$ W/cm$^2$ on a CD sphere filled with deuterium. The dotted curve in Fig. 125.3 shows the shock-velocity profile predicted by *LILAC*[16] using the flux-limiter model with $f = 0.06$. This flux-limiter value was previously constrained by simulations of various experimental observables. Note in Fig. 125.3 that it underestimates the strength of the first shock. This type of disagreement was also true for recent absorption, acceleration, and scattered-light measurements on OMEGA.[17] The dashed curve in Fig. 125.3 shows the velocities predicted when a nonlocal transport model is used.[6] This model better simulates the shock velocity produced by the first pulse and the merger time of the two shocks. Early in time, when the first pulse interacts with the solid target,

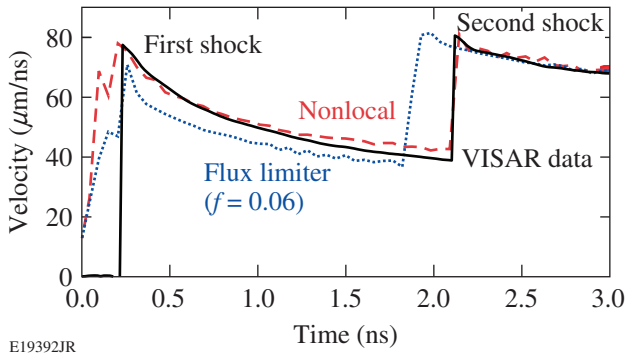


Figure 125.3
The shock-velocity profile (solid) for a two-shock experiment. The profile predicted by *LILAC* using the flux-limiter model with $f = 0.06$ (dotted) and using a nonlocal transport model (dashed). The latter better simulates the experiments, particularly the initial interaction with the target and the first shock.

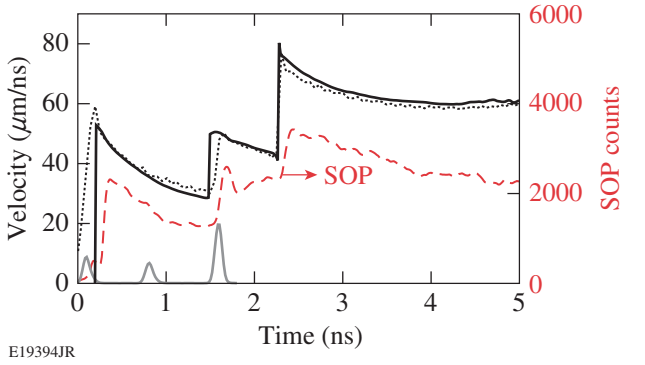


Figure 125.4
Measured-velocity profile (solid) and self-emission intensity (dashed) for a three-shock experiment. The simulated-velocity profiles (dotted) predict the velocities of each shock and their merger times with good accuracy including the effect of convergence.

the density scale is very short near the critical density, where the majority of laser light is absorbed. In the flux-limiter model, the classical Spitzer flux is replaced with 6% of the free-stream limit in a narrow region near this surface, where this limit is applied. This produces a nonphysical jump in the electron density near the critical surface, which leads to reduced absorption of laser light. The nonlocal treatment eliminates this jump, resulting in higher laser coupling and a stronger first shock, in better agreement with experimental data. Figure 125.3 shows that proper treatment of this electron transport is essential to correctly model these plasmas and predict shock timing.

Figure 125.4 shows the measured (solid)-velocity profile from an experiment (shot 59667) that used a 900-$\mu$m-diam, 5-$\mu$m-thick CH shell filled with liquid deuterium. The triple-pulse drive is shown in the figure. The dotted curve in Fig. 125.4 is the simulated velocity that matches the experiment to better than the ±50 ps required for ignition targets. Also shown is a lineout (dashed) of the SOP self-emission intensity versus time; it also provides a corroborative measure of shock velocities and shock mergers. These data also show the acceleration caused by convergence effects, as predicted by the simulations. In 5-$\mu$m–shell targets, the laser fully ablates the CH shell and begins to interact with the deuterium. The ability to model this phase is critical to the performance of direct-drive–ignition targets, which are expected to have very thin CH shells.

That the simulations accurately predict the first shock velocity indicates that the codes adequately treat the plasma-initiation problem. Similarly, the good agreement with the subsequent shock velocities indicates the expansion of the coronal plasma, and the interaction of later pulses with that preformed plasma is also well modeled. Lastly, the agreement of the predicted velocities and merger times with experiments indicates that the material properties (equations of state for CH and deuterium) used in the codes are also adequate. Obtaining good simulation of these data depended greatly on locating the target to within ~30 $\mu$m of the desired position. This ensured that the irradiation uniformity and intensity were as designed and expected.

A direct-drive ICF implosion on OMEGA has a longer (~1-ns) fourth pulse that drives the target implosion. This pulse is more intense and has significantly higher energy than the individual ~100-ps pulses preceding it. For shock-timing experiments, x rays from that drive pulse can be sufficiently intense to photoionize the quartz window at the end of the VISAR cone; this could prevent VISAR measurements. Figure 125.5 shows the VISAR signal from a four-pulse experiment where a reduction in the drive-pulse intensity made it possible to measure all four shocks using VISAR. The features of the data are similar to those in Figs. 125.2(a) and 125.2(c): the merger of the second shock with the first is evident at 1.9 ns; then at 2.4 ns the third shock merges with the first two. At 3.1 ns, the fourth shock from the main drive pulse (which started at 2 ns) overtakes the three merged shocks; soon after, the VISAR signal disappears. It is likely that, at these high pressures, the shock was sufficiently hot to photoionize the unshocked deuterium ahead of it and this material absorbed the VISAR probe beam.

In Fig. 125.6, the solid line is the velocity profile deduced from the VISAR data, showing shock velocities of 50, 56, 73, and 130 km/s for each of the four shocks. The latter velocity corresponds to a pressure of 2500 GPa in the deuterium. Ignition targets on the NIF will have the first three shock velocities in the range of 20, 40, and 70 km/s. These results

show that spherical shocks of those strengths in deuterium can readily be observed and timed using this technique. Note in Fig. 125.6 that the SOP (dashed) signal decreases (but does not disappear) at ~2.4 ns. This could be the result of initial blanking of the quartz window; the main pulse reaches its peak at this time. SOP detects light in the 590- to 850-nm range; photons in this range are better absorbed than those of the VISAR probe.

The velocity and timing of multiple, spherically converging shock waves have been measured in cryogenic-deuterium targets directly irradiated with laser pulses. A shock velocity of 135-km/s was observed in cryogenic deuterium. This is the highest shock velocity ever reported in deuterium and corresponds to a pressure of ~2500 GPa (25 Mb). This is also the first measurement of shock velocities that exhibited the effects of spherical convergence, i.e., the increase in shock strength produced by that convergence.

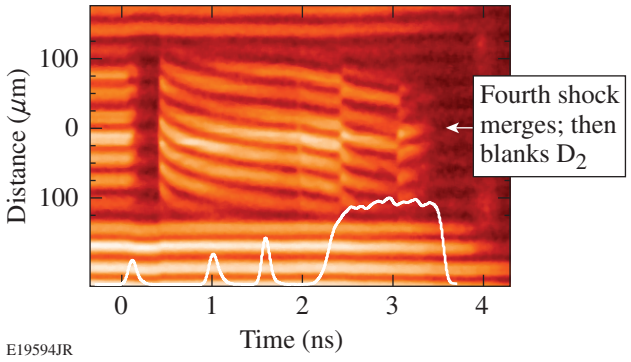


Figure 125.5
VISAR image for a four-shock experiment using an ICF drive pulse shown in the figure. Three shocks are visible as in Fig. 125.2(a) with mergers at 1.6 and 2.3 ns. At 3.1 ns, the fourth shock (produced by the main pulse) overtakes them, and soon after the x-ray flux from that pulse blanks the VISAR window.

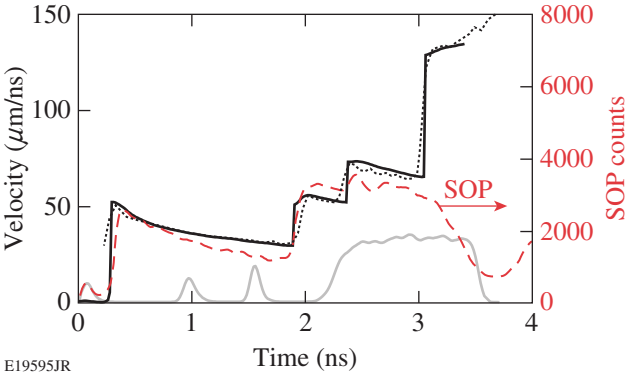


Figure 125.6
The velocity profile (solid) showing velocities of 42, 64, 83, and 135 km/s for each of the four shocks and the simulation (dotted). The latter velocity corresponds to a pressure of 2500 GPa. The SOP signal (dashed) follows VISAR during the first three shocks but then decreases at ~2.4 ns. Laser pulses are shown at the bottom of the graph.

To properly simulate these results, the hydrodynamic code used a nonlocal model to properly simulate heat transport in the coronal plasma. At high intensities, the initial plasmas produced by short (100-ps) pulses have steep density and temperature gradients, which the standard flux-limiter models do not properly treat. When a nonlocal thermal transport model is used instead, the shock velocities and timing are better modeled by the simulations. The ability to simulate these experimental results provides confidence in the hydrodynamic codes used to design direct-drive ICF targets for OMEGA and the NIF.

These experiments are the first to time multiple, spherically converging shock waves in liquid deuterium. The observed deuterium shock velocities were similar to and greater than those required for the initial phase of an ignition target on the NIF. They demonstrate the ability to time and control shock waves to the precision needed for ignition experiments. This technique was applied to full-scale experiments to tune hohlraum-driven ignition targets on the NIF.

## ACKNOWLEDGMENT

This work was supported by the U.S. Department of Energy Office of Inertial Confinement Fusion under Cooperative Agreement No. DE-FC52-08NA28302, the University of Rochester, and the New York State Energy Research and Development Authority. The support of DOE does not constitute an endorsement by DOE of the views expressed in this article.

## REFERENCES

1. J. D. Lindl, *Inertial Confinement Fusion: The Quest for Ignition and Energy Gain Using Indirect Drive* (Springer-Verlag, New York, 1998), Chap. 6, pp. 61–82.
2. D. H. Munro *et al.*, Phys. Plasmas **8**, 2245 (2001).
3. D. H. Munro, H. F. Robey, B. K. Spears, and T. R. Boehly, Bull. Am. Phys. Soc. **51**, 105 (2006).
4. B. A. Hammel and the National Ignition Campaign Team, Plasma Phys. Control. Fusion **48**, B497 (2006).
5. E. I. Moses, Fusion Sci. Technol. **54**, 361 (2008).
6. V. N. Goncharov, T. C. Sangster, P. B. Radha, R. Betti, T. R. Boehly, T. J. B. Collins, R. S. Craxton, J. A. Delettrez, R. Epstein, V. Yu. Glebov, S. X. Hu, I. V. Igumenshchev, J. P. Knauer, S. J. Loucks, J. A. Marozas, F. J. Marshall, R. L. McCrory, P. W. McKenty, D. D. Meyerhofer, S. P. Regan, W. Seka, S. Skupsky, V. A. Smalyuk, J. M. Soures, C. Stoeckl, D. Shvarts, J. A. Frenje, R. D. Petrasso, C. K. Li, F. Séguin, W. Manheimer, and D. G. Colombant, Phys. Plasmas **15**, 056310 (2008).

7. T. R. Boehly, D. H. Munro, P. M. Celliers, R. E. Olson, D. G. Hicks, V. N. Goncharov, G. W. Collins, H. F. Robey, S. X. Hu, J. A. Marozas, T. C. Sangster, O. L. Landen, and D. D. Meyerhofer, Phys. Plasmas **16**, 056302 (2009).

8. V. N. Goncharov, in *Laser-Plasma Interactions*, edited by D. A. Jaroszynski, R. Bingham, and R. A. Cairns, Scottish Graduate Series (CRC Press, Boca Raton, FL, 2009), pp. 409–418.

9. P. M. Celliers, D. K. Bradley, G. W. Collins, D. G. Hicks, T. R. Boehly, and W. J. Armstrong, Rev. Sci. Instrum. **75**, 4916 (2004).

10. J. E. Miller, T. R. Boehly, A. Melchior, D. D. Meyerhofer, P. M. Celliers, J. H. Eggert, D. G. Hicks, C. M. Sorce, J. A. Oertel, and P. M. Emmel, Rev. Sci. Instrum. **78**, 034903 (2007).

11. T. R. Boehly, D. L. Brown, R. S. Craxton, R. L. Keck, J. P. Knauer, J. H. Kelly, T. J. Kessler, S. A. Kumpan, S. J. Loucks, S. A. Letzring, F. J. Marshall, R. L. McCrory, S. F. B. Morse, W. Seka, J. M. Soures, and C. P. Verdon, Opt. Commun. **133**, 495 (1997).

12. R. Kodama *et al.*, Nature **412**, 798 (2001).

13. Y. Lin, T. J. Kessler, and G. N. Lawrence, Opt. Lett. **20**, 764 (1995).

14. W. Seka, V. N. Goncharov, J. A. Delettrez, D. H. Edgell, I. V. Igumenshchev, R. W. Short, A. V. Maximov, J. Myatt, and R. S. Craxton, Bull. Am. Phys. Soc. **51**, 340 (2006).

15. W. Seka, D. H. Edgell, J. F. Myatt, A. V. Maximov, R. W. Short, V. N. Goncharov, and H. A. Baldis, Phys. Plasmas **16**, 052701 (2009).

16. J. Delettrez, R. Epstein, M. C. Richardson, P. A. Jaanimagi, and B. L. Henke, Phys. Rev. A **36**, 3926 (1987).

17. W. Seka, D. H. Edgell, J. P. Knauer, J. F. Myatt, A. V. Maximov, R. W. Short, T. C. Sangster, C. Stoeckl, R. E. Bahr, R. S. Craxton, J. A. Delettrez, V. N. Goncharov, I. V. Igumenshchev, and D. Shvarts, Phys. Plasmas **15**, 056312 (2008).

# Impeding Hohlraum Plasma Stagnation in Inertial Confinement Fusion

The symmetry requirements for achieving ignition are fundamental and impose strict constraints on inertial confinement fusion (ICF).[1–7] The tolerable drive asymmetry of an implosion, in a time-integrated sense, is less than 1% to 2% and depends on the ignition margin.[3,4] In the indirect-drive approach to ICF, low-mode-number implosion asymmetries are a major concern because the quasi-uniform hohlraum radiation field provides drive with minimal high-mode-number nonuniformities.[3–8] An example of such an asymmetry would be a time-integrated P2 (second-order Legendre polynomial) nonuniformity that could lead to different radial velocities and densities at pole and equator, converting less kinetic energy into internal energy and resulting in a higher drive energy required for ignition.

The high-$Z$ plasma from the wall blowoff, usually gold (Au) or uranium (U), which causes motion in the laser-absorption region and alters the spatial distributions of x-ray energy sources and sinks, has been shown to cause low-mode-number implosion asymmetries.[3–8] The blowoff quickly fills the interior of an initially empty (optically thin) hohlraum, leading to early on-axis plasma stagnation.[3–8] The stagnated plasma has high pressure and can asymmetrically compress the capsule.

To achieve the required drive symmetry, the motion of the laser-deposition (x-ray emission) region must be minimized. Two proposed approaches are to overcoat a hohlraum wall surface with a low-$Z$ liner and to fill a hohlraum interior with low-$Z$ gas.[4] Neither the liner nor the fill gas stops the wall blowoff; however, they displace the low-density plasmas. In the first approach, plasma jets form because of the interaction of pairs of adjacent, expanding plumes of low-$Z$ liner blowoff.[4,9] The radially moving jets are supersonic and quickly stagnate at the hohlraum interior, resulting in asymmetries in both the drive and the capsule implosion. The ignition campaign at the National Ignition Facility (NIF) currently adopts the second approach.[3–7] Hohlraums are filled with helium-4 gas[6] at a pressure ~0.4 atm (when fully ionized, $n_e \sim 0.04\, n_{crit}$, the critical electron density for 0.35-$\mu$m laser light). The gas is contained with thin polyimide windows over the laser entrance holes (LEH's).

This article presents the first proton radiography observations of the effects of gas fill on impeding the hohlraum plasma stagnation. The experiments, illustrated schematically in Fig. 125.7(a), were performed at the Omega Laser Facility.[10] Radiographic images were made with 15-MeV protons at various implosion times through the LEH.[9,11] Figure 125.7 shows two different types of images: proton fluence versus position [Fig. 125.7(b)] and proton mean energy versus position [Fig. 125.7(c)]. The proton fluence piles up in the gaps between the two expanding plasma plumes and in the region between the imploding capsule and the expanding plasmas, forming a five-prong, asterisk-like pattern—a consequence of OMEGA's laser-beam distribution.[9,11] Contrary to earlier experiments that showed a deficit in proton fluence in these regions for vacuum hohlraums,[9,11] this fluence surplus suggests that no high-density plasma jets were formed. The fill gas along the laser beam's path is fully ionized. The interfaces between the gas plasma and the Au wall blowoff are constrained near the wall's surface [Fig. 125.7(b), indicated by the open arrows]. Figure 125.8 shows the measured Au-wall plasma-fill gas interface radius as a function of time compared with the sound speed $\left[C_s \propto \left(ZT_e m_i^{-1}\right)^{1/2}\right]$ that sets the scale for hydrodynamic rarefaction expansion in vacuum.[11,12] The expansion speed of the Au blowoff is estimated to be $\sim(2.1\pm0.3) \times 10^7$ cm s$^{-1}$, which is slower than $C_s \sim 2.5 \times 10^7$ cm s$^{-1}$, indicating that the wall blowoff's expansion has been compressed by the fill gas.[13] These measurements show that the fill gas impedes the wall plasma expansion.

An additional interface appears in the region around the imploding capsule [1.65 ns, Fig. 125.7(b)]. It is identified as the interface between the capsule's CH ablation and the fill-gas plasma. Because the implosion is nearing the deceleration phase, with the typical implosion velocity, $v_{imp}\left[\propto I_{15}^{1/8} \ln\left(m_0/m\right)\right] \sim 2$ to $3 \times 10^7$ cm s$^{-1}$ and velocity of outward-moving ablated cap-

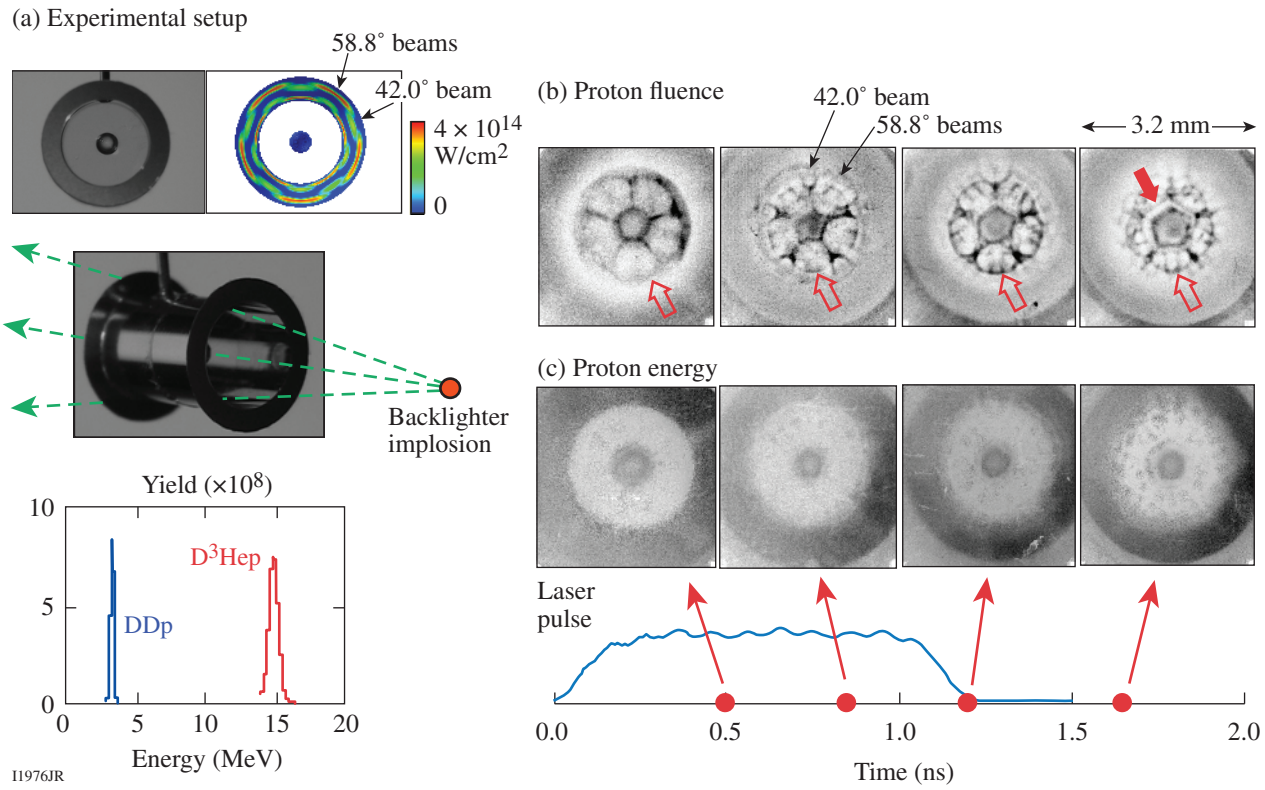


Figure 125.7

(a) Experimental setup. The two photos show an Au hohlraum filled with ~0.4 atm of neopentane gas ($C_5H_{12}$) and containing a CH capsule (30-$\mu$m-thick, 550-$\mu$m-diam plastic shell either empty or filled with 50 atm of $H_2$ gas). A proton backlighter (imploded, $D^3He$-filled, thin-glass-shell capsule driven by 30 OMEGA laser beams[15]) is typically 1 cm from the hohlraum center and has the illustrated monoenergetic spectra from the reactions $D+{}^3He \longrightarrow \alpha + p$ (14.7 MeV) and $D + D \longrightarrow T + p$ (3.0 MeV), recorded with a CR39 detector. The hohlraums had 30-$\mu$m-thick gold walls, 100% laser entrance hole (LEH), 2.4-mm diameter, and 3.8-mm length. The hohlraum was driven by 30 laser beams with a wavelength of 0.351 $\mu$m and total laser energy ~11 kJ in a 1-ns square pulse. The laser beams had full spatial and temporal smoothing.[16] Radiographic images of (b) proton fluence and (c) proton energy taken with 15-MeV $D^3He$ protons (the particle energy was slightly upshifted from its birth energy because of the capsule's positive charging) at various implosion times. Within each image, darker means (b) higher proton fluence or (c) lower proton energy. The open arrows in (b) point to the interfaces between the Au wall blowoff and gas plasmas. For the image at 1.65 ns, the solid arrow points to the interface between the capsule ablator and gas plasma.

sule material $v_{abl}\left[\propto I_{15}^{9/40}\right] \sim C_s$, the capsule is expected to be essentially unaffected by the pressure generated in this region.[4]

While the proton fluence shows large variations [Fig. 125.7(b)], the proton energy shows less variation [Fig. 125.7(c)] until later times (1.65 ns). This suggests that the trajectories of these backlighting protons have been largely affected by fields around the capsule and not by proton scattering in the plasma because Coulomb interactions are always accompanied by energy loss.[9,14]

To explore the mechanism for forming such a unique spatial (fluence) structure and its effects on impeding the hohlraum wall's plasma expansion and drive dynamics, experiments were performed with solid, spherical CH targets driven in both gas-filled Au hohlraums and CH-lined vacuum Au hohlraums (Fig. 125.9). The two images show related asterisk-like structures (with spokes in the gaps between pairs of expanding plasma plumes) but with opposite proton fluence distributions: protons were focused into the gaps (high-fluence spokes) for the gas-filled hohlraum [Figs. 125.9(a) and 125.9(c)] but were deflected away from the spokes in the CH-lined vacuum hohlraum [Figs. 125.9(b) and 125.9(d)]. The role of a spontaneously generated magnetic (B) field in these interactions can be excluded by symmetry since the toroidal B-field topology around the laser spots[15,17] cannot result in such azimuthal proton deflections.[9] Lateral electric (E) fields[18,19] associated with azimuthally oriented electron pressure gradients ($\nabla P_e$) in the plasma plumes and in the radial plasma jets, $\boldsymbol{E} = -\nabla P_e / en_e$, may be the source of these deflections. Another physical mechanism that could explain the deflection near the capsule before 0.5 ns is the E field associated with a supersonic heat front generated by the laser-heated gas channels that are in close

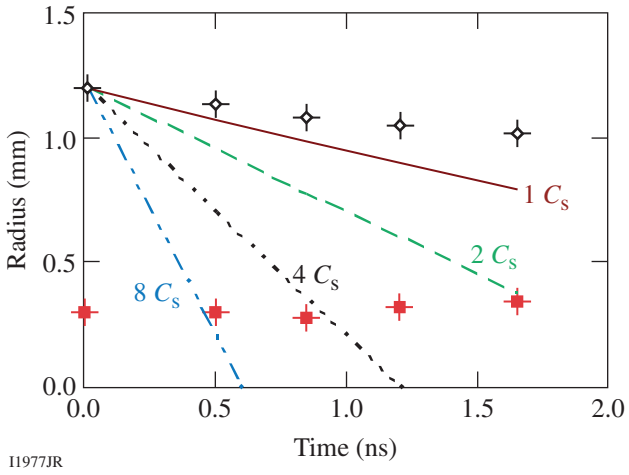


Figure 125.8
Measured interfaces between the Au wall blowoff and the gas plasma (open black diamonds), and between the capsule and the gas plasma (solid red squares), are compared to motion at multiples of the sound speed. The boundary position shown at ~0.5 ns suggests that the hot regions of the gas plasma have reached the surface of an imploding capsule at a fast speed (~8 $C_s$). The uncertainties for sampling times were ~90 ps (the backlighter burn duration), while for the radius they were ~10% (the variation in image circularity). The linear fit yields the expansion speed $v \approx (2.1\pm0.3) \times 10^7$ cm s$^{-1}$ (reduced $\chi^2 = 0.662$).

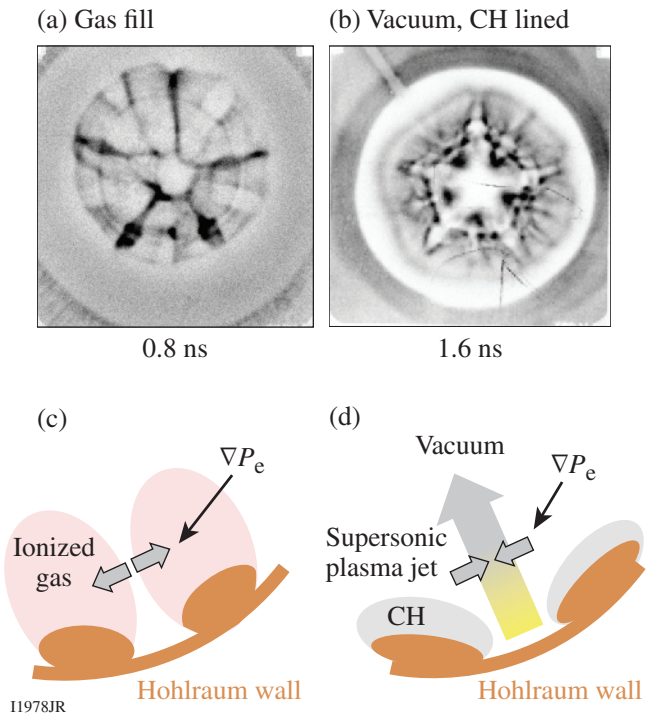


Figure 125.9
The proton fluence distributions show a surplus in the regions between the pairs of expanding plasma plumes in a gas-filled Au hohlraum (a) but show a deficit in a CH-lined, vacuum Au hohlraum (b), indicating opposing directions of the self-generated electric fields as illustrated schematically by the corresponding cartoons, in (c) and (d), respectively.

proximity to the capsule. Work is in progress to quantitatively assess the relative importance of this mechanism in the generation of such a field. Since Figs. 125.9(a) and 125.9(b) show opposite deflections, E must have pointed in opposite directions.

As illustrated in the cartoon in Fig. 125.9(c) for the gas-filled hohlraum, the high plasma pressure should have resulted from an increase of temperature inside the plasma plume and ionized gas.[20] The steep $\nabla P_e$ results in strong E fields that point laterally away from the plumes, deflecting the backlighting protons into the gaps between pairs of approaching plasma plumes. For these underdense gas plasmas (~0.04 $n_{crit}$), the rapidly rising plasma temperature in the region through which the laser passes does not result from continuous laser heating but is a consequence of the inhibition of heat flow caused by the self-generated megaGauss B field[8,9,11] because the electron thermal transport is reduced by a factor of $\left(1+\omega_{ce}^2\tau^2\right)^{-1}$, where $\omega_{ce}$ is the electron gyro frequency and $\tau$ is the collision time.[18] Including the contribution from magnetized window plasma, the Hall parameter $\omega_{ce}\tau$ is ~10 (Ref. 8). Eventually, the combination of inverse bremsstrahlung absorption in the Au wall and electron conduction establishes a near-equilibrium plasma conditions in the laser propagation channel, and the quasi pressure balance leads to continuous plasma heating and temperature increase.[4]

The spontaneous B field is generated initially at the hohlraum wall because of nonparallel density and temperature gradients $\left(\nabla n_e \times \nabla T_e\right)$. Based on the proton deflection feature, the data [Fig. 125.7(b)] show that the plasma temperatures were high[20] even at the earlier time (~0.5 ns) for the fully ionized, low-$Z$ gas plasma whose front boundary had already reached the surface of the imploding capsule within the region of the laser beam's propagation channel, indicating that inhibition of heat flow by fields must have taken place at an earlier time. This suggests that the transport of the field was much faster than the plasma's expansion speed that carried the "frozen in" field with $\left[\nabla \times (\boldsymbol{v} \times \boldsymbol{B})\right]$. The fluid velocity $v$ ($<C_s$) is too slow to explain the rapid increase in gas plasma temperature at the earlier times (Figs. 125.7–125.9). Such a nonlocal field transport must have resulted from the convection of the B field with the heat flux associated with "faster" electrons because of the Nernst effect ($\propto \beta_\wedge \boldsymbol{b} \times \nabla T_e$, i.e., the current flow is driven perpendicular to a B field and $\nabla T_e$, where $\boldsymbol{b} \equiv \boldsymbol{B}B^{-1}$ and $\beta_\wedge$ is the thermoelectric coefficient perpendicular to the B field and temperature gradient).[19,21] The velocity of convection of the B field in this

transport mechanism is approximately $v_N \approx 2q_e(5n_eT_e)^{-1}$, where $q_e = \kappa_\perp \nabla T_e$ is the electron heat flux and $\kappa_\perp$ is the thermal conductivity. Using the data from Figs. 125.7(b) and 125.8 (the position of the boundary of the gas plasma that reached the surface of an imploding capsule), a rough estimate indicates that the lower limit for the B-field convection speed is $v_N \sim 8C_s$, suggesting that the field transport (convection) by heat flux is about one order of magnitude faster than the plasma expansion ($v_N \sim 10v$). The physical process of the B-field generation, evolution, and dissipation $\left[\nabla \times \left(D_m \nabla \times \boldsymbol{B}\right)\right]$ is described by Faraday's law in a plasma as[18,19]

$$\frac{\partial \boldsymbol{B}}{\partial t} \approx -\frac{\nabla n_e \times \nabla T_e}{e n_e} + \nabla \times (\boldsymbol{v} \times \boldsymbol{B}) - \nabla \times \left(D_m \nabla \times \boldsymbol{B}\right) - \frac{\nabla \times \boldsymbol{R}}{e n_e}, \quad (1)$$

where $D_m$ is the magnetic diffusion coefficient and

$$R = \frac{\left(\alpha_\perp \boldsymbol{J}_\perp + \alpha_\wedge \boldsymbol{J} \times \boldsymbol{b}\right)}{e n_e} + \beta_\perp \nabla_\perp T_e - \beta_\wedge \boldsymbol{b} \times \nabla T_e \quad (2)$$

is the contribution of electron thermal and friction forces.[18,19,21] The data suggest that the Nernst effect is responsible for the rapid B-field transport, which is shown to play an important role in observed rapid increase in the gas plasma temperature.

The behavior and dynamics are different in the laser-irradiated, CH-lined, Au vacuum hohlraum [Fig. 125.9(b)]. Although the ablated CH wall helps to compress the Au blowoff, radially moving CH plasma jets are generated with the Au blowoff trailing.[9] This process is initiated by the CH liner ablating from the wall, which subsequently expands with the continual arrival of wall blowoff into the region between the two adjacent expanding plumes. These plasmas collide with one another, leading to the formation of the dense plasma spokes that are redirected radially and move toward the hohlraum interior. The steep $\nabla P_e$ around the jets results in radial E fields that deflect the imaging protons away from the jets and lead to the asterisk-like spoke structure in the fluence images [Fig. 125.9(d)]. The inward jets travel with supersonic speed (~4 $C_s$) generating an early-time stagnation pressure that affects capsule implosion symmetry and dynamics,[9] a phenomenon also observed in the pure vacuum Au hohlraum-driven experiments.[11]

The widths of the spokes in the images can be used with the imaging geometry to estimate the field $\int \boldsymbol{E} \times d\boldsymbol{\ell} \sim 3 \times 10^5$ V (where $d\boldsymbol{\ell}$ is the differential path length along the proton trajectory through the field area).[9] A scale length of ~0.1 cm (~laser spot width) for the field in a jet spoke implies $E \sim 3 \times 10^6$ V cm$^{-1}$.

To further study the dynamics of the interface and its effect on impeding the plasma stagnation, capsule implosions were performed with a denser hohlraum gas fill (~1 atm, $C_5H_{12}$) at two sampling times (Fig. 125.10). A relatively smooth interface appears between the expanding wall blowoff and the ionized fill gas at 0.8 ns, while chaotic spatial structure and interface interpenetration are evident at 1.6 ns. This interpenetration is caused by hydrodynamic instabilities. The surface perturbations that are seeded at the plume front can be amplified by the classical Rayleigh–Taylor (RT) instability occurring at the interface of the lighter, decelerating ionized gas plasma and the heavier, expanding Au blowoff.[4] This instability has a growth rate[4] $\gamma_{RT} \approx \left(2\pi A_t a k\right)^{1/2}$, where $a$ is the acceleration, ~$10^{16}$ cm s$^{-2}$ is estimated from Fig. 125.7(b); $k = m(2\pi r)^{-1}$ is the perturbation wave number. As an example, for a mode number $m \sim 50$ at half the hohlraum radius $r \sim 0.5 \times 0.12$ cm, $k \sim 130$ cm$^{-1}$, and $A_t = \left(\rho_2 - \rho_1\right)/\left(\rho_2 + \rho_1\right)$ is the Atwood number at the interface. For ~0.1 $n_{crit}$ the gas-fill plasma has a $\rho_1 \approx 3$ mg cm$^{-3}$ while the Au plasma has a $\rho_2 \approx 10$ mg cm$^{-3}$; therefore $A_t \approx 0.54$. A rough estimate gives $\gamma_{RT} \sim 2.7 \times 10^9$ s$^{-1}$ and a perturbation grows by a factor of ~15 in 1 ns. A similar interaction process occurred between the ablated capsule plasma and the gas plasma. The consequence is a reduced benefit of the gas fill because the enhanced interpenetration (or mixing) between the Au blowoff and the gas plasma leads to high-$Z$ material stagnating earlier in the hohlraum interior. This effect does not appear to be

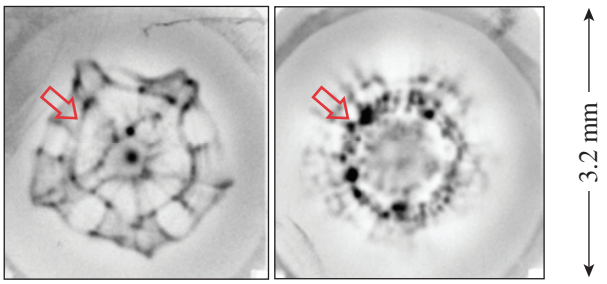


Figure 125.10
Proton fluence images of capsule implosions driven by gas-filled hohlraums. The open arrows point to interfaces between the Au wall blowoff and gas plasma. A relatively smooth interface appears between the expanding wall blowoff and the ionized fill gas at time 0.8 ns, while chaotic spatial structure and interface interpenetration are evident at time 1.6 ns. The fluence surplus inside the imploding capsule (0.8 ns) resulted from self-generated radial E fields.[22,23]

severe because it happens during the coasting phase when the capsule implosion moves at a speed $v_{imp}$ that is comparable to, or even faster than, the outward ablation speed ($\sim C_s$). At this time, the high-$Z$ blowoff should be sonically decoupled from the imploding capsule.

To explore the role that CH windows play in impeding the plasma stagnation, we performed capsule implosions driven by vacuum hohlraums with a CH window on both LEH's. This is an important issue because when laser beams pass through the LEH's, the CH windows are immediately evaporated, ionized, and magnetized. The high-pressure, low-$Z$ window plasma will rapidly flow into the hohlraum interior, filling it and altering the wall blowoff dynamics and impeding the plasma stagnation, like the gas fill does. The spontaneous B fields will convect with the flowing window plasma and inhibit electron thermal conduction, further increasing the plasma temperature[18,19,21] and impeding the motion of the wall blowoff. Figure 125.11 shows radiographic images taken while the drive laser was on. Because of the inflow of CH window plasma, no plasma jets formed and the wall blowoff was contained radially. More protons deflected in the radial direction than in the lateral directions of the radial expanding plume. This is because $|\boldsymbol{L}_T| > |\boldsymbol{L}_n|$, where $\boldsymbol{L}_T = T_e(\nabla T_e)^{-1}$ and $\boldsymbol{L}_n = n_e(\nabla n_e)^{-1}$ are the temperature and density scale lengths, respectively, and $\boldsymbol{E} \approx |\boldsymbol{E}_r + \boldsymbol{E}_\theta| \propto n_e^{-1}\nabla P_e \sim T_e|\boldsymbol{L}_n^{-1} + \boldsymbol{L}_T^{-1}|$, leading to $|\boldsymbol{E}_r| > |\boldsymbol{E}_\theta|$.

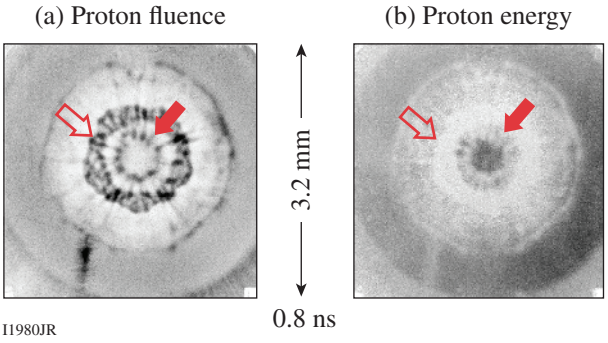


Figure 125.11
Images of (a) proton fluence and (b) proton energy from a solid CH sphere driven by a vacuum Au hohlraum with polyimide windows. The open (solid) arrows point to the interfaces between the Au wall blowoff and gas plasma (between the capsule ablation and gas plasma).

In summary, we have performed the first time-gated proton radiography of the spatial structure and temporal evolution of how the fill gas compresses the wall blowoff, inhibits plasma jet formation, and impedes plasma stagnation in the hohlraum interior. We have shown that the plasma interpenetrate caused by the classical Rayleigh–Taylor instabilities occurs as the lighter, decelerating ionized fill gas pushes against the heavier, expanding gold wall blowoff. We have demonstrated the important roles of spontaneously generated E and B fields in the hohlraum dynamics and capsule implosion. The heat flux is shown to rapidly convect the B field because of the Nernst effect. This experiment provides novel physics insight into the effects of fill gas on x-ray–driven implosions and will have an important impact on the ignition experiments at the NIF.

## ACKNOWLEDGMENT

This work was supported in part by the U.S. Department of Energy and LLE National Laser User's Facility (DE-FG52-07NA28059 and DE-FG03-03SF22691), LLNL (B543881 and LDRD-08-ER-062), LLE (414090-G), FSC (412761-G), and General Atomics (DE-AC52- 06NA 27279). A. B. Zylstra is supported by the Stewardship Science Graduate Fellowship (DE-FC52-08NA28752).

## REFERENCES

1. J. Nuckolls *et al.*, Nature **239**, 139 (1972).
2. R. L. McCrory, J. M. Soures, C. P. Verdon, F. J. Marshall, S. A. Letzring, S. Skupsky, T. J. Kessler, R. L. Kremens, J. P. Knauer, H. Kim, J. Delettrez, R. L. Keck, and D. K. Bradley, Nature **335**, 225 (1988).
3. S. W. Haan *et al.*, Phys. Plasmas **2**, 2480 (1995).
4. J. D. Lindl, *Inertial Confinement Fusion: The Quest for Ignition and Energy Gain Using Indirect Drive* (Springer-Verlag, New York, 1998).
5. S. Atzeni and J. Meyer-ter-Vehn, *The Physics of Inertial Fusion: Beam Plasma Interaction, Hydrodynamics, Hot Dense Matter*, International Series of Monographs on Physics (Clarendon Press, Oxford, 2004).
6. S. H. Glenzer *et al.*, Science **327**, 1228 (2010).
7. O. L. Landen, T. R. Boehly, D. K. Bradley, D. G. Braun, D. A. Callahan, P. M. Celliers, G. W. Collins, E. L. Dewald, L. Divol, S. H. Glenzer, A. Hamza, D. G. Hicks, N. Hoffman, N. Izumi, O. S. Jones, R. K. Kirkwood, G. A. Kyrala, P. Michel, J. Milovich, D. H. Munro, A. Nikroo, R. E. Olson, H. F. Robey, B. K. Spears, C. A. Thomas, S. V. Weber, D. C. Wilson, M. M. Marinak, L. J. Suter, B. A. Hammel, D. D. Meyerhofer, J. Atherton, J. Edwards, S. W. Haan, J. D. Lindl, B. J. MacGowan, and E. I. Moses, Phys. Plasmas **17**, 056301 (2010).
8. S. H. Glenzer *et al.*, Phys. Plasmas **6**, 2117 (1999).
9. C. K. Li, F. H. Séguin, J. A. Frenje, M. Rosenberg, R. D. Petrasso, P. A. Amendt, J. A. Koch, O. L. Landen, H. S. Park, H. F. Robey, R. P. J. Town, A. Casner, F. Philippe, R. Betti, J. P. Knauer, D. D. Meyerhofer, C. A. Back, J. D. Kilkenny, and A. Nikroo, Science **327**, 1231 (2010).
10. J. M. Soures, R. L. McCrory, C. P. Verdon, A. Babushkin, R. E. Bahr, T. R. Boehly, R. Boni, D. K. Bradley, D. L. Brown, R. S. Craxton, J. A. Delettrez, W. R. Donaldson, R. Epstein, P. A. Jaanimagi, S. D. Jacobs, K. Kearney, R. L. Keck, J. H. Kelly, T. J. Kessler, R. L. Kremens, J. P. Knauer, S. A. Kumpan, S. A. Letzring, D. J. Lonobile, S. J. Loucks,

L. D. Lund, F. J. Marshall, P. W. McKenty, D. D. Meyerhofer, S. F. B. Morse, A. Okishev, S. Papernov, G. Pien, W. Seka, R. Short, M. J. Shoup III, M. Skeldon, S. Skupsky, A. W. Schmid, D. J. Smith, S. Swales, M. Wittman, and B. Yaakobi, Phys. Plasmas **3**, 2108 (1996).

11. C. K. Li, F. H. Séguin, J. A. Frenje, R. D. Petrasso, P. A. Amendt, R. P. J. Town, O. L. Landen, J. R. Rygg, R. Betti, J. P. Knauer, D. D. Meyerhofer, J. M. Soures, C. A. Back, J. D. Kilkenny, and A. Nikroo, Phys. Rev. Lett. **102**, 205001 (2009).

12. R. P. Drake, *High-Energy-Density Physics: Fundamentals, Inertial Fusion, and Experimental Astrophysics,* Shock Wave and High Pressure Phenomena (Springer, Berlin, 2006).

13. For an adiabatic rarefaction expansion of an ideal gas, the expansion speed is 3 $C_S$ in vacuum, while the hot electrons advancing ahead of the rarefaction expansion because of their high mobility may further boost the motion of leading edge CH and Au ions ablating off the hohlraum wall by an additional $C_S$ factor.[9]

14. C. K. Li and R. D. Petrasso, Phys. Rev. Lett. **70**, 3059 (1993).

15. C. K. Li, F. H. Séguin, J. A. Frenje, J. R. Rygg, R. D. Petrasso, R. P. J. Town, P. A. Amendt, S. P. Hatchett, O. L. Landen, A. J. MacKinnon, P. K. Patel, V. A. Smalyuk, T. C. Sangster, and J. P. Knauer, Phys. Rev. Lett. **97**, 135003 (2006).

16. D. D. Meyerhofer, J. A. Delettrez, R. Epstein, V. Yu. Glebov, V. N. Goncharov, R. L. Keck, R. L. McCrory, P. W. McKenty, F. J. Marshall, P. B. Radha, S. P. Regan, S. Roberts, W. Seka, S. Skupsky, V. A. Smalyuk, C. Sorce, C. Stoeckl, J. M. Soures, R. P. J. Town, B. Yaakobi, J. D. Zuegel, J. Frenje, C. K. Li, R. D. Petrasso, D. G. Hicks, F. H. Séguin, K. Fletcher, S. Padalino, C. Freeman, N. Izumi, R. Lerche, T. W. Phillips, and T. C. Sangster, Phys. Plasmas **8**, 2251 (2001).

17. R. D. Petrasso, C. K. Li, F. H. Séguin, J. R. Rygg, J. A. Frenje, R. Betti, J. P. Knauer, D. D. Meyerhofer, P. A. Amendt, D. H. Froula, O. L. Landen, P. K. Patel, J. S. Ross, and R. P. J. Town, Phys. Rev. Lett. **103**, 085001 (2009).

18. S. I. Braginskii, in *Reviews of Plasma Physics*, edited by Acad. M. A. Leontovich (Consultants Bureau, New York, 1965), Vol. 1.

19. M. G. Haines, Phys. Rev. Lett. **78**, 254 (1997).

20. Such a temperature rise has been seen with Thomson scattering in Nova experiments, where an electron temperature ~2 keV was measured on the axis of a gas-filled hohlraum at early times during a 1-ns laser pulse ($I \approx 10^{15}$ W/cm$^{-2}$), and in LASNEX simulations of the development of hot regions along the laser-pass channel.[8]

21. A. Nishiguchi *et al.*, Phys. Rev. Lett. **53**, 262 (1984).

22. C. K. Li, F. H. Séguin, J. R. Rygg, J. A. Frenje, M. Manuel, R. D. Petrasso, R. Betti, J. Delettrez, J. P. Knauer, F. Marshall, D. D. Meyerhofer, D. Shvarts, V. A. Smalyuk, C. Stoeckl, O. L. Landen, R. P. J. Town, C. A. Back, and J. D. Kilkenny, Phys. Rev. Lett. **100**, 225001 (2008).

23. P. A. Amendt *et al.*, Plasma Phys. Control. Fusion **51**, 124048 (2009).

# Initial Cone-in-Shell, Fast-Ignition Experiments on OMEGA

## Introduction

Fast ignition[1,2] is an attractive option for inertial confinement fusion because the target compression and ignition stages are separated, relaxing the requirements on the symmetry of the implosion and the compression energy. Massive fuel shells can be imploded with low velocity, providing the potential of higher gains at lower total driver energy than in conventional central hot-spot ignition schemes.[3] In fast ignition, the dense core is ignited by particles (electrons, protons, or ions) generated by a short, ultra-intense, high-energy laser pulse. Fast ignition relies on the localized deposition of the particle energy in the core. Design studies have been performed for electrons with integrated simulations coupling a hydrodynamic code with a hybrid particle-in-cell (PIC) code.[4] The simulations estimate that electron-beam energies ranging from ~40 to 100 kJ are required for ignition, assuming a Gaussian-shaped fast-electron beam with an ~30-$\mu$m spot size, a 10-ps duration, and a relativistic Maxwellian distribution with ~2-MeV mean energy. The beam is injected 125 $\mu$m from the target center into a compressed DT core with $\rho \sim$ 500-g/cm$^3$ peak density and $\rho R \sim$ 1-g/cm$^2$ areal density.[4] The ignition threshold depends on the initial beam's full-divergence angle, which was varied from 40° to 80° in the simulation. Similar ignition electron-beam energies have been obtained in other design studies.[5,6] These design studies are still lacking a detailed description of the laser–plasma interaction, which is complex and will require massive, large-scale, three-dimensional (3-D) PIC simulations.[7]

Maximizing the coupling efficiency of the short-pulse energy into core heating remains a challenge for full-scale fast ignition. The conversion efficiency of fast electrons with the appropriate energy (1 to 2 MeV) needs to be maximized, and the particles must be transported efficiently from their source location to the compressed fuel, where they must be stopped in a sufficiently small volume that matches the optimal size of the ignition spark. Self-generated resistive magnetic fields are predicted to significantly affect the transport of hot electrons.[8,9] A self-generated magnetic field may collimate the beam as a whole while it propagates into the dense core and, therefore, may increase the coupling efficiency.[10]

It is important to bring the fast-electron source as close as possible to the fuel assembly. A very promising approach is the cone-in-shell concept[11] with encouraging initial integrated experiments at the GEKKO Laser Facility, which reported significant heating by a 0.6-ps, 300-J short-pulse laser.[12] The re-entrant cone makes it possible for a high-energy petawatt laser pulse to propagate as close as possible to the dense core, avoiding the need to channel the laser beam through a large region of plasma material.

Figure 125.12 shows a schematic of the integrated cone-in-shell, fast-ignitor experiments reported here, which were conducted at the Omega Laser Facility,[13] including the short-pulse OMEGA EP laser.[14] The coupling efficiency will depend on the separation of the cone tip from the dense plasma. A shorter distance will increase the hydrodynamic forces on the cone tip, which result from a jet formed by imploded plasma impacting the cone tip and launching a shock wave through the tip. This shock wave must not break out from the inner cone surface before the short pulse is fired; otherwise, plasma will quickly fill the cone, significantly increasing the electron-propagation distance and lowering the transport efficiency.

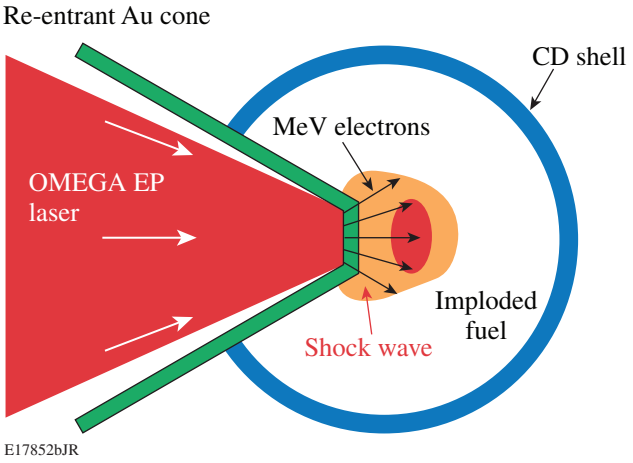


Figure 125.12
Schematic of the integrated cone-in-shell, fast-ignition experiment.

Design studies and experiments are needed to determine the optimum separation distance, tip thickness, and cone wall material. The shell mass and implosion velocity will have a significant effect on the force that the plasma jet exerts on the cone tip. It has been shown that low-velocity implosions of massive shells on a low adiabat lead to a cold and dense fuel assembly that is ideal for fast ignition.[3] The resulting dense core has a relatively low pressure and large size, reducing the hydrodynamic forces and creating a smaller distance between the tip and the dense core edge. Spherical symmetric low-adiabat implosions of cryogenic targets in direct-drive geometry have been demonstrated on OMEGA with triple-picket laser pulses, achieving a neutron-rate–averaged areal density ($\rho R$) of up to 300 mg/cm$^2$ (Ref. 15).

This article describes initial integrated fast-ignition experiments at the Omega Laser Facility, which uses low-adiabat implosions and demonstrates core heating with a 1-kJ, 10-ps, short-pulse laser. Companion experiments demonstrate that the cone tip is intact at the time when the short-pulse laser is fired into the cone. The integrated experiments produced up to ~$1.4 \times 10^7$ additional neutrons.

The following sections describe the targets and the laser setup; discuss shock-breakout measurements, the integrated fast-electron heating experiment, and the integrated simulations; and conclude with a summary.

## Targets and Laser Setup

The targets were relatively thick walled (40-$\mu$m), ~870-$\mu$m-outer-diam deuterated-plastic (CD) shells with an inserted hollow gold cone; they were fabricated and characterized by General Atomics.[16] Figure 125.13(a) is a photograph of a target mounted on a support stalk; Fig. 125.13(b) shows a target cross section with target dimensions. A shelf is machined into the gold cone to attach the shell. This serves as a reference for placing the tip precisely in the desired location, 40±10 $\mu$m away from the center of the shell along the cone axis. The shell was not filled with gas for these experiments. An x-ray radiograph of such a target can be found in Ref. 17. The cone has an inner full opening angle of 34±1°, a side-wall thickness of 10 $\mu$m, and a small circular flat tip. The cone wall is 50 $\mu$m thick outside the shell. The tip diameter was either 10 or 40 $\mu$m. The tip thickness was 5, 10, or 15 $\mu$m in the shock-breakout experiment described in **Shock-Breakout Measurements**, p. 15 and 10 or 15 $\mu$m in the integrated shots discussed in **Integrated Fast-Electron–Heating Experiments**, p. 17.

The shells were imploded on an adiabat of $\alpha_{in} \approx 1.5$ (Ref. 18), where $\alpha_{in}$ is defined as the ratio of plasma pressure in the inner portion of the shell to the Fermi pressure of a fully degenerate electron gas. Figure 125.14 shows the ~2.7-ns drive pulse, consisting of a 90-ps full-width-at-half-maximum (FWHM) Gaussian prepulse with ~6.5 TW of peak power attached to a shaped main pulse with a foot power of ~0.8 TW and a peak power of ~12 TW. The shell was imploded using 54 out of the 60 UV OMEGA beams with a total energy of ~20 kJ. The laser light was smoothed with polarization rotators and distributed phase plates.[19,20]

The fuel assembly was optimized in previous work,[18,21] with a predicted peak $\rho R$ of ~0.4 g/cm$^2$ and $\rho_{max}$ of ~150 g/cm$^3$ for an empty-shell target. Secondary proton measurements with symmetrically irradiated 40-$\mu$m spherical plastic shells filled

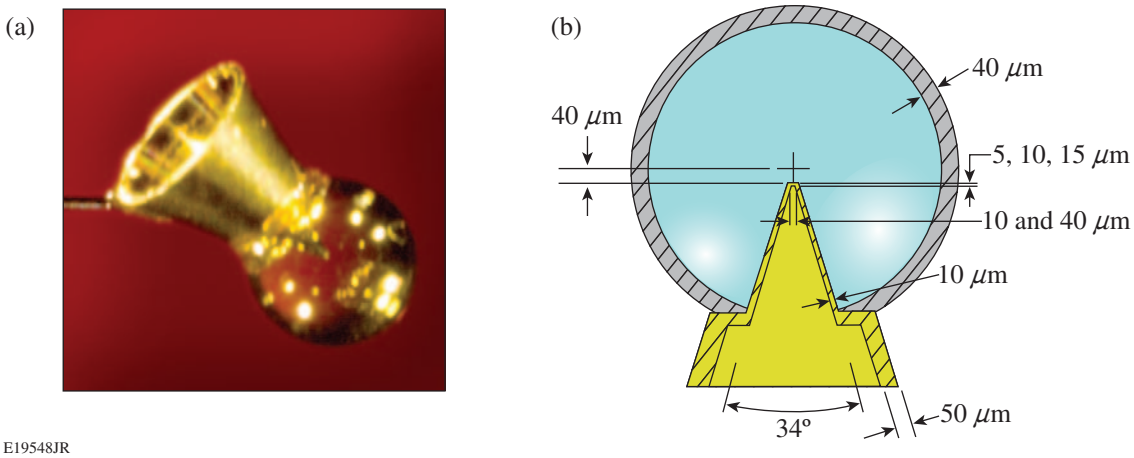


Figure 125.13
(a) Photograph of a gold re-entrant cone target; (b) cross-sectional drawing through the shell and cone tip with target dimensions.

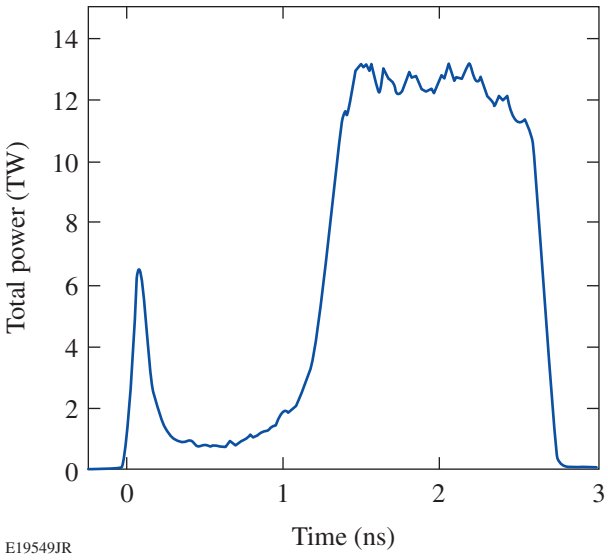


Figure 125.14
Drive-laser pulse shape (shot 55154).

with 25 atm of $D_2$ gas demonstrated a fuel assembly close to the 1-D prediction, a measured neutron-averaged $\rho R$ of 0.15 g/cm$^2$, and a peak $\rho R$ of 0.26 g/cm$^2$ (Ref. 18).

The 1053-nm–wavelength short pulse from the OMEGA EP laser had an energy of ~1 kJ and a 10-ps duration and was focused to a spot with a radius of $R_{80}$ = (26±2) $\mu$m and containing 80% of the laser energy. A high-resolution wavefront sensor measured the on-shot fluence distribution in the focal plane of the OMEGA EP pulse at full energy.[22] More than 30% of the laser energy had an intensity >1 × 10$^{19}$ W/cm$^2$, while the average intensity within $R_{80}$ was (6±2) × 10$^{18}$ W/cm$^2$. The focal pattern and $R_{80}$ varied slightly from shot to shot. A picture of the focal spot can be found in Ref. 23.

A high laser contrast, defined as the ratio of the peak power to the power of the pedestal before the main pulse, is critical for cone-in-shell fast ignition,[24] requiring careful characterization of the prepulse. A nanosecond prepulse caused by front-end parametric fluorescence preceded the OMEGA EP pulse, which was spatially and temporally resolved.[25] The on-shot temporal contrast was measured with a set of calibrated fast photodiodes. The measured power and energy contrast were (3.1±0.5) × 10$^6$ and (4.6±0.9) × 10$^4$, respectively, leading to a prepulse energy of ~22 mJ for a 1-kJ main-pulse energy. The prepulse is described by a Gaussian with FWHM of 0.9 ns and a peak 1 ns before the main pulse. [See Fig. 1(b) in Ref. 23.] The focal spot of the prepulse was measured to have a diameter of 39±3.5-$\mu$m FWHM, resulting in a prepulse intensity of (1.7±0.4) × 10$^{12}$ W/cm$^2$.

**Shock-Breakout Measurements**

The compressing shell pushes a jet of plasma material toward the cone tip,[17] heating the plasma to a temperature >1 keV and creating a shock wave through the cone wall. Shock-breakout measurements[26] were performed by imploding the shell without a short-pulse beam, using targets with a 40-$\mu$m-diam flat tip and thicknesses between 5 and 15 $\mu$m (Fig. 125.15). When the shock wave reached the inner cone surface, it generated optical emission inside the hollow cone, which was measured and temporally resolved with a streaked optical pyrometer (SOP)[27] in the wavelength range ~600 to ~750 nm and a velocity interferometer system for any reflector (VISAR)[28] at a wavelength of 532 nm. Figure 125.15(b) shows the measured SOP signal as a function of time for a 14-$\mu$m-thick tip. The optical emission suddenly rises when the shock breaks out at 3.72 ns. SOP integrates over a time period of 150 ps, determined by the slit width and the sweep speed of the streak camera. The signal is differentiated with respect to time and the first peak determines shock breakout with an accuracy of ±30 ps.[27] VISAR achieves a higher precision of ±10 ps in measuring shock breakout because of a faster streak camera.[28] Figure 125.15(c) shows the time of shock breakout as a function of tip thickness. The red circles are the VISAR and the blue squares the SOP measurements. Except for one shot at 10 $\mu$m, there is good agreement between both diagnostics within their error bars. With increasing tip thickness, the breakout is delayed. For thicknesses of 10 and 15 $\mu$m, the shock-breakout time was 3.70±0.03 ns and 3.76±0.03 ns, respectively. The red line is a weighted fit through all the data points.

The implosion of the cone-in-shell target and the shock propagation through the cone wall were simulated with the 2-D hydrodynamics code *SAGE*[29] in cylindrical geometry. Figure 125.16 shows a sequence of frames with zoomed images of the cone tip at times around peak compression. The first frame at 3.46 ns shows an intact cone tip when the shock wave just starts to enter the cone wall. At 3.50 ns the shock has propagated about halfway through the cone wall, pushing the outside cone wall back by ~5 $\mu$m, but has not broken out at the inner wall. In the simulation, the shock breaks through at 3.54 ns, ~0.2 ns before the experimentally measured breakout time of 3.76 ns. After shock breakout, the cone is predicted to very rapidly fill up with plasma below solid density but above the critical density of the short-pulse laser. A run with a 10-$\mu$m flat tip shows very similar shock behavior and a slightly earlier (40 ps) breakout time. No breakout measurements are available for the 10-$\mu$m flat tip. Using the relative timing from the simulations and the absolute timing from the measurements, the breakout time for 10-$\mu$m flat and

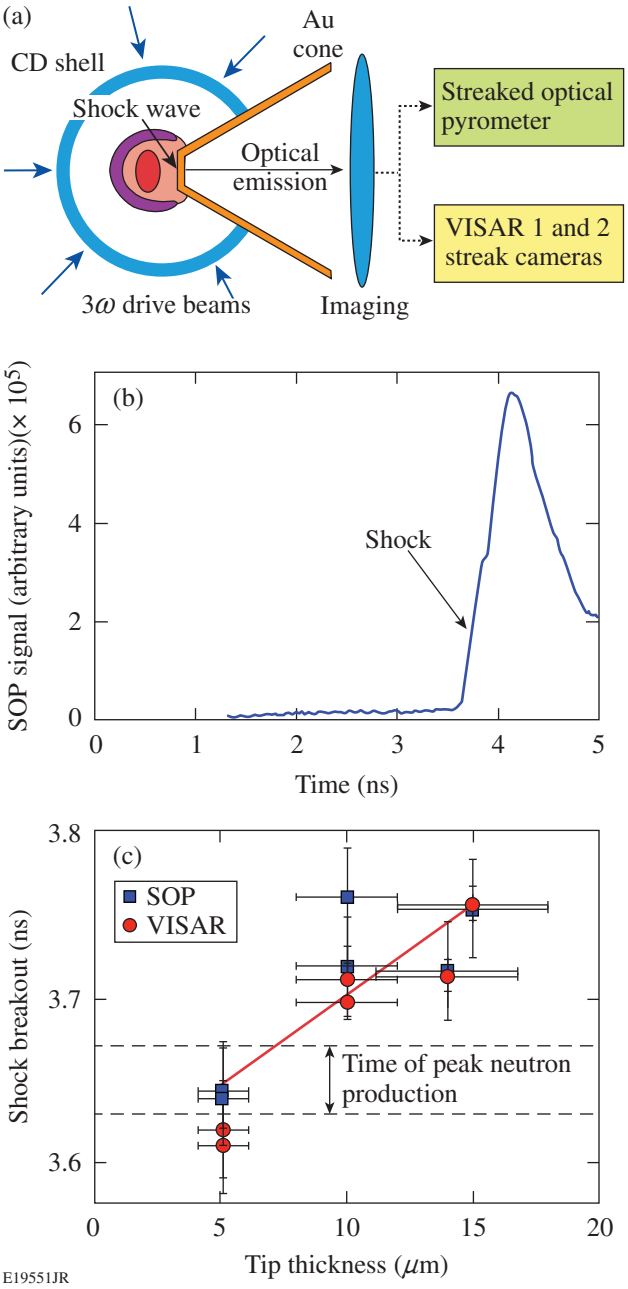


Figure 125.15
(a) Schematic of the shock-breakout experiment. The CD shell was imploded using just the long-pulse, 351-nm drive beams, resulting in shock propagation through the tip of the cone. Emergence of the shock at the inside of the tip was diagnosed using a streaked optical pyrometer (SOP) and VISAR. (b) SOP trace for a typical shot and (c) measured breakout time inside the cone for various tip thicknesses. The breakout is later for thicker cone tips.

15-$\mu$m-thick tip is extrapolated to 3.72±0.03 ns. This number is compared to the measured time of peak neutron production [see **Integrated Fast-Electron–Heating Experiments**, p. 17], which results in 3.65±0.02 ns for 10-$\mu$m flat, 15-$\mu$m-thick tips.

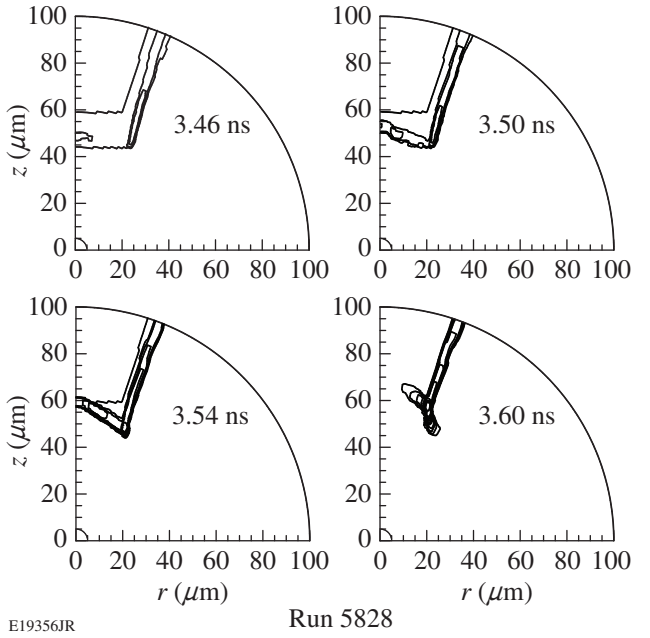


Figure 125.16
Sequence of density contours above 10 g/cm$^3$ in the tip of a Au cone from a 2-D *SAGE* simulation, showing the rapid propagation of a strong shock wave through a 15-$\mu$m cone tip. The fuel assembly from a cone-in-shell target (not shown) generates the shock. The shock propagates faster through the cone tip than through the wall.

Shock breakout appeared 70±36 ps after the peak of neutron production, confirming that the cone tip was intact at optimum OMEGA EP timing.

The VISAR measurements indicate that preheat can lead to a premature release of material inside the hollow cone if the cone wall is not thick enough. X-ray radiation in the ~5- to 10-keV photon range from the shell plasma can preheat the cone tip, as shown in Fig. 125.17(a). The temperature at the inside of the gold wall depends on the thickness of the tip. Figure 125.17(b) shows the electron temperature as a function of time for 5-$\mu$m and 15-$\mu$m thicknesses, calculated using the radiation hydrodynamic code *LILAC*.[30] *LILAC* modeled the x-ray production in the corona of the imploding shell during the drive pulse and its transport to the cone tip. At 1.5 ns, when the main-pulse intensity reaches its plateau, the temperature reaches ~0.5 eV or ~6000 K in the 5-$\mu$m case, while it is much lower for 15 $\mu$m. The temperature in the 5-$\mu$m tip is higher than the melting and boiling temperatures of gold, which are 1337 K and 3129 K (Ref. 31), respectively. Temperatures as high as ~2 eV or ~24,000 K are calculated at the end of the drive pulse are certainly sufficient to generate a gold plasma with a low degree of ionization. This effect is clearly observed in the VISAR measurement of Fig. 125.17(c).

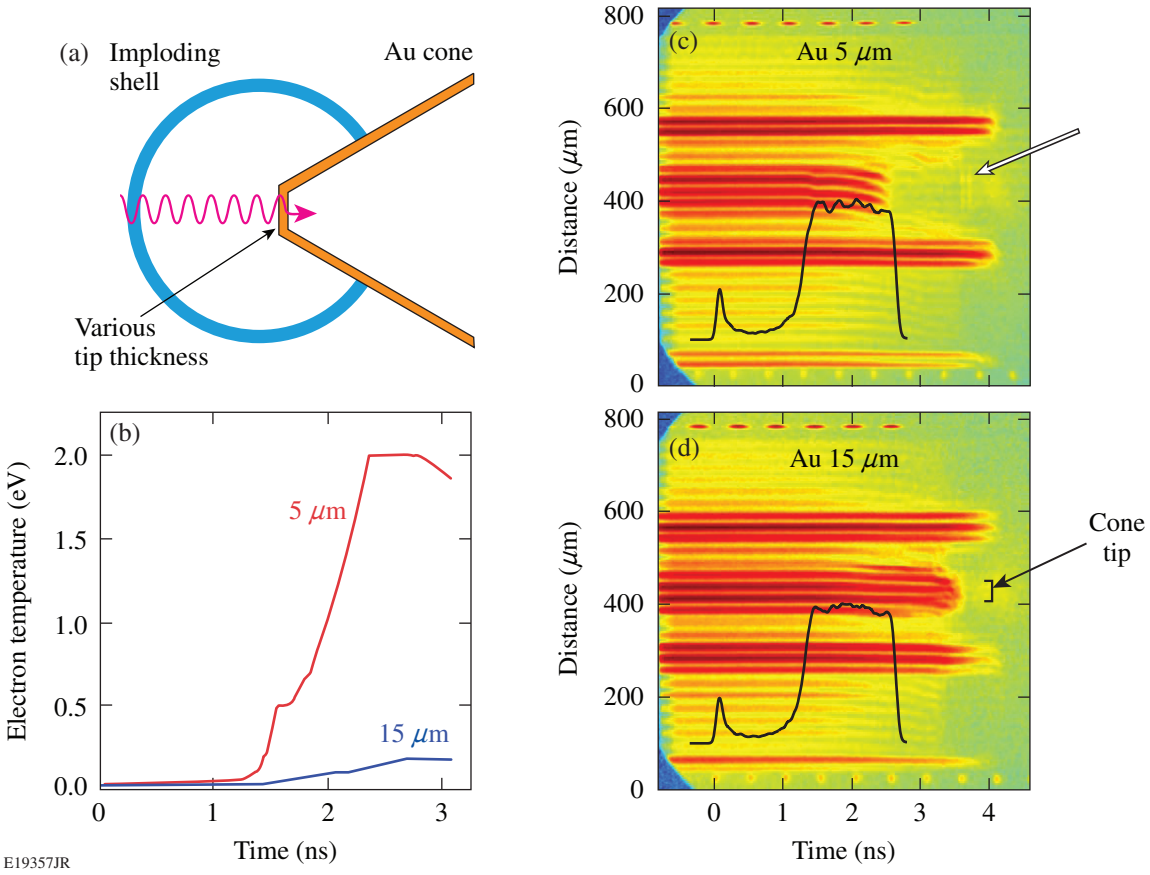


Figure 125.17
(a) Schematic for simulations of radiation preheat of the cone tip. Coronal x-ray radiation from the shell driven by the strong UV pulse can penetrate through the cone wall, preheating the gold material. (b) Calculated electron temperature at the inside of the cone tip for 5-$\mu$m and 15-$\mu$m thicknesses. (c) VISAR trace for a 5-$\mu$m thickness; the disappearance of the fringes at ~2.5 ns indicate preheat. The white arrow marks the optical emission at the shock-breakout time. (d) VISAR trace for a 15-$\mu$m thickness, showing no attenuation before shock breakout at 3.75 ns. The brace indicates the spatial range of the flat tip. In (c) and (d) the black curve indicates the laser's temporal shape.

The fringes are formed by a probe laser reflecting from the inside of the cone tip back into an interferometer. The VISAR diagnostic is a high-resolution optical imager that projects a magnified image (25.5×) of the inside of the cone onto the slits of a pair of streak camera detectors.[28] The system was aligned such that it imaged sharply the flat tip portion. The brace in Fig. 125.17(d) marks the spatial range, where fringes are formed through back reflection from that region. The two to three upper and lower fringes that remain up to 4 ns are due to reflection from the shelf in the cone. [See Fig. 125.13(b).] A fringe shift indicates a change in the optical path length with time, i.e., through a movement of the reflecting surface or through an increase in plasma density along the probe path. In Fig. 125.17(c) the fringes start to shift downward after the onset of the main pulse (black curve), indicating plasma formation within the cone. The velocity of the boundary of the gold plasma is predicted to steadily increase to ~$5 \times 10^5$ cm/s at 3 ns, consistent with the observed fringe shift. With increasing ionization, a density gradient develops in front of the reflecting surface so that eventually the probe laser is completely absorbed, explaining the disappearance of the fringes at ~2.5 ns. For a 5-$\mu$m thickness, breakout is measured at 3.60 ns, based on two short vertical lines [marked by the white arrow in Fig. 125.17(c)] that are created by optical self-emission from the emerging shock wave at a wavelength of 532 nm. The two lines are exactly separated by the expected etalon delay[32] in the interferometer and provide a precise measurement of the breakout time. In contrast, the inner cone wall is well preserved for the 15-$\mu$m tip thickness, which is seen in Fig. 125.17(d), by the almost straight fringes up to the time of breakout.

### Integrated Fast-Electron–Heating Experiments

In preparation for each integrated fast-ignition experiment, the short-pulse laser is precisely timed with respect to the drive

laser and pointed into the cone tip. The accuracy of pointing for the short-pulse laser is ~15 $\mu$m as measured by x-ray pinhole images.[21] The timing is measured *in situ* with ±30-ps precision at full energy by measuring the temporally resolved hard x-ray emission produced by the short-pulse laser interaction.[21] The main diagnostic for inferring the coupling efficiency of short-pulse laser energy into the compressed core is the yield of thermonuclear neutrons that are produced by d(d,n)$^3$He reactions. A new liquid-scintillator time-of-flight detector was developed to measure the neutron yield in the presence of a strong hard x-ray background from the short-pulse laser.[33] This was required because standard plastic scintillator detectors were overwhelmed by the hard x-ray radiation and did not provide a useful measurement in integrated shots.[33] The liquid scintillator detector completely suppresses the background at the time when the 2.45-MeV neutrons arrive and provides reliable neutron-yield data. The details of the new detector and background mitigation techniques in fast-ignition integrated experiments are discussed in Ref. 33. Examples of the measured neutron spectra are shown in Fig. 125.18 for different timings and two target types. The spectrum for an early arrival (3.52 ns) of the short-pulse laser is very similar to spectra obtained without the short-pulse laser. The spectrum at a later time (3.62 ns) for a 10-$\mu$m flat tip shows a significant enhanced neutron signal, while the increase is not as pronounced for the 40-$\mu$m flat tip (3.65 ns). No attempt was made to extract an ion temperature from the noisy and broadened spectra. This is because of (i) limited number of detected neutrons (~10 to 40 particles), (ii) neutron scattering by a 2.5-cm-thick lead plate that shielded x rays and was located in the line of sight and by other structures adjacent to the detector, and (iii) broadening effects from a relatively large (~3 liter) detector volume. The neutron time-of-flight spectra are integrated to provide a total yield. The neutron detector was cross calibrated against another absolutely calibrated neutron detector[34] using a series of shots without the short-pulse laser.

The implosion produces thermonuclear neutrons in the hot, dense core surrounded by the cold shell; but neutrons are also generated in the corona of the plasma. The whole shell was deuterated and the drive laser heated the region between the critical and the ablation surface to temperatures >1 keV, which generated a significant amount of neutrons outside the dense shell. The corona yield ($0.73\pm0.08\times10^7$) was measured in a series of shots with cone-in-shell targets without the short-pulse laser, where the inside of the shell was coated with a CH plastic layer (1 to 5 $\mu$m) to quench the yield from the target center. The neutron yield was ~35% lower compared to pure CD shells and did not depend on the thickness of the CH layer. Previous experiments[35] showed that an inner 1-$\mu$m CH layer is sufficient to quench the fusion yield from the central region. Simulations show that fast-electron heating is insignificant in the region of the corona neutrons. The amount of fast-electron energy deposited in this region is negligible compared to the fast-electron energy coupled in the central plasma region. This justifies that the corona yield is treated as an offset and is subtracted from the measured yield.

Figure 125.19 shows the measured neutron yield as a function of the arrival time of the OMEGA EP pulse in the cone. Two types of targets were used. The red circles show the results for a 10-$\mu$m tip diameter and the blue triangles for a

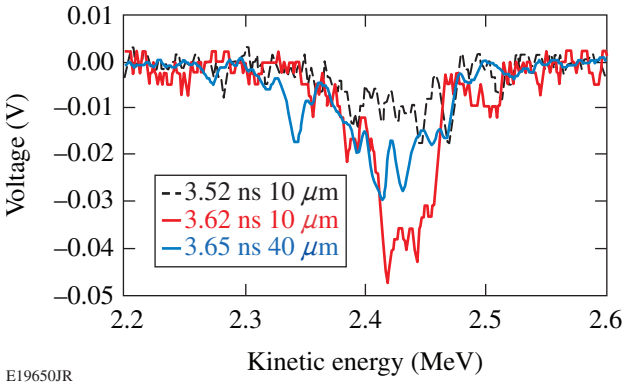


Figure 125.18
Time-of-flight spectra of 2.45-MeV neutrons from thermonuclear d(d,n)$^3$He reactions in integrated fast-ignition experiments. Spectra with various timings of the OMEGA EP beam are shown for two target types.

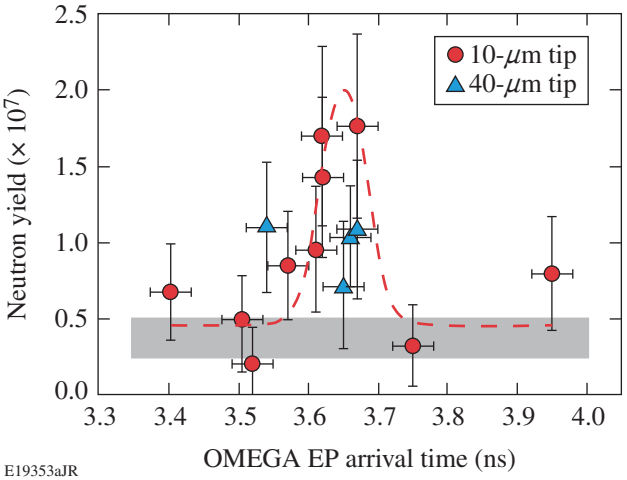


Figure 125.19
Measured neutron yield as a function of the arrival time of the short-pulse laser for two types of cone targets: 10-$\mu$m (circles) and 40-$\mu$m (triangles) tip diameter. The gray area represents data without the short-pulse laser.

larger tip (40 $\mu$m). The 10-$\mu$m data show a peak in neutron yield at a delay time of 3.65±0.02 ns. Most of the tips were 15 $\mu$m thick. The dashed curve is a fit of a Gaussian profile to the red circles. The gray bar shows the yield from several shots without the short-pulse beam, measured with a different detector that had smaller yield error. Most of the null shots were taken with the 10-$\mu$m-flat-tip cone target, but some null shots were also taken with the 40-$\mu$m flat tip. The same implosion yield was measured within the measurement uncertainty. The error bars include the error caused by neutron statistics and the cross-calibration error. The uncertainty in yield without the OMEGA EP pulse, indicated by the width of the gray bar, is lower because it represents an average over many shots using the more-accurate detector. The 10-$\mu$m data show an enhancement in neutron yield by more than a factor of 4 for the smaller-tip targets and a properly timed short-pulse beam. The experiments measured $(1.4\pm0.6)\times10^7$ additional neutrons resulting from heating by the short-pulse laser in a narrow time window of less than 100 ps. This corresponds to a coupling efficiency of 3.5±1.0% of the short-pulse energy into the core.[36]

It is expected that most of the OMEGA EP beam energy interacted with the side walls of the cone in the smaller-tip target, while a significant portion of laser energy interacted under normal incidence with the circular flat in the larger tip. It is surprising that the data from the larger tip may indicate a lower coupling efficiency. However, only four shots have been taken with this target type to date and more experiments are required covering a larger time range of OMEGA EP arrival times. The neutron peak might be shifted for the 40-$\mu$m tip. Hydrodynamic simulations are very similar for both targets and timing shifts of more than 50 ps are not expected. Possible causes for the difference in neutron yield are higher fast-electron conversion efficiency in the smaller tip and better electron transport. Intense laser–plasma interaction with cone-like structures might lead to a higher conversion efficiency into fast electrons[37] and enhanced surface acceleration of fast electrons.[38] It is expected that the density scale length plays an important role in the conversion efficiency and the directionality of the fast electrons.[39] A better understanding requires characterization of the preplasma (see below) and PIC simulations of the laser–plasma interaction.

Fast electrons that escaped the target were measured in two different directions with two absolutely calibrated electron spectrometers based on permanent magnets and image plates.[40] The spectrometers covered the energy range from 0.1 to 100 MeV. Figure 125.20 shows measured spectra in the laser's forward direction and sideways (at an angle of 79° to the laser axis). The spectra were measured simultaneously. Significant numbers of electrons were measured with kinetic energies up to several tens of MeV in both directions. The total number of escaped electrons was ~40% higher in the forward direction. The mean energy averaged over the whole range was ~5.1 MeV in the forward direction and ~3.7 MeV sideways. The slope temperature of the sideways curve is about 2 MeV in the 5- to 10-MeV range and is significantly higher than that expected based on ponderomotive scaling of the average laser intensity in vacuum. It is interesting to note that in the range up to 2 MeV, ~10× more fast electrons are measured sideways. This might be caused by the forward-generated electrons as they are stopped in the dense fuel assembly. Another possible explanation is that strong self-generated electric and magnetic fields affect the directionality of the emitted electrons.[41,42]

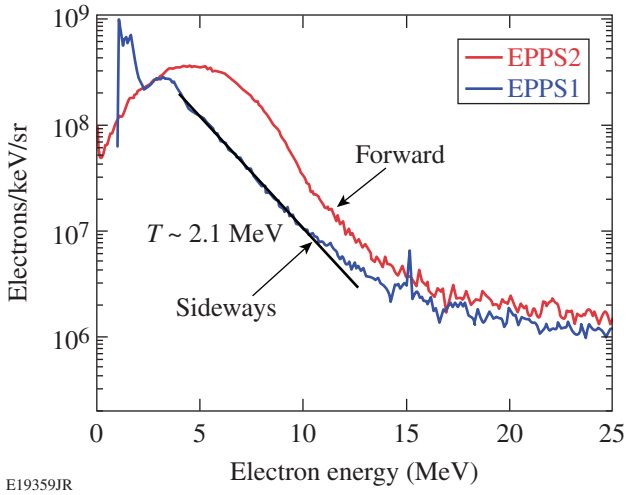


Figure 125.20
Fast-electron spectra measured in the laser's forward direction (red curve) and perpendicular to the laser direction (blue curve) (shot 59124).

The energy spectrum of the escaped electrons is only indirectly related to that of the generated electrons.[42] A few percent of the electrons are able to escape the target through the large Debye sheath fields that are formed at the plasma boundary. Escaping electrons lose energy to the sheath potential, which is a function of time, and therefore the spectrum of the escaping electrons is modified. Assuming that the forward-electron component is emitted into a cone with a 45° half-angle and that the colder distribution is emitted sideways from 90° to 45° with respect to the laser direction, it is estimated that the total energy carried away by the fast electrons is ~7.3 J, which corresponds to ~0.8% of the OMEGA EP pulse energy. Assuming a conversion efficiency of ~20% to 30% of laser energy into fast electrons,[23,43] a few percent of the fast electrons escaped

the target as expected. The estimate is not very sensitive on the half-angle of the forward-going component. For example, a total energy of ~5.8 J is estimated for a 10° half-angle.

The higher electron energies may be caused by cone filling by a preplasma. Self-focusing and beam filamentation in this preplasma seeded by the OMEGA EP beam nonuniformities may explain the observed hard electron spectrum.[24] Filamentary structures in an under-dense plasma with periodicity orthogonal to the laser beam direction can be driven by thermal,[44] ponderomotive,[45] and relativistic effects.[46] The last two are probably the dominant effects for the present experiment. An incident light beam that is slightly more intense in one region results in a lateral force, pushing the plasma electrons sideways from the region of highest laser intensity and leaving behind a region of lower electron density, $n_e$. This results in a transversal modulation of the index of refraction, $n = \sqrt{1 - n_e / n_c}$, where $n_c$ is the critical density. The slightly increased index of refraction in the depleted region causes the wave front to curve in such a way that light is focused into the region of high intensity, which is counteracted by diffraction. The process leads to a positive feedback and results into what is known as the filamentation instability. Filamentation and self-focusing can therefore lead to much higher laser intensities than in vacuum and produce a hotter electron population, which was observed in this experiment. Some portion of the laser light may be transported in these filaments, at higher intensities, deeper into the preplasma. This effect was observed in 2-D PIC simulations for similar experimental conditions.[24]

**Integrated Simulations and Discussion**

*DRACO*[47] + *LSP*[48] simulations were performed to estimate the coupling of fast electrons to the compressed CD.[36] *DRACO* simulated the fuel assembly in cylindrical geometry and was coupled with the implicit hybrid PIC code *LSP* to calculate the fast-electron propagation and energy deposition in the target.[4,10] In the simulation, the Au cone tip had an inner diameter of 40 $\mu$m, a wall thickness of 15 $\mu$m, and a cone half-angle of 37°. The cone tip was 55 $\mu$m away from the center of the shell. The laser–plasma interaction was not modeled. The simulation assumed a fast-electron beam that was promoted from thermal electrons at the inside of the cone wall with an initial full-angle spread of 110°. Various experimental[49,50] and theoretical work[51] indicates that a full angle of about 100° for the MeV electrons is a reasonable number for the initial divergence angle. The electron-transport calculation through the gold cone included scattering. Similar to the experimental observation, the injection time of the fast electrons was chosen ~50 ps before shock breakout at a time when the shock wave was transiting through the cone wall. An exponential energy distribution was assumed for the fast electrons with a mean energy given by the maximum of the ponderomotive[52] and Beg[53] scalings. The total energy of the fast electrons generated at the inside cone wall contained 16% of the OMEGA EP beam energy with a fast-electron temperature of ~0.3 MeV.

Initial *DRACO* runs without the OMEGA EP beam yielded higher neutron numbers than measured, indicating higher density and temperature in the simulation. The fusion-reaction rate is highly sensitive to the density and temperature distribution in the assembled fuel. Beside an over-predicted density, mainly the higher temperature leads to a higher yield because the fusion reactivity roughly varies with the fourth power of the ion temperature in the range of interest. A number of effects contribute to the over-prediction. Radiation transport was not included and a uniform drive over the shell was assumed that is too optimistic. Low-adiabat implosions with plastic shells and high-convergence ratio are strongly RT instable during the deceleration phase, giving rise to mixing of cold-shell material into hotter parts of the plasma, which quenches the fusion reaction and leads to lower temperatures than predicted.[18] The presence of the cone also leads to a reduction in ion temperature. Neutron and proton measurements from $D^3He$-filled cone-in-shell targets have shown that measured ion temperatures are a factor of 2 lower than predicted, while $\rho R$ is reduced by only 30%.[26] This shows that the cone affects the ion temperature much more than $\rho R$. The ion temperature was, therefore, reduced in the simulation to obtain a neutron yield consistent with the experiment. To match the neutron yield when the OMEGA EP beam is not fired, the temperature had to be reduced by a factor of 2.1 in the shell and a factor of 1.4 in the plasma region in front of the cone tip, which was heated by a shock that bounced back from the cone tip.

Figure 125.21(a) shows the ion temperature of the target without and with hot-electron heating. The simulation shows that the imploded shell material was pushed against the cone tip and was heated strongly up to ~2 keV. Fast electrons deposited more than 50% of their energy in the cone wall, which was strongly heated. Radiation cooling was not included in the simulation, and the temperature in gold was artificially clamped to 1 keV. Most of the fast electrons that were transmitted through the cone wall deposited their energy in the lower-density plasma (>2 g/cm$^3$) close to the tip of the cone between the tip and the core. From Fig. 125.21(b), the peak neutron-production density occurred at the core in the absence of hot electrons. With hot electrons, the neutron-production density is largest just to the left of the tip of the cone ($Z \approx 60$ $\mu$m). The simulation obtained

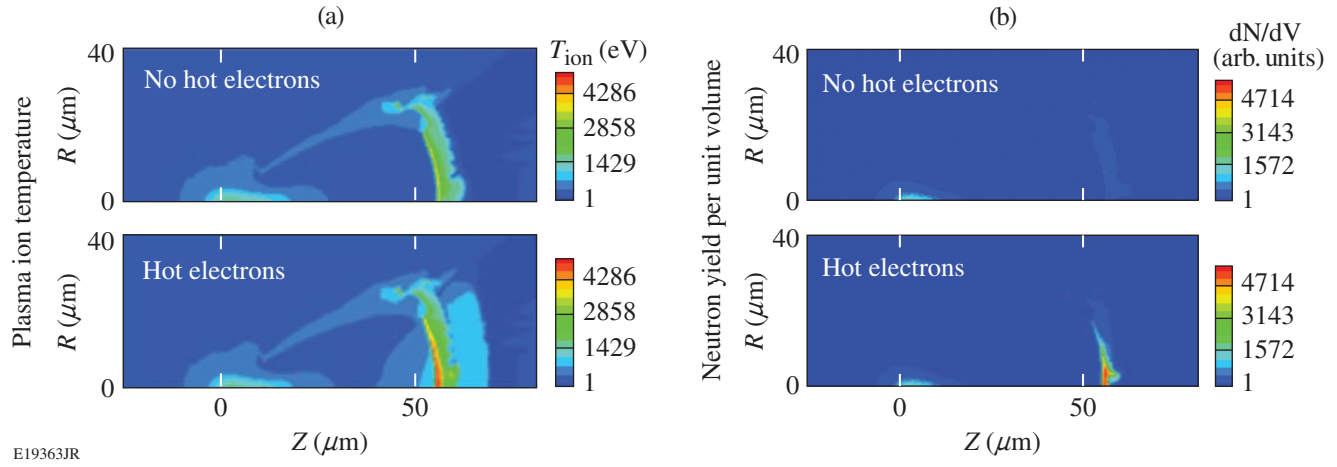


Figure 125.21
*DRACO* + *LSP* simulation for a 10-ps, 1.0-kJ, $R_{80}$ = 27-$\mu$m OMEGA EP pulse, showing contours of (a) plasma ion temperature and (b) neutron yield per unit volume, with and without hot electrons produced by the OMEGA EP pulse.

a neutron-yield enhancement of $1.4 \times 10^7$, which required that 3.5±1.0% of the OMEGA EP energy was coupled into the CD by fast electrons. Some fraction of fast electrons left the target without significant heating. According to the simulation, only about 0.4% of the OMEGA EP energy coupled to densities above 100 g/cm$^3$.

The current results are now compared to previous integrated experiments. An integrated experiment performed on Rutherford Appleton Laboratory's VULCAN Laser studied the flux of high-intensity laser-generated electrons via a hollow cone into a laser-imploded plasma.[42] The shell was imploded by six 900-J, 1-ns laser beams at 1.05-$\mu$m wavelength, and a 10-ps, 70-J laser pulse was focused into a hollow Au cone with a peak intensity of ~$3 \times 10^{18}$ W/cm$^2$ in vacuum. The compressed densities and areal densities were more than an order of magnitude lower than in the present case. The cone had similar dimensions with a tip thickness of 10 $\mu$m. The flux of high-energy electrons traversing the imploded CD was determined from comparing the measured $K_\alpha$ fluorescence yield from a Cu dopant in the shell to Monte Carlo simulations that modeled the fast-electron transport in the CD and calculations of the $K_\alpha$ yield. It was estimated that ~7% to 22% of the short-pulse laser energy was converted into fast electrons in the CD, depending on the assumed hot-electron temperature.[42] This number seems higher than what is reported here, but electron-transport modeling indicates that only a small fraction of the fast-electron energy (~9%) was actually deposited into the CD in the VULCAN experiment. The model in Ref. 42 did not include the physics of electron transport in the cone wall, which might affect the inferred coupling efficiency. Our modeling shows that fast-electron transport is very sensitive to scattering in the high-$Z$ material and is influenced by resistive magnetic fields at the high-$Z$ cone walls.[36]

Integrated experiments were performed about a decade ago on the GEKKO XII Laser System in Japan.[12] A 500-$\mu$m-diam, 7-$\mu$m-thick CD shell was imploded by nine beams at a wavelength of 0.53 $\mu$m and with an energy of 2.5 kJ with 1.2-ns, flat-top pulses. The compressed density was estimated with 50 to 100 g/cm$^3$. Similar peak densities were obtained in our experiment but with significantly higher drive energy and a shaped UV drive pulse. No shock-breakout measurements were reported in Ref. 12. With a 300-J, 0.6-ps (0.5-PW) heating beam, ~$2 \times 10^7$ neutrons were reported compared to 2 to $5 \times 10^4$ with no heating beam. The time window in which the enhancement was observed was ~80 ps, which is very similar to our measurement. Simple predictions of the neutron yield normalized to the yield without heating were used to derive a coupling of 15% to 30% of laser energy to core heating.[12] These numbers are considerably higher than the number reported here. The coupling efficiency here is based on comparing the measured heating neutron yield to more sophisticated integrated simulations that include the hydrodynamics and the fast-electron transport through the cone wall and into the fuel assembly. Possible explanation of the difference in coupling efficiency is a different level of preplasma formation.

Recent integrated experiments at GEKKO XII with the new LFEX short-pulse laser[54] were not able to reproduce the previous results and measured neutron yields are significantly lower.[55] This is attributed to the formation of a preplasma in the

cone by a laser prepulse or pedestal. Short-pulse experiments with cone-like structures on the TITAN Laser at LLNL and on the LULI 100 TW Laser in France revealed the presence of preplasma over 100 $\mu$m away from the cone tip for very similar laser contrast.[56,57] It was shown in Ref. 24 that a preformed plasma in a hollow cone strongly influences the ultra-intense laser–plasma interaction and the hot-electron generation. The laser beam filamented in the underdense plasma and the laser energy was diverted from the cone tip for large preplasmas. The laser beam propagation halted and energetic electrons were generated mostly transverse to the incoming beam.[24]

Two-dimensional simulations were performed with the radiation–hydrodynamics code *HYDRA*[58] to study the preplasma formation for the present case using the measured prepulse. Figure 125.22 shows the simulated density contours for the smaller tip diameter. A preplasma fills the cone, and the nonrelativistic critical density shifts ~100 $\mu$m away from the original position of the inner cone wall at the time when the main pulse is incident. Results for the larger tip were similar but had slight differences in the shape of the density contours. An experimental characterization of the preplasma in the cone is important and will be performed in the future.

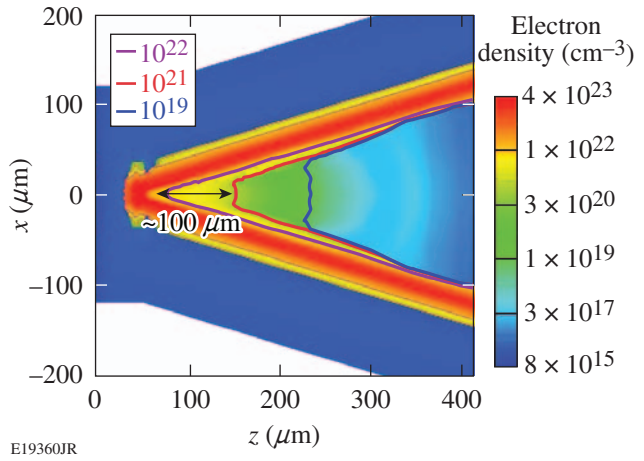


Figure 125.22
Electron-density contours from a 2-D *HYDRA* simulation at the time of the short-pulse interaction of the preplasma formation in a gold cone with inner tip diameter of 10 $\mu$m.

The integrated simulations were based on the assumption of a relatively low fast-electron temperature from the average intensity in vacuum. More heating of the dense portion of the core is expected with a hotter-electron distribution, which is expected from laser interactions with a preformed plasma. This requires large-scale PIC simulations that model the details of the laser–preplasma interaction and couple these results to the integrated simulations. Such large-scale PIC simulations will be performed in the future.

**Summary**

The fast-ignitor, cone-in-shell target concept has been investigated at the OMEGA Laser Facility. Initial integrated fast-ignition experiments with room-temperature re-entrant cone targets were performed using a shaped laser pulse to implode the capsule with 20 kJ of UV energy on a low adiabat, followed by a 1-kJ, 10-ps, short-pulse IR beam interacting with a hollow gold cone at various times with respect to the driver laser.

Shock-breakout measurements have been performed with cone-in-shell targets under the same drive conditions, but without the short-pulse laser. The measurements confirm an intact cone tip at the time of peak neutron production in the integrated shots. VISAR measurements show that Au cones with a thin tip (5 $\mu$m) are affected by x-ray preheat that is produced in the corona of the imploding shell. This leads to premature material release inside the hollow cone, which might affect the short-pulse laser interaction. The thicker cone walls (15 $\mu$m Au) that were used in the integrated shots are well shielded against the x rays and are not affected by preheat.

In the integrated shots, a fourfold increase in neutron yield was observed by short-pulse heating in a narrow (~100-ps) time window close to peak compression. The additional (1.4±0.6) × $10^7$ neutrons produced by the short-pulse beam correspond to a coupling efficiency of 3.5±1.0% of short-pulse energy into the CD, according to simulations with the integrated *DRACO* + *LSP* codes.

Electrons with energies higher than 20 MeV were measured in the direction of the short-pulse laser and perpendicular to it. More escaping electrons were measured in the forward direction, integrated over the whole energy range, but for energies below 2 MeV a significant depletion was observed in the spectrum through the dense plasma.

Integrated simulations show significant target heating in the lower-density CD plasma adjacent to the cone tip, which is where most of the additional neutrons are created. The simulations assumed a hot-electron temperature based on ponderomotive scaling of the laser intensity in vacuum and no preplasma. Additional two-dimensional hydrodynamic simulations using the measured laser prepulse indicate a significant production of preplasma in the cone. Laser interaction with and filamentation in a lower-density preplasma might consequently lead to much

higher laser intensities and produce a hotter-electron distribution. There is evidence for this from the measured spectra of escaped electrons showing significantly higher mean energy than expected.

This work addresses a number of important issues for fast ignition, which include cone survivability and the tradeoff of matching the cone thickness to the fast-electron energy. More work must be done to optimize the target geometry and materials. This also includes improvements in the short-pulse–laser contrast, a smaller focus, and a higher energy. It is expected that these improvements will increase the coupling efficiency and lead to a greater enhancement in the number of neutrons. Simulations were performed with a smaller focus ($R_{80} = 15\ \mu$m) and higher laser energy (2.6 kJ) without contrast degradation, leading to a fourfold increase in coupling efficiency to densities above 100 g/cm$^3$. Integrated experiments with improved laser parameters will be performed in the future.

## ACKNOWLEDGMENT

This work was supported by the U.S. Department of Energy Office of Inertial Confinement Fusion under Cooperative Agreement No. DE-FC52-08NA28302, the OFES Fusion Science Center grant No. DE-FC02-04ER54789, the OFES ACE Fast Ignition grant No. DE-FG02-05ER54839, the DOE Laboratory Basic Science Program, the University of Rochester, and the New York State Energy Research and Development Authority. The support of DOE does not constitute an endorsement by DOE of the views expressed in this article.

## REFERENCES

1. N. G. Basov, S. Yu. Gus'kov, and L. P. Feokistov, J. Sov. Laser Res. **13**, 396 (1992).
2. M. Tabak *et al.*, Phys. Plasmas **1**, 1626 (1994).
3. R. Betti and C. Zhou, Phys. Plasmas **12**, 110702 (2005).
4. A. A. Solodov, K. S. Anderson, R. Betti, V. Gotcheva, J. Myatt, J. A. Delettrez, S. Skupsky, W. Theobald, and C. Stoeckl, Phys. Plasmas **15**, 112702 (2008).
5. S. Atzeni *et al.*, Phys. Plasmas **15**, 056311 (2008).
6. J. J. Honrubia and J. Meyer-ter-Vehn, Plasma Phys. Control. Fusion **51**, 014008 (2009).
7. A. J. Kemp, Y. Sentoku, and M. Tabak, Phys. Rev. Lett. **101**, 075004 (2008).
8. J. R. Davies *et al.*, Phys. Rev. E **56**, 7193 (1997).
9. A. R. Bell and R. J. Kingham, Phys. Rev. Lett. **91**, 035003 (2003).
10. A. A. Solodov, K. S. Anderson, R. Betti, V. Gotcheva, J. F. Myatt, J. A. Delettrez, S. Skupsky, W. Theobald, and C. Stoeckl, Phys. Plasmas **16**, 056309 (2009).
11. P. A. Norreys *et al.*, Phys. Plasmas **7**, 3721 (2000).
12. R. Kodama *et al.*, Nature **412**, 798 (2001); R. Kodama *et al.*, Nature **418**, 933 (2002).
13. T. R. Boehly, D. L. Brown, R. S. Craxton, R. L. Keck, J. P. Knauer, J. H. Kelly, T. J. Kessler, S. A. Kumpan, S. J. Loucks, S. A. Letzring, F. J. Marshall, R. L. McCrory, S. F. B. Morse, W. Seka, J. M. Soures, and C. P. Verdon, Opt. Commun. **133**, 495 (1997).
14. L. J. Waxer, D. N. Maywar, J. H. Kelly, T. J. Kessler, B. E. Kruschwitz, S. J. Loucks, R. L. McCrory, D. D. Meyerhofer, S. F. B. Morse, C. Stoeckl, and J. D. Zuegel, Opt. Photonics News **16**, 30 (2005).
15. V. N. Goncharov, T. C. Sangster, T. R. Boehly, S. X. Hu, I. V. Igumenshchev, F. J. Marshall, R. L. McCrory, D. D. Meyerhofer, P. B. Radha, W. Seka, S. Skupsky, C. Stoeckl, D. T. Casey, J. A. Frenje, and R. D. Petrasso, Phys. Rev. Lett. **104**, 165001 (2010).
16. General Atomics, San Diego, CA, 92123.
17. C. Stoeckl, T. R. Boehly, J. A. Delettrez, S. P. Hatchett, J. A. Frenje, V. Yu. Glebov, C. K. Li, J. E. Miller, R. D. Petrasso, F. H. Séguin, V. A. Smalyuk, R. B. Stephens, W. Theobald, B. Yaakobi, and T. C. Sangster, Phys. Plasmas **14**, 112702 (2007).
18. C. D. Zhou, W. Theobald, R. Betti, P. B. Radha, V. A. Smalyuk, D. Shvarts, V. Yu. Glebov, C. Stoeckl, K. S. Anderson, D. D. Meyerhofer, T. C. Sangster, C. K. Li, R. D. Petrasso, J. A. Frenje, and F. H. Séguin, Phys. Rev. Lett. **98**, 025004 (2007).
19. T. R. Boehly, V. A. Smalyuk, D. D. Meyerhofer, J. P. Knauer, D. K. Bradley, R. S. Craxton, M. J. Guardalben, S. Skupsky, and T. J. Kessler, J. Appl. Phys. **85**, 3444 (1999).
20. Y. Lin, T. J. Kessler, and G. N. Lawrence, Opt. Lett. **21**, 1703 (1996).
21. W. Theobald, K. S. Anderson, R. Betti, R. S. Craxton, J. A. Delettrez, J. A. Frenje, V. Yu. Glebov, O. V. Gotchev, J. H. Kelly, C. K. Li, A. J. MacKinnon, F. J. Marshall, R. L. McCrory, D. D. Meyerhofer, J. F. Myatt, P. A. Norreys, P. M. Nilson, P. K. Patel, R. D. Petrasso, P. B. Radha, C. Ren, T. C. Sangster, W. Seka, V. A. Smalyuk, A. A. Solodov, R. B. Stephens, C. Stoeckl, and B. Yaakobi, Plasma Phys. Control. Fusion **51**, 124052 (2009).
22. J. Bromage, S.-W. Bahk, D. Irwin, J. Kwiatkowski, A. Pruyne, M. Millecchia, M. Moore, and J. D. Zuegel, Opt. Express **16**, 16561 (2008).
23. P. M. Nilson, A. A. Solodov, J. F. Myatt, W. Theobald, P. A. Jaanimagi, L. Gao, C. Stoeckl, R. S. Craxton, J. A. Delettrez, B. Yaakobi, J. D. Zuegel, B. E. Kruschwitz, C. Dorrer, J. H. Kelly, K. U. Akli, P. K. Patel, A. J. MacKinnon, R. Betti, T. C. Sangster, and D. D. Meyerhofer, Phys. Rev. Lett. **105**, 235001 (2010).
24. A. G. MacPhee *et al.*, Phys. Rev. Lett. **104**, 055002 (2010).
25. C. Dorrer, D. Irwin, A. Consentino, and J. Qiao, presented at the ICUIL 2010 Conference, Watkins Glen, NY, 26 September–1 October 2010 (Paper ThO3).
26. C. Stoeckl, T. R. Boehly, J. A. Delettrez, S. P. Hatchett, J. A. Frenje, V. Yu. Glebov, C. K. Li, J. E. Miller, R. D. Petrasso, F. H. Séguin, V. A.

Smalyuk, R. B. Stephens, W. Theobald, B. Yaakobi, and T. C. Sangster, Plasma Phys. Control. Fusion **47**, B856 (2005).

27. J. E. Miller, T. R. Boehly, A. Melchior, D. D. Meyerhofer, P. M. Celliers, J. H. Eggert, D. G. Hicks, C. M. Sorce, J. A. Oertel, and P. M. Emmel, Rev. Sci. Instrum. **78**, 034903 (2007).

28. P. M. Celliers, D. K. Bradley, G. W. Collins, D. G. Hicks, T. R. Boehly, and W. J. Armstrong, Rev. Sci. Instrum. **75**, 4916 (2004).

29. R. S. Craxton and R. L. McCrory, J. Appl. Phys. **56**, 108 (1984).

30. J. Delettrez, R. Epstein, M. C. Richardson, P. A. Jaanimagi, and B. L. Henke, Phys. Rev. A **36**, 3926 (1987); M. C. Richardson, P. W. McKenty, F. J. Marshall, C. P. Verdon, J. M. Soures, R. L. McCrory, O. Barnouin, R. S. Craxton, J. Delettrez, R. L. Hutchison, P. A. Jaanimagi, R. Keck, T. Kessler, H. Kim, S. A. Letzring, D. M. Roback, W. Seka, S. Skupsky, B. Yaakobi, S. M. Lane, and S. Prussin, in *Laser Interaction and Related Plasma Phenomena*, edited by H. Hora and G. H. Miley (Plenum Publishing, New York, 1986), Vol. 7, pp. 421–448.

31. D. R. Lide, *CRC Handbook of Chemistry and Physics*, 82nd ed. (CRC Press, Boca Raton, FL, 2001), p. 4-132.

32. W. Theobald, J. E. Miller, T. R. Boehly, E. Vianello, D. D. Meyerhofer, T. C. Sangster, J. Eggert, and P. M. Celliers, Phys. Plasmas **13**, 122702 (2006).

33. C. Stoeckl, M. Cruz, V. Yu. Glebov, J. P. Knauer, R. Lauck, K. Marshall, C. Mileham, T. C. Sangster, and W. Theobald, Rev. Sci. Instrum. **81**, 10D302 (2010); R. Lauck *et al*., IEEE Trans. Nucl. Sci. **56**, 989 (2009).

34. V. Yu. Glebov, C. Stoeckl, T. C. Sangster, S. Roberts, G. J. Schmid, R. A. Lerche, and M. J. Moran, Rev. Sci. Instrum. **75**, 3559 (2004).

35. F. J. Marshall, J. A. Delettrez, R. Epstein, V. Yu. Glebov, D. R. Harding, P. W. McKenty, D. D. Meyerhofer, P. B. Radha, W. Seka, S. Skupsky, V. A. Smalyuk, J. M. Soures, C. Stoeckl, R. P. Town, B. Yaakobi, C. K. Li, F. H. Séguin, D. G. Hicks, and R. D. Petrasso, Phys. Plasmas **7**, 2108 (2000).

36. W. Theobald, A. A. Solodov, C. Stoeckl, K. S. Anderson, R. Betti, T. R. Boehly, R. S. Craxton, J. A. Delettrez, C. Dorrer, J. A. Frenje, V. Yu. Glebov, H. Habara, K. A. Tanaka, J. P. Knauer, R. Lauck, F. J. Marshall, K. L. Marshall, D. D. Meyerhofer, P. M. Nilson, P. K. Patel, T. C. Sangster, W. Seka, N. Sinenian, T. Ma, F. N. Beg, and R. B. Stephens, "Integrated Fast-Ignition Core-Heating Experiments on OMEGA," submitted to Physical Review Letters.

37. W. Theobald, V. Ovchinnikov, S. Ivancic, B. Eichman, P. M. Nilson, J. A. Delettrez, R. Yan, G. Li, F. J. Marshall, D. D. Meyerhofer, J. F. Myatt, C. Ren, T. C. Sangster, C. Stoeckl, J. D. Zuegel, L. Van Woerkom, R. R. Freeman, K. U. Akli, E. Giraldez, and R. B. Stephens, Phys. Plasmas **17**, 103101 (2010).

38. H. Habara *et al*., Phys. Rev. Lett. **97**, 095004 (2006).

39. M. I. K. Santala *et al*., Phys. Rev. Lett. **84**, 1459 (2000).

40. H. Chen *et al*., Rev. Sci. Instrum. **79**, 10E533 (2008).

41. T. Yabuuchi *et al*., New J. Phys. **11**, 093031 (2009).

42. M. H. Key, J. C. Adam, K. U. Akli, M. Borghesi, M. H. Chen, R. G. Evans, R. R. Freeman, H. Habara, S. P. Hatchett, J. M. Hill, A. Heron, J. A. King, R. Kodama, K. L. Lancaster, A. J. MacKinnon, P. Patel, T. Phillips, L. Romagnani, R. A. Snavely, R. Stephens, C. Stoeckl, R. Town, Y. Toyama, B. Zhang, M. Zepf, and P. A. Norreys, Phys. Plasmas **15**, 022701 (2008).

43. C. D. Chen *et al*., Phys. Plasmas **16**, 082705 (2009).

44. O. Willi and P. T. Rumsby, Opt. Commun. **37**, 45 (1981).

45. B. I. Cohen and C. E. Max, Phys. Fluids **22**, 1115 (1979).

46. C. Max, J. Arons, and A. B. Langdon, Phys. Rev. Lett. **33**, 209 (1974).

47. P. B. Radha, T. J. B. Collins, J. A. Delettrez, Y. Elbaz, R. Epstein, V. Yu. Glebov, V. N. Goncharov, R. L. Keck, J. P. Knauer, J. A. Marozas, F. J. Marshall, R. L. McCrory, P. W. McKenty, D. D. Meyerhofer, S. P. Regan, T. C. Sangster, W. Seka, D. Shvarts, S. Skupsky, Y. Srebro, and C. Stoeckl, Phys. Plasmas **12**, 056307 (2005).

48. D. R. Welch *et al*., Nucl. Instrum. Methods Phys. Res. A **464**, 134 (2001).

49. M. Storm, A. A. Solodov, J. F. Myatt, D. D. Meyerhofer, C. Stoeckl, C. Mileham, R. Betti, P. M. Nilson, T. C. Sangster, W. Theobald, and C. Guo, Phys. Rev. Lett. **102**, 235004 (2009).

50. J. S. Green, V. M. Ovchinnikov, R. G. Evans, K. U. Akli, H. Azechi, F. N. Beg, C. Bellei, R. R. Freeman, H. Habara, R. Heathcote, M. H. Key, J. A. King, K. L. Lancaster, N. C. Lopes, T. Ma, A. J. MacKinnon, K. Markey, A. McPhee, Z. Najmudin, P. Nilson, R. Onofrei, R. Stephens, K. Takeda, K. A. Tanaka, W. Theobald, T. Tanimoto, J. Waugh, L. Van Woerkom, N. C. Woolsey, M. Zepf, J. R. Davies, and P. A. Norreys, Phys. Rev. Lett. **100**, 015003 (2008).

51. C. Ren *et al*., Phys. Plasmas **13**, 056308 (2006).

52. S. C. Wilks and W. L. Kruer, IEEE J. Quantum Electron. **33**, 1954 (1997).

53. F. N. Beg *et al*., Phys. Plasmas **4**, 447 (1997).

54. J. Kawanaka *et al*., J. Phys., Conf. Ser. **112**, 032006 (2008).

55. H. Azechi, Bull. Am. Phys. Soc. **55**, 291 (2010).

56. L. Van Woerkom *et al*., Phys. Plasmas **15**, 056304 (2008).

57. S. D. Baton *et al*., Phys. Plasmas **15**, 042706 (2008).

58. M. M. Marinak *et al*., Phys. Plasmas **3**, 2070 (1996).

# Submicrometer-Resolution Mapping of Ultraweak 355-nm Absorption in $HfO_2$ Monolayers Using Photothermal Heterodyne Imaging

## Introduction

Thin-film coatings for near-ultraviolet (UV), nanosecond (ns)-pulse–laser applications are usually comprised of metal oxide as the high-index component and silica oxide as the low-index material. High-resolution studies of laser-damage morphology[1] reveal two important facts about ns-pulsed–laser damage in these coatings: First, metal oxide is the weakest part and is where damage is initiated. Second, at close-to-threshold conditions, damage takes the form of submicrometer-sized craters. Such morphology indicates that the damage process starts at isolated sites and can be linked to localized absorbers, like few-nanometer–sized metal clusters,[2] or high-density electronic defect areas. Deposition of metal oxide using metal as a starting material provides the possibility for cluster formation. On the other hand, electronic defects are always present in metal-oxide dielectric materials, even in bulk form.[3] In thin-film coatings, characterized by columnar structure and large internal surfaces, submicrometer-scale electronic defect density enhancements might be expected. Clarification of the exact nature and distribution of damage precursors is essential for further improvements in damage resistance of coating materials. In this work, we make an attempt to evaluate spatial distribution of absorbers in hafnia ($HfO_2$) monolayers by using photothermal heterodyne imaging (PHI).[4] High sensitivity to absorption and true submicrometer resolution of this technique, developed specifically for nanoscale absorber detection and characterization, was demonstrated[4,5] by imaging embedded gold nanoparticles with the smallest diameter of 1.4 nm. To gain insight into the damage mechanism, our present study of PHI mapping of hafnia monolayers before and after laser irradiation is complemented by atomic force microscopy (AFM) analysis of damage morphology. This article is organized as follows: first, we describe the PHI principle, setup for sample mapping, and system calibration; then sample preparation and characterization, followed by the results of PHI mapping of differently prepared $HfO_2$ monolayers prior to laser irradiation. Next, we present the results of damage-site mapping using PHI and AFM and discuss possible damage mechanisms and the nature of damage-initiating absorbers. Finally, the conclusions are presented.

## Experimental

1. The PHI Principle and Setup

Like other versions of photothermal techniques, PHI relies on the presence of a modulated pump beam that causes local modulated heating of the material and of a probe beam that experiences modification (deflection, focusing, scattering, etc.) while passing through the heated volume. In the case of PHI (see Fig. 125.23), both the pump and probe beams are focused into an overlapping, very tight, preferably diffraction limited spot inside the material. A very small absorbing defect, being covered by such a spot, heats up and, by heat conduction, causes the temperature $T$ to rise in the surrounding host material. This process leads to a variation in the host refractive index $n$ according to $n = n(T)$ and, consequently, probe light scattering. Moreover, because of scatterer-size modulation, the probe laser's frequency $\omega$ is shifted by an amount equal to the modulation frequency $\Omega$. Following the description in Ref. 5, the interference between scattered and propagating (or reflected, for back configuration) probe light in the far field creates a beat signal with intensity $I(\Omega)$:

$$I(\Omega) \sim I_{\text{pump}} I_{\text{probe}}\, n \partial n \big/ \partial T \lambda^{-2} w^{-1} F(\Omega),$$

where $I_{\text{pump}}$ and $I_{\text{probe}}$ are the pump and probe intensities, $\lambda$ and $w$ are the probe wavelength and beam waist, respectively, and $F(\Omega)$ is a function describing heat conduction.

The experimental setup for PHI is shown in Fig. 125.24. A diode-pumped, continuous-wave (cw) semiconductor laser operating at 355-nm, 40-mW maximum output power (6 mW on sample) served as the pump laser, and a HeNe laser [633 nm, 10 mW (5 mW on sample)] was used as the probe. An acousto-optic modulator provided pump modulation in the frequency range of 100 kHz to 1 MHz, and only one beam diffracted into the first order was used as a pump. Pump and probe beams were combined at the entrance of the 40×, 0.95-N.A. (numerical aperture) microscope objective focusing both beams onto the sample mounted on the nanopositioning stage (Physik Instrumente). The stage had a minimum lateral step size of 10 nm, a maximum scan size of 200 $\mu$m, and an axial displacement of

20 $\mu$m. Probe light can be collected by either the same objective (back configuration) or an additional lens (forward configuration) and detected by a fast photodiode, lock-in amplifier (30-ms integration time), and a LabView-based data acquisition system. In the case of a back configuration, a quarter-wave plate and polarizing beam splitter were added to isolate the signal beam from the source. A detailed analysis of signals detected in either configuration can be found in Ref. 5. In this work, most measurements were performed using a forward configuration and 350-kHz modulation frequency.

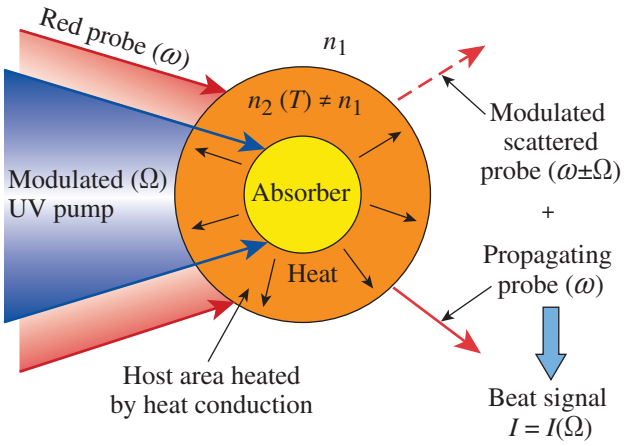


Figure 125.23
Schematic of photothermal heterodyne signal formation.

2. PHI-Setup Characterization and Calibration

Pump- and probe-beam focus spots were combined and characterized using a 1-$\mu$m pinhole in a metal foil. The pinhole was mounted on the nanopositioning stage using a sample holder and scanned across the beam. A corresponding image of the pump and probe beams' combined focal spot is shown in Fig. 125.25. A cross section through this image gives a full-width-at-half-maximum (FWHM) value of 0.79 $\mu$m, which should be considered an upper limit because of the transfer function of the pinhole. We estimated a real FWHM value ~10% to 15% smaller, or ~0.7 $\mu$m. Using this beam size and a maximum UV power on the sample of 6 mW, maximum power densities on the sample did not exceed ~1.6 MW/cm$^2$. For the system's spatial resolution and sensitivity characterization, we used 5- to 14-nm-diam isolated gold nanoparticles embedded inside silica film.[6] Figure 125.26 presents a 6-$\mu$m PHI scan and cross-sectional data for a sample with 14-nm particles, which show that a single particle is imaged as a feature with FWHM = 0.42 $\mu$m and that two particles separated by 0.55 $\mu$m can be clearly resolved. Also, particles as small as 5 nm were imaged using this setup. These calibration results proved both the true submicron spatial resolution and high sensitivity of the system. To characterize setup response in the case of homogeneous absorption, a $TiO_2$ film of ~200-nm thickness and 49% transmission at 355 nm was deposited on a fused-silica substrate. Figure 125.27 shows PHI signal dependence as a function of the pump laser's output power. It should be

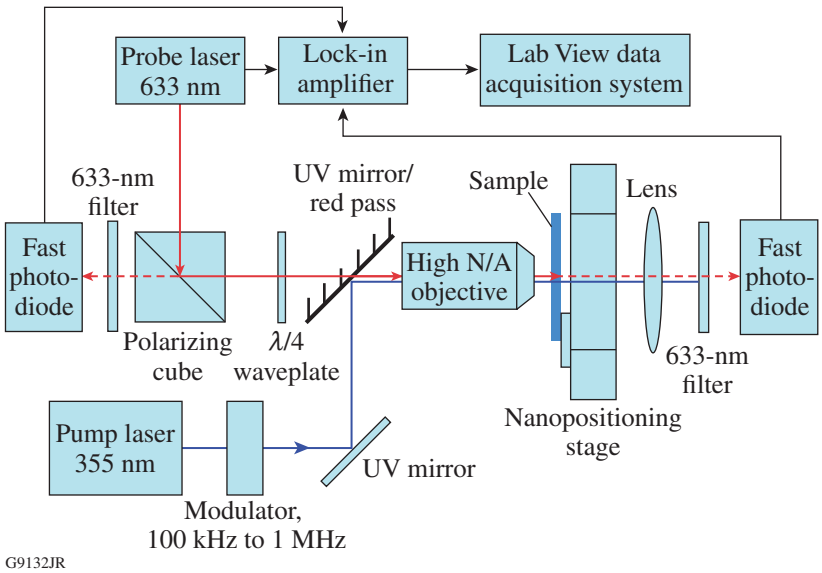


Figure 125.24
PHI setup for signal detection in a forward and backward configuration.

noted here that starting with powers of a few mW or higher, the signal declined as the exposure time was increased. Data shown in Fig. 125.27 were taken right after the beam shutter was opened. This effect can be attributed to some kind of sample bleaching during exposure. Consequently, it indicates that a strongly absorbing $TiO_2$ film is not the best solution to calibrate systems that rely on tightly focused beams. Still, with a measured noise level of 0.5 $\mu$V and maximum PHI signal detected ~6000 $\mu$V, the signal-to-noise ratio was >$10^4$, which proves the high sensitivity of this PHI setup.

3. $HfO_2$ Sample

$HfO_2$ thin-film monolayer coatings, 179 nm thick (1-wave optical thickness at 355 nm), were deposited by electron-beam (e-beam) evaporation using either conventional or plasma-assisted (argon/oxygen mixture) deposition. The conventional e-beam deposition rate was 1.2 Å/s and the oxygen pressure was $8 \times 10^{-5}$ Torr; in the case of the plasma-assisted deposition, the rate was –0.8 Å/s and the plasma source was operated at 180 V, 35 A. The latter was deliberately not optimized in order to produce samples with varying absorption for the same film thickness. In addition, 45-nm-thick (1/4-wave) $HfO_2$ film was prepared by conventional e-beam deposition to investigate PHI signal variation with film thickness. To create insulation from defects introduced by the polishing process, UV-grade

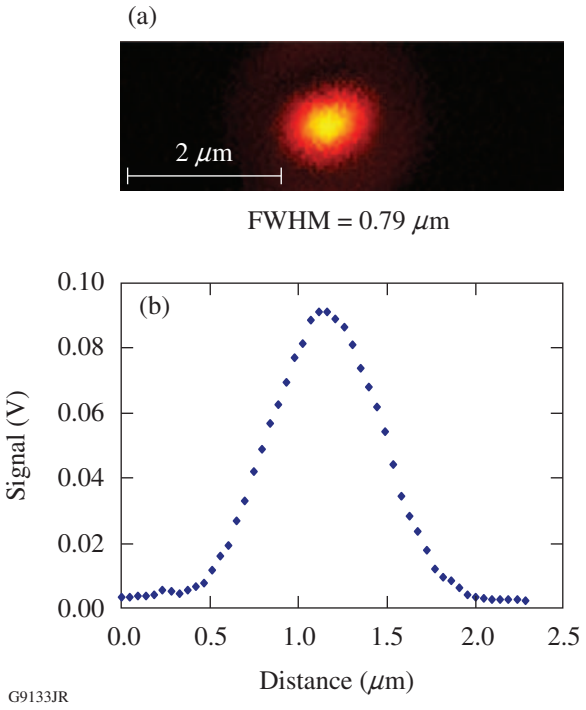


Figure 125.25
Characterization of the combined focal spot of 355-nm pump and 633-nm probe beams: (a) image of the focal spot obtained with a 1-$\mu$m pinhole; (b) cross-sectional profile.

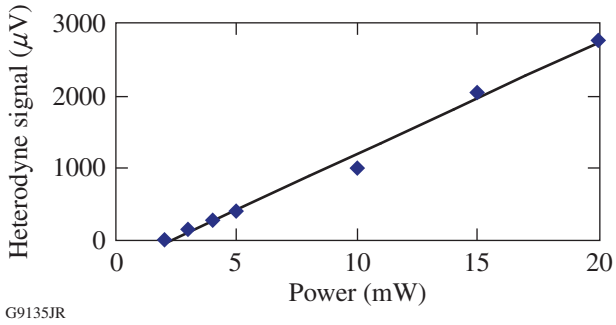


Figure 125.27
PHI signal from homogeneously absorbing $TiO_2$ thin-film sample as a function of 355-nm pump output power.

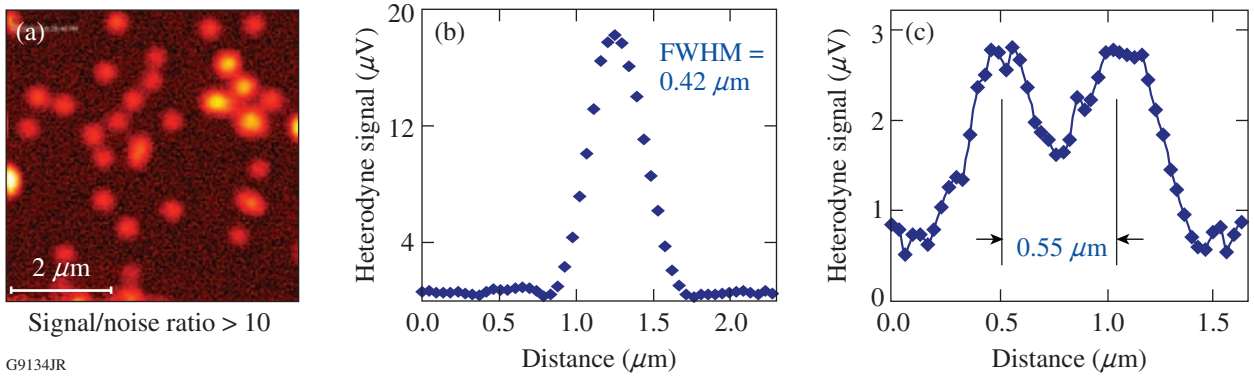


Figure 125.26
PHI calibration using embedded 14-nm gold nanoparticles: (a) 6 × 6-$\mu$m PHI image, (b) single-particle signal profile, and (c) signal profile for two particles separated by 0.55 $\mu$m.

fused-silica substrates were coated first by a 1-$\mu$m-thick $SiO_2$ layer [see Fig. 125.28(a)]. Next, in the same coating run, $HfO_2$ films of appropriate thickness were deposited. The E-field intensity distribution peaked at both interfaces and in the bulk of the 1-wave-thick film [Fig. 125.28(b)] and had only one peak at the $HfO_2/SiO_2$ interface in the case of 1/4-wave film [Fig. 125.28(c)]. This information is important for the analysis of the PHI signal versus film-thickness variation.

4. Damage Testing and Damage Morphology

The PHI mapping of $HfO_2$ monolayers was complemented by damage-threshold and morphology studies using 351-nm, 0.5-ns pulses from a Nd-doped glass laser. Damage thresholds (1-on-1 mode) were measured using 110× magnification, dark-field microscopy, and damage morphology was investigated by means of AFM. Note that the 355-nm wavelength of the pump laser for the PHI technique is very close to the 351-nm wavelength of the damage-test laser, which allows one to establish correlation between measured PHI signals and damage-threshold values.

## Results and Discussion

1. PHI Imaging of $HfO_2$ Films Prior to Irradiation

Photothermal images of $HfO_2$ monolayer films (see Fig. 125.29) showed different absorption levels for different film thicknesses and deposition techniques but did not show

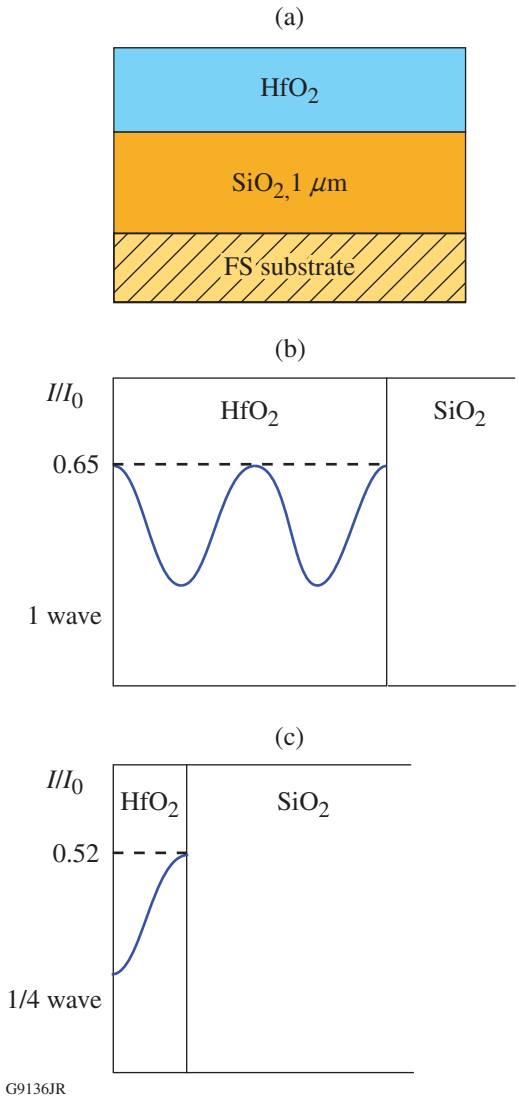


Figure 125.28
(a) Schematic of $HfO_2$ thin-film sample and E-field intensity distribution for (b) 1-wave-thick and (c) 1/4-wave-thick samples.

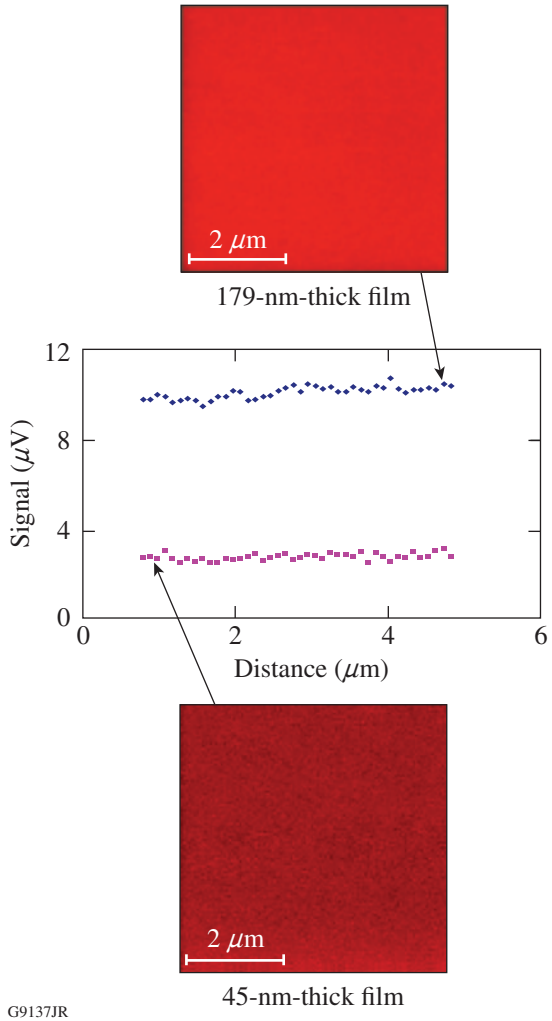


Figure 125.29
Heterodyne images and corresponding horizontal signal profiles of conventionally deposited 179-nm-thick and 45-nm-thick $HfO_2$ films prior to irradiation.

any structure attributable to the presence of isolated localized absorbers. This allows us to hypothesize that average distances between absorbing defects are much smaller than the laser beam's spot size and, moreover, than the ~0.4-$\mu$m spatial resolution of the system. Comparison of PHI signals for two different $HfO_2$ film thicknesses, 1 wave and 1/4 wave, gave a ratio very close to 4:1 (Fig. 125.29), which renders a PHI signal proportional to the film thickness and also to the absorbing volume. This important result indicates that despite the presence of the intensity peak [Figs. 125.28(b) and 125.28(c)], absorption at the $HfO_2/SiO_2$ interface is not a dominating factor. Otherwise, the ratio of signals should be close to 1.25, in agreement with the intensity ratio at the interface position.

As expected, a 1-wave-thick sample deposited by a plasma-assisted technique, non-optimized for a laser-damage performance, generated an almost 3× higher PHI signal compared to a standard e-beam–deposited sample. This result correlates well with single-shot damage thresholds measured for these samples (see Table 125.I) and, if confirmed by the larger statistics for different coating materials, can point to the PHI technique as a preliminary indicator of ns-pulse laser damage performance.

Table 125.I: Damage thresholds (351 nm) and corresponding PHI signals for 1-wave-thick $HfO_2$ films.

| $HfO_2$ films | Damage thresholds ($J/cm^2$) | Heterodyne signal ($\mu V$) |
|---|---|---|
| Standard e-beam | 3.57±0.23 | 9.8 |
| Plasma assisted | 2.03±0.13 | 27.6 |

## 2. PHI and AFM Mapping of $HfO_2$ Damage Morphology

PHI and AFM mapping of damaged sites revealed damage in the form of micrometer- and nanometer-scale craters. These craters appear as very dark (no signal) features on PHI images (Fig. 125.30). Taking into account that no signal was detected on silica samples without a hafnia layer, one can assume that the $HfO_2$ layer has been removed in the crater-formation process. Another observation is that scans performed in the central part of the damage site, and depicted in Fig. 125.30(c), show enhanced absorption in parts of the coating that survived laser irradiation. This indicates structural modification of $HfO_2$ film subjected to a fast heating and cooling cycle and allows one to forecast damage propagation under continuing pulse irradiation. PHI images of damage morphology also provided an opportunity to independently evaluate the method's spatial resolution, because of re-deposited nanoscale particles. A cross-sectional profile through one of these particulates, shown in Fig. 125.30(d), confirmed a true submicrometer resolution of 0.4 $\mu$m, in good agreement with the calibration value of 0.42 $\mu$m obtained using gold nanoparticles. AFM imaging (Fig. 125.31) revealed further details about the damage process. Both isolated craters [Fig. 125.31(a)] imaged on the periphery of the damage site and merging craters from the heavier-damaged central part of the same site [Fig. 125.31(b)] are missing the granular structure of the surrounding coating material. Such morphology indicates that a melting point has been reached by the material at the bottom of the crater ($SiO_2$, as revealed by AFM analysis), and the observed smooth, glassy structure is a result of material flow and resolidification. Moreover, crater boundaries and narrow "bridges" between

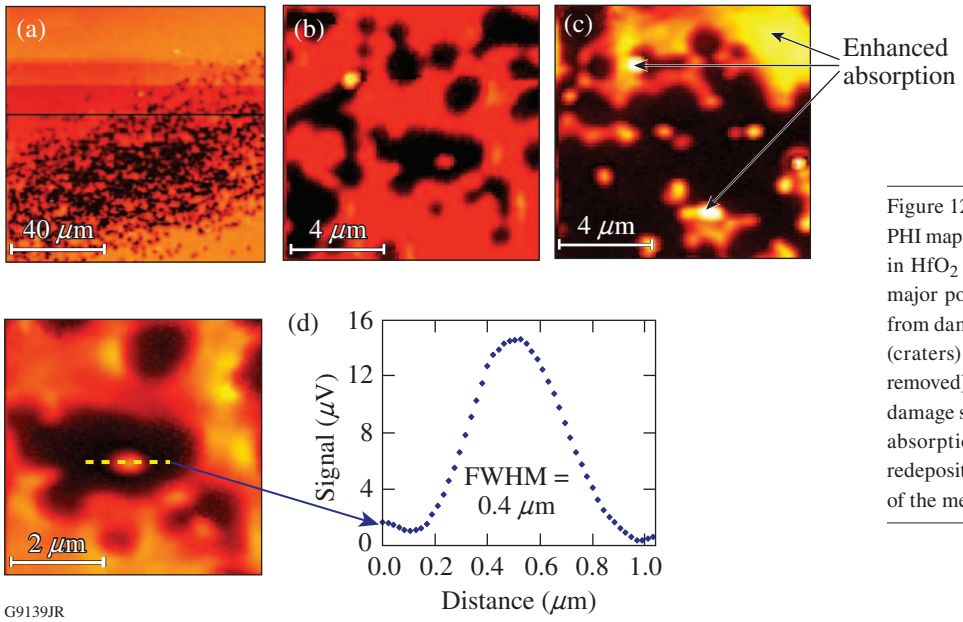


Figure 125.30
PHI mapping of 351-nm, 0.5-ns damage morphology in $HfO_2$ film samples: (a) 100-$\mu$m scan covering a major portion of the damage site; (b) 10-$\mu$m scan from damage site periphery [dark features are areas (craters) where hafnia film has been completely removed]; (c) 10-$\mu$m scan from the central part of the damage site; remaining hafnia film shows enhanced absorption; (d) cross-sectional profile through a redeposited particle, confirming 0.4-$\mu$m resolution of the method.

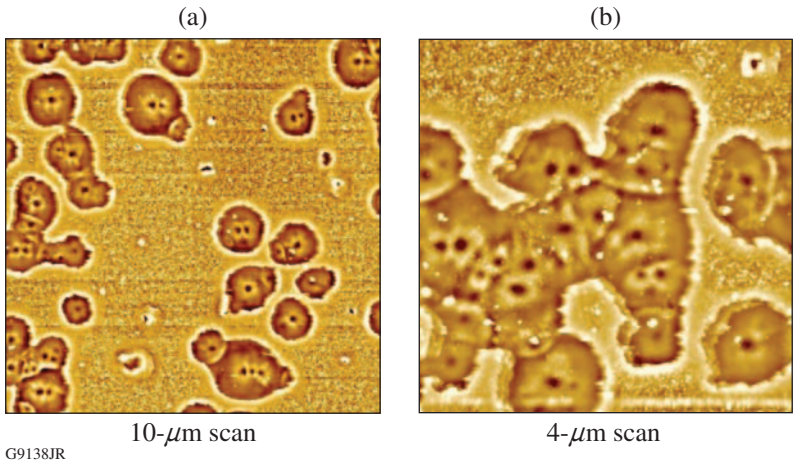


Figure 125.31
AFM images of damage morphology: (a) isolated craters formed on the damage-site periphery (10-$\mu$m scan); each crater has at least one damage origination point; (b) merging craters from the central part of the damage (4-$\mu$m scan); crater edges show smoothing of granular film structure, indicative of reaching the melting point.

craters [Fig. 125.31(b)] show $HfO_2$ film granularity that is much smoother than normal coating granularity, indicating the early stage of $HfO_2$ material melting. Small (100 nm or smaller) particles inside the area of heavier damage [presented in Fig. 125.31(b)] are attributed to material being redeposited onto the surface during crater formation. Another important observation here is that each crater [Fig. 125.31(a)] has in its central part at least one additional nanoscale protrusion—the point at which damage originates. Calculation of the average initiation-point separation using data from Fig. 125.31(b) gave a value of 272±59 nm. Previous studies using artificial nanoscale absorbers[7] demonstrated that damage initiation requires an effective energy transfer from absorber to the surrounding matrix; in porous thin-film material, only part of all absorbers can satisfy this condition. From this, we conclude that the actual distance between absorbing defects is smaller than the measured initiation-point separation. This conclusion is strongly supported by our previously derived estimate (see **PHI Imaging of $HfO_2$ Films Prior to Irradiation**, p. 28) that the separation would be much smaller than 0.4 $\mu$m. Consequently, we estimate the upper limit for the average absorber separation to be ~100 nm.

Cross-sectional profiles taken on AFM images (Fig. 125.32) through damage craters reveal further details of crater formation. An average crater depth of 186 nm appears to be very close to the 179-nm thickness of the $HfO_2$ layer, which strongly supports hafnia layer removal suggested by PHI mapping. A nanoscale protrusion located at the center of the main crater propagates 30 nm to 80 nm into the supporting $SiO_2$ layer, which also clearly points to localized absorption and material removal in the silica layer. Such observations suggest the following damage-process scenario: Energy from the laser pulse is initially absorbed at random locations within the $HfO_2$ layer, causing a local temperature rise. At selected locations, characterized by good thermal contact between the $HfO_2$ and $SiO_2$ layers, heat conduction through the $HfO_2/SiO_2$ interface may raise the temperature in the $SiO_2$ material up to the melting point and higher. Recently, it was convincingly demonstrated[8] that silica, upon reaching a temperature $T \approx 2200$ K (slightly above melting point), becomes absorbent enough at 355 nm to cause a dramatic drop in the nanosecond-pulse surface damage threshold. In our case, it means that once this temperature

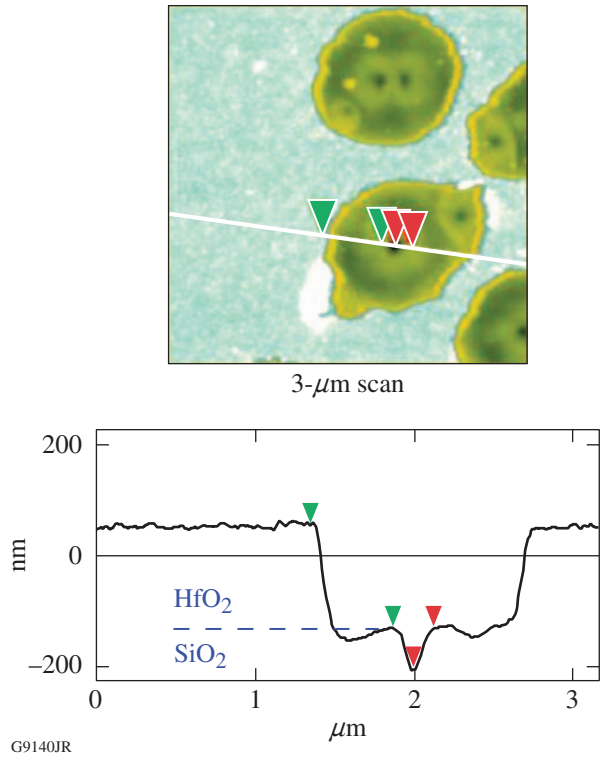


Figure 125.32
Damage crater cross-sectional profile (AFM). Crater-depth measurement points to removal of the hafnia layer within crater volume.

is reached inside the $SiO_2$ layer within the laser-pulse–length interval, local temperature and pressure can grow dramatically by acquiring energy from the laser pulse. As a result, explosive removal of the $HfO_2$ material within the main crater volume and $SiO_2$ material within the central nanocrater takes place. Taking into account that the hafnia melting point $T_m(HfO_2)$ = 3085 K is much higher than that of silica, $T_m(SiO_2)$ = 1986 K, $HfO_2$ material can be removed from the crater volume via a stress-driven mechanism, without full melting.[9] This conclusion is supported by crater morphology (see Fig. 125.32) characterized by sharp edges that are missing an elevated smooth rim, typical for melted material flow.

3. Nature of Nanoscale Absorbers

As suggested in the **Introduction**, p. 25, there are two possible nanoscale absorber candidates in metal-oxide thin film: metal clusters and high-density areas of electronic defects. Figure 125.33 shows the spectral dependence of the absorption cross section for a 10-nm Hf cluster.[10] Also on Fig. 125.33 are data for a 10-nm gold cluster calculated[10] at 355-nm wavelength, which is just slightly larger than for Hf. In **Experimental**, p. 25, we reported on PHI imaging of gold clusters as small as 5 nm, making it realistic to assume that we could detect similarly sized Hf clusters using PHI, if the same were present in the $HfO_2$ film. Assuming ~100-nm average separation between 5-nm clusters, lattice unit cell volumes[3] of $2.23 \times 10^{-2}$ nm$^3$ for Hf, and $3.48 \times 10^{-2}$ nm$^3$ for $HfO_2$, the portion of Hf in a form of clusters inside $HfO_2$—$3.1 \times 10^{-5}$—is rather high. Another observation that questions the possible role of metal clusters is that $HfO_2$ films deposited from oxide, as a starting material, should have a lower probability of metal-cluster formation than films deposited from Hf metal. Nevertheless, films produced by oxide evaporation show higher absorption and lower UV–ns-pulse damage thresholds.[11] Thermodynamic modeling of cluster formation in an evaporation plume and also during film growth is needed to evaluate the realistic cluster fraction inside metal oxide film.

Absorption by electronic defects, enhanced at grain boundaries within columnar film structure, is another possible source of damage initiation. Photoluminescence excited by 266-nm, 4.66-eV photons revealed a rich spectrum attributable to absorption from electronic defect states.[11] Figure 125.34 shows an energy diagram for oxygen-ion vacancy defect states ($V^+$ and $V^{2+}$) inside a $HfO_2$ bandgap,[3] where energy permits electron transition into the conduction band by absorption of 355-nm, 3.5-eV photons. Further heating of these electrons by a laser pulse ensures avalanche formation and damage. For obvious reasons, spatial density of the electronic defects must be much larger than cluster density in order to achieve a similar localized effect. That might explain the very small spatial signal variation on PHI images of $HfO_2$ films prior to irradiation as a result of averaging over a large number of absorbing defects. Further experiments and modeling are needed to clarify which type of absorbing defect plays a major role in the damage process.

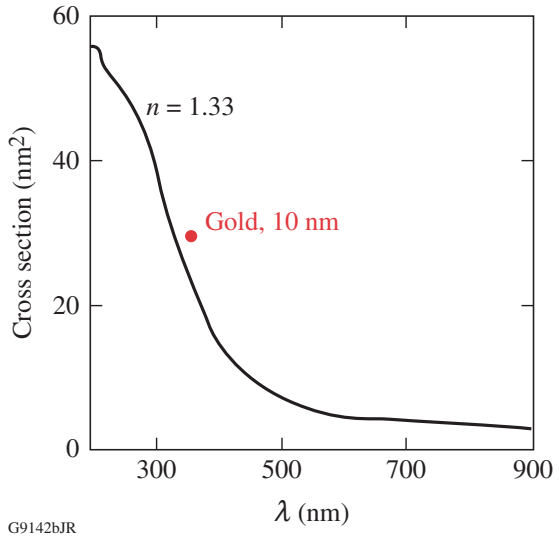


Figure 125.33
Absorption cross section for 10-nm-diam Hf cluster in a medium with refractive index = 1.33 as a function of wavelength. For comparison, 355-nm–wavelength data for a 10-nm Au cluster are also shown on the graph.

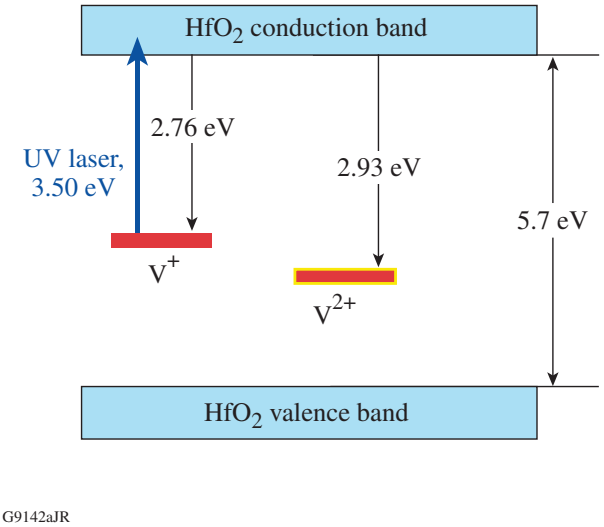


Figure 125.34
Energy-level diagram for defect states[3] in monoclinic $HfO_2$ whose electron affinities permit electron excitation into the conduction band through absorption of a 355-nm photon.

## Conclusions

Photothermal heterodyne imaging using near-UV light as a pump source can measure metal oxide's thin-film absorption properties with high sensitivity and submicron (~0.4-$\mu$m) spatial resolution.

PHI images of $HfO_2$ films prior to irradiation are structureless, pointing to absorber separations much smaller than the 0.4-$\mu$m resolution of this method. Combining these data with damage initiation statistics allowed us to estimate an upper limit for an average absorber separation at ~100 nm. By comparing heterodyne signals for different film thicknesses, we found that $HfO_2/SiO_2$ interfacial absorption is not a major factor, but the main contribution comes from absorption inside $HfO_2$ film.

Observed correlation between PHI signals and measured nanosecond-pulse damage thresholds for $HfO_2$ monolayer films points to PHI as a useful technique for predicting laser-damage resistance of differently deposited thin films.

Using AFM and PHI to analyze the damage morphology allowed us to suggest a $HfO_2$ damage mechanism. The process starts with localized absorption and a temperature rise in the $HfO_2$ film and is followed by heat transfer to the supporting $SiO_2$ layer by means of heat conduction. At locations with good thermal contact, the temperature in $SiO_2$ can rise above the melting point and reach a critical temperature ~2200 K at which silica transforms into an effectively absorbing material. As a result, energy acquisition from the laser pulse leads to a quick temperature and pressure rise, explosive material removal, and damage.

Hafnium clusters and high-density areas of electronic defects still remain hypothetical candidates as damage initiators. Further experiments and modeling are required for unambiguous damage-driving absorber identification.

## ACKNOWLEDGMENT

This work was supported by the U.S. Department of Energy Office of Inertial Confinement Fusion under Cooperative Agreement No. DE-FC52-08NA28302, the University of Rochester, and the New York State Energy Research and Development Authority. The support of DOE does not constitute an endorsement by DOE of the views expressed in this article.

## REFERENCES

1. S. Papernov and A. W. Schmid, J. Appl. Phys. **82**, 5422 (1997).
2. S. Papernov, A. W. Schmid, A. L. Rigatti, J. B. Oliver, and J. D. Howe, in *Laser-Induced Damage in Optical Materials: 2005*, edited by G. J. Exarhos *et al.* (SPIE, Bellingham, WA, 2005), Vol. 5991, pp. 429–435.
3. A. S. Foster *et al.*, Phys. Rev. B **65**, 174117 (2002).
4. S. Berciaud *et al.*, Phys. Rev. Lett. **93**, 257402 (2004).
5. S. Berciaud *et al.*, Phys. Rev. B **73**, 045424 (2006).
6. S. Papernov and A. W. Schmid, J. Appl. Phys. **104**, 063101 (2008).
7. S. Papernov and A. W. Schmid, J. Appl. Phys. **92**, 5720 (2002).
8. J. Bude *et al.*, in *Laser-Induced Damage in Optical Materials: 2007*, edited by G. J. Exarhos *et al.* (SPIE, Bellingham, WA, 2007), Vol. 6720, p. 672009.
9. S. I. Kudryashov, S. D. Allen, S. Papernov, and A. W. Schmid, Appl. Phys. B **82**, 523 (2006).
10. J. A. Creighton and D. G. Eadon, J. Chem. Soc. Faraday Trans. **87**, 3881 (1991).
11. A. Ciapponi *et al.*, J. Lumin. **1029**, 1786 (2009).

# Large Tunable, THz Electro-Optic Response in Cadmium Manganese Telluride (Cd,Mn)Te Single Crystals

Cadmium manganese telluride (Cd,Mn)Te (CMT) is a well-studied II–VI semiconductor because of its many desirable attributes and versatility. One such attribute is CMT's stable zinc-blend structure for Mn concentrations, $x$, up to 0.70, providing a very wide tuning range of the energy bandgap $E_g$. CMT also exhibits a large magneto-optic Faraday effect and is commonly used for isolators. Finally, it has a very high stopping power, showing great potential for x- and $\gamma$-ray detection.[1,2] In this article, we demonstrate CMT's exceptionally large electro-optic (EO) Pockels effect, which has previously been underestimated because of screening of the applied electric field by free carriers. Furthermore, we discuss how the EO sensitivity can be magnified for a particular operating probe wavelength using bandgap engineering.

Electro-optic sampling (EOS) measurements were performed using a modified configuration of that described by Zheng *et al.*,[3] in which the transmitted beam was collected. The subpicosecond pulses for all measurements were generated by a low-temperature–grown GaAs, freestanding photoconductive switch (PCS) integrated onto a coplanar strip (CS) transmission line.[4] Our CMT samples were as-grown, millimeter-size single crystals obtained using a modified vertical Bridgman method.[1] The crystals were oriented in such a manner that the electric field was applied along the [110] direction, and the sampling beam, incident along the [–110] direction, had parallel polarization with respect to the electric field. This configuration ensured maximum EO interaction.[5]

Since CMT is a semi-magnetic semiconductor, it was important to determine first whether the CMT optical response was a result of the EO Pockels effect or the magneto-optic Faraday effect. The PCS element was positioned at the center of the CS line, while the CMT transducer was placed on the transmission line, to one side of the PCS at first, and moved to the other side of the switch in a second measurement. This way the electric field of the signal generated by the PCS was constant on both ends of the CS line. However, the polarity of the magnetic field was flipped. The measurements showed no sign change of the signal, establishing that the dominant mechanism in sampling an ultrafast signal is the EO effect.

EO transducers are able to resolve THz pulses by converting the electric field into a retardation $\Gamma$ of the sampling beam's polarization. For $x$-cut $LiTaO_3$, $\Gamma$ is given by

$$\Gamma_{LTO} = \frac{2\pi(n_e - n_o)L_1}{\lambda} - \frac{\pi\left(n_e^3 r_{33} - n_o^3 r_{13}\right)L_2}{\lambda d} V_{LTO}, \qquad (1)$$

where the non-isotropic $LiTaO_3$ has two significant EO coefficients, $r_{33}$ and $r_{13}$, and an extraordinary and ordinary refractive index, $n_e$ and $n_o$, respectively. The gap between transmission lines is $d$, the crystal thickness is $L_1$, the interaction length between crystal and electric field is $L_2$, and $V_{LTO}$ is the voltage transient propagating beneath the $LiTaO_3$ crystal. It is important to note that this transient is affected by the dielectric of the measuring transducer. The first term of the $\Gamma_{LTO}$ equation is the intrinsic birefringence independent of the electric field and can be negated by a second perpendicular crystal of equal $L_1$. The second term is the Pockels-induced birefringence.

Isotopic $\bar{4}3m$ crystals have no intrinsic birefringence, so $\Gamma$ of the CMT transducer is[6]

$$\Gamma_{CMT} = \frac{2\pi\left(n_o^3 r_{41}\right)L_2}{\lambda d} V_{CMT}, \qquad (2)$$

where $V_{CMT}$ is the CMT counterpart to $V_{LTO}$ and the only nonzero components of the EO tensor are $r_{41} = r_{52} = r_{63}$. Literature[6] for CdTe gives $r_{41} = 4.5$ pm/V, which is based on measurements taken at $\lambda = 1$ $\mu$m and for frequencies lower than 20 kHz. Assuming that the refractive indices and EO coefficients for $LiTaO_3$ (Ref. 7) are constant in the 633- to 800-nm wavelength range, calculations show that $\Gamma_{CMT}$ is less than $\Gamma_{LTO}$. This is, however, in direct contradiction to our experimental results shown in Fig. 125.35, where we present the

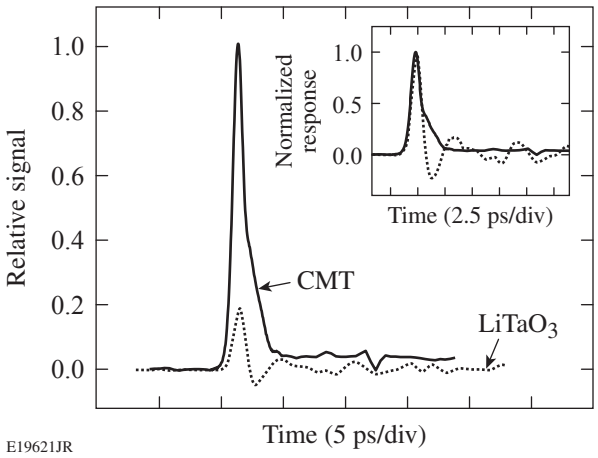


Figure 125.35
EOS response of a 1.45-V pulse detected by $Cd_{0.88}Mn_{0.12}Te$ (solid) and $LiTaO_3$ (dotted) transducers at a sampling beam wavelength of 800 nm. The inset compares the normalized responses of CMT (solid) and $LiTaO_3$ (dotted).

EO sampling responses of a $Cd_{0.88}Mn_{0.12}Te$ transducer (solid) and the widely used EO crystal $LiTaO_3$ (dotted). We see that CMT exhibits retardation five times greater than that of $LiTaO_3$.

The differential transfer function for the EO modulator in our setup is

$$\frac{\Delta V}{V_0} = \frac{1}{2}\sin\left(\pi V / V_\pi\right) \approx \frac{\pi V}{2V_\pi}, \quad \text{for } V \ll V_\pi , \tag{3}$$

where $V_\pi$ is the $V_{LTO}$ required to retard the optical probe by $\pi$ and the dc component ($V_0$) is 31.5 mV/$\mu$W times the measured power of the transmitted probe. It is not possible, however, to determine the magnitude of $r_{41}$ directly from the CMT EOS response because of the unknown variables $L_2$ and $V_{CMT}$. Therefore, we first determined the coupling between the transducer and transmission line using $LiTaO_3$. Coupling measurements were easily accomplished by directly applying a 2-V peak-to-peak, low-frequency (MHz) sinusoid, bypassing the PCS entirely. Knowing the EO coefficients for $LiTaO_3$ (Ref. 6), $V_{LTO}$ and $L_2$ were calculated from the EOS response and coupling measurements using Eqs. (1) and (3).

The $L_2$ was small (1.18±0.26 $\mu$m), which we assume was a result of the poor condition of the substrate. This was confirmed by calculating a large air gap of 24 $\mu$m between the transmission line and crystal. These calculations were determined by the impedance for our CS line in a multilayer substrate[8] ($LiTaO_3$/air-gap/MgO) using the effective dielectric $\varepsilon_{eff} = (c/v)^2 = 9.2$. The velocity $v$ was evaluated using the temporal delay of the EOS response measured for two spots with a known spatial separation. The $\varepsilon_{eff}$ also established the reflection of the pulse at the crystal interface along the transmission line. The impedance mismatch in $LiTaO_3$ resulted in a 14% reflection of the generated pulse at the crystal interface, and the original signal of the PCS was then obtained (~1.45 V). Finally, the same air gap for CMT resulted in a smaller (3.5%) reflection, showing that $V_{CMT}$ was $1.12 \times V_{LTO}$.

We strongly believe that the discrepancy between our ultrafast CMT retardation value and the low-frequency one given in the literature is caused by free carriers present in as-grown CMT crystals. These crystals are naturally *p*-type and holes are capable of screening slow oscillations of applied voltage, preventing any significant EO coupling at low frequencies. The free-carrier screening frequency can be estimated by dividing our CMT sample conductivity $\sigma \approx 10^{-3}$ S/cm (Ref. 1) by its permittivity, resulting in a value as high as 1.25 GHz. Measuring the EO response at 256 kHz, we calculated that the suppressed $r_{41}$ for $Cd_{0.88}Mn_{0.12}Te$ was as low as 2.7±0.8 pm/V. This result was in close approximation to CdTe [4.5 pm/V (Ref. 6)] and $Cd_{0.75}Mn_{0.25}Te$ [3.5 pm/V (Ref. 8)] coefficients found in literature.

The fact that our CMT transducer was able to render the ultrafast PCS signal precisely (Fig. 125.35) with the response 5× greater ($\Delta V$ = 504 $\mu$V) than that of $LiTaO_3$ ($\Delta V$ = 95 $\mu$V) is because the pulse generated by the switch contains frequency components far exceeding the carrier screening process.

Table 125.II provides the *r* coefficients and the $V_\pi$ values for several CMT crystals, taking into account the previously calculated coupling factors and the wavelength-dependent $n_0$, as well as the other EO transducers found in the literature. Comparative measurements in Table 125.II for $Cd_{0.82}Mn_{0.12}Te$ and $Cd_{0.91}Mn_{0.09}Te$ show that the kHz- and MHz-range measurements undervalue the EO coefficient by nearly an order of magnitude because of screening effects. Furthermore, our independent EO coupling measurements performed on $Cd_{0.91}Mn_{0.09}Te$ at 256 kHz but at 10 K, demonstrated that the EO response was 10× greater than that at 300 K. In the latter case, free carriers were immobilized by deep-level traps as the temperature was lowered.

EOS measurements for various wavelengths were performed using a $Cd_{0.91}Mn_{0.09}Te$ crystal (Fig. 125.36), showing a dramatic increase of the EO response when approaching $E_g$. Knowing that the signal is electro-optic in nature, we attributed

Table 125.II: Measurements (bold) and previously reported values of the optimum EO coefficients and $V_\pi$ for several (Cd,Mn)Te crystals of $x$ and for other popular EO transducers. Provided are the probe wavelength, tested signal frequency, and the probe wavelength appropriate $n$ for the crystal.

| Crystal | $\lambda$ (nm) | $f$ | $n$ | $r$ (pm/V) | $V_\pi \cdot d/L_2$ (V) |
|---|---|---|---|---|---|
| **CdTe** | **855** | **THz** | $\mathbf{n_o = 2.91}$ | $\mathbf{r_{41} = 30.2 \pm 2.9}$ | **572** |
| CdTe (Ref. 6) | 1000 | kHz | $n_o = 2.84$ | $r_{41} = 4.5$ | 3880 |
| $\mathbf{Cd_{0.91}Mn_{0.09}Te}$ | **855** | **THz** | $\mathbf{n_o = 2.76}$ | $\mathbf{r_{41} = 24.7 \pm 1.2}$ | **821** |
| $\mathbf{Cd_{0.88}Mn_{0.12}Te}$ | **800** | **THz** | $\mathbf{n_o = 2.79}$ | $\mathbf{r_{41} = 28.3 \pm 5.9}$ | **651** |
| $\mathbf{Cd_{0.88}Mn_{0.12}Te}$ | **800** | **kHz** | $\mathbf{n_o = 2.79}$ | $\mathbf{r_{41} = 2.7 \pm 0.8}$ | **6825** |
| $Cd_{0.75}Mn_{0.25}Te$ (Ref. 8) | 800 | GHz | $n_o = 2.64$ | $r_{41} = 3.5 \pm 0.5$ | 4735 |
| $\mathbf{Cd_{0.50}Mn_{0.50}Te}$ | **855** | **THz** | $\mathbf{n_o = 2.52}$ | $\mathbf{r_{41} = 25.3 \pm 1.2}$ | **1059** |
| $LiTaO_3$ (Ref. 6) | 800 | THz | $n_{e/o} = 2.18/2.176$ | $r_{33/13} = 33/7.5$ | 3490 |
| ZnTe (Ref. 12) | 800 | THz | $n_o = 3.24$ | $r_{41} = 4.04$ | 2911 |
| DAST (Ref. 3) | 810 | THz | $n_{a/b} = 2.46/1.68$ | $r_{11/21} = 77/42$ | 790 |

this phenomenon to the wavelength dependence of $n_o$ (Ref. 9). Our experimental EOS dependence on wavelength was fit (solid line in Fig. 125.36) using the $n(\lambda)$ dispersion model given by Schubert *et al.*[10] Taking the asymptote as the crystal bandgap, the $E_g$ (1.623 eV) was slightly smaller than the calculated value [1.646 eV (Ref. 11)], apparently, because of interstitial states broadening the bandgap. The EO dependence on $\lambda$ can be easily exploited by either tuning the operating probe $\lambda$ to near-$E_g$, as we have presented in Fig. 125.36. Alternatively, for tests using a fixed probe wavelength above 600 nm, crystals can be custom grown to match for greatest signal quality. We finally note that Table 125.II shows that for an 855-nm probe, CdTe has twice the sensitivity as $Cd_{0.50}Mn_{0.50}Te$, but the CdTe bandgap limits its practical use to $\lambda > 812$ nm.

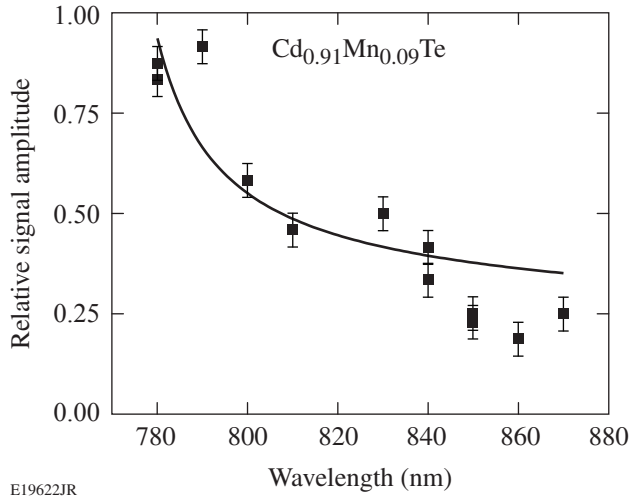


Figure 125.36
Wavelength dependence of $Cd_{0.91}Mn_{0.09}Te$ EO effect. Fittings are based on $n(\lambda)$ dispersion (solid line).

The calibration method used here allowed us to obtain absolute values of the EO coefficient for tested CMT crystals. We have demonstrated that, ultimately, CMT is significantly more sensitive at THz frequencies than previously expected[12] and more sensitive than the widely used indirect EO crystal $LiTaO_3$; the typical free-space THz EO transducer ZnTe;[12] and even when compared to DAST, an organic crystal exhibiting the largest EO coefficient of any material.[3,13] Furthermore, CMT exhibits a low $\varepsilon_r$, so only a small percentage of the signal is lost because of reflections along the transmission line. The CMT EOS response shown in Fig. 125.35 also presents a much cleaner signal as compared to the $LiTaO_3$ response because of the absence of a significant dielectric loading. Carrier screening was verified as the source of an order-of-magnitude difference between the CMT EO effect response at very high (THz) and low (MHz) frequencies. Finally, the CMT EO wavelength dependence was exploited to garner the highest sensitivity.

## ACKNOWLEDGMENT

The authors thank Drs. W. R. Donaldson and H. Irie for their many valuable discussions. A. S. C. acknowledges support from the Frank Horton Graduate Fellowship Program at the University of Rochester Laboratory for Laser Energetics. Work in Rochester was supported in part by NSF grant No. ECCS-0901701 and the U.S. Department of Energy Office of Inertial Confinement Fusion under Cooperative Agreement No. DE-FC 52-08NA28302, the University of Rochester, and the New York State Energy Research and

Development Authority. The support of DOE does not constitute an endorsement by DOE of the views expressed in this article. Work in Warsaw was supported by the Polish Ministry of Science and Higher Education through grant 3 T08A 046 30.

## REFERENCES

1. A. Mycielski *et al*., Phys. Stat. Sol. (C) **2**, 1578 (2005).
2. A. S. Cross, J. P. Knauer, A. Mycielski, D. Kochanowska, M. Wiktowska-Baran, R. Jakieła, J. Domagała, Y. Cui, R. B. James, and R. Sobolewski, Nucl. Instrum. Methods Phys. Res. A **624**, 649 (2010).
3. X. Zheng, S. Wu, R. Sobolewski, R. Adam, M. Mikulics, P. Kordoš, and M. Siegel, Appl. Phys. Lett. **82**, 2383 (2003).
4. R. Adam, M. Mikulics, A. Förster, J. Schelten, M. Siegel, P. Kordoš, X. Zheng, S. Wu, and R. Sobolewski, Appl. Phys. Lett. **81**, 3485 (2002).
5. S. Namba, J. Opt. Soc. Am. **51**, 76 (1961).
6. A. Yariv, *Optical Electronics in Modern Communications*, 5th ed., The Oxford Series in Electrical and Computer Engineering (Oxford University Press, New York, 1997).
7. Q. Wu and X.-C. Zhang, Appl. Phys. Lett. **68**, 1604 (1996).
8. E. Chen and S. Y. Chou, IEEE Trans. Microw. Theory Tech. **45**, 939 (1997).
9. A. S. Cross, D. Wang, G. Guarino, S. Wu, A. Mycielski, and R. Sobolewski, J. Phys., Conf. Ser. **92**, 012015 (2007).
10. D. W. Schubert *et al*., Appl. Phys. Lett. **60**, 2192 (1992).
11. J. K. Furdyna, J. Appl. Phys. **64**, R29 (1988).
12. B. Pradarutti *et al*., Opt. Commun. **281**, 5031 (2008).
13. F. Pan *et al*., Appl. Phys. Lett. **69**, 13 (1996).

# Improvements to Long-Pulse–System Performance and Operational Efficiency on OMEGA EP

## Introduction

An important operational goal of the Omega EP Laser Facility is to provide principal investigators with maximum UV energy on target, while maintaining UV peak fluences within an acceptable margin for safe operation. To optimize the long-pulse, on-target energy of OMEGA EP, we have pursued a threefold effort: (1) improve the laser-induced damage threshold of beam-transport optics; (2) improve the near-field beam profile; and (3) develop simulation tools to use during shot operations that provide rapid prediction of laser-system performance. These simulation tools predict the UV near-field beam-fluence distribution and on-target energy based on measurements of the inputs to the main amplifiers and are regularly used during shot operations. They have streamlined daily system qualification, making it possible for UV energy to be maximized within current system constraints.

Each of the four OMEGA EP beamlines uses a folded architecture and type-I/type-II frequency-conversion crystal (FCC) design based at the National Ignition Facility (NIF), as shown in Figs. 125.37(a) and 125.37(b).[1] Beamlines 1 and 2 can be operated in either short-pulse or long-pulse mode, while Beamlines 3 and 4 are dedicated to long-pulse operation. All beams are amplified in two passes through a 7-disk booster amplifier and four passes through an 11-disk main amplifier. Depending on the required shot conditions, the main amplifier operates with a variable number of pumped disks. Each beamline has an independent front-end laser source that provides a seed pulse that is injected into the transport spatial filter. The seed originates in a single-frequency fiber laser and is amplified in a regenerative amplifier (regen) after temporal shaping to a level of ~5 mJ. Further preamplification is provided by Nd:glass amplifiers prior to injection into the beamline. Spatial beam shaping is accomplished by two different apodizing elements located in the laser sources' front end. The first apodizer is located immediately after the regen and shapes the edges of the beam from round to square. The second apodizer is located just prior to the glass amplification stage and provides precompensation for the roll-off in gain that occurs at the edges of the beamline disk amplifiers.[2] The spatial gain variation of the front-end glass amplifiers is compensated by appropriately sizing the regen Gaussian output beam on the first apodizer.

Table 125.III shows the OMEGA EP individual beamline long-pulse–design energies, its current performance, and the total number of long-pulse target shots to date.

On-target $3\omega$ energies have been limited by the laser-damage resistance of the installed $3\omega$ transmissive optics.[3] Effort is underway to achieve OMEGA EP's long-pulse–design capability by procuring $3\omega$ optics with greater laser-damage resistance. The current $3\omega$ transport optics have been preconditioned to mitigate $3\omega$ laser-induced damage growth to a fluence of 4 J/cm$^2$ (3-ns Gaussian pulse),[4] and it is anticipated that new processing methods[5] applied to newly procured $3\omega$ optics may provide up to a factor-of-2 increase in damage threshold.[6]

Owing to the current fluence limitation, OMEGA EP must operate in a regime where both the beamline amplifiers and the frequency-conversion crystals are not highly saturated, making the $3\omega$ near-field beam structure very sensitive to small changes in the injected beam quality. Several methods to improve the near-field beam profile have been pursued and are described in the next section.

The sensitivity to laser front-end performance necessitates significant effort and care to avoid exceeding the established fluence limit. To maintain a high level of operational efficiency, simulation tools have been developed that predict the $3\omega$ near-field beam-fluence distribution and on-target energy using the preamplified injected near-field beam that is measured during pre-shot qualification. During shot operations, these tools have

Table 125.III: OMEGA EP long-pulse beamline performance.

| Design | Current | Total long-pulse shots through FY10 |
|---|---|---|
| 2.5 kJ ($t$ = 1 ns)<br>6.5 kJ ($t$ = 10 ns) | 1.0 kJ ($t$ = 1 ns)<br>3.0 kJ ($t$ = 10 ns) | 278 |

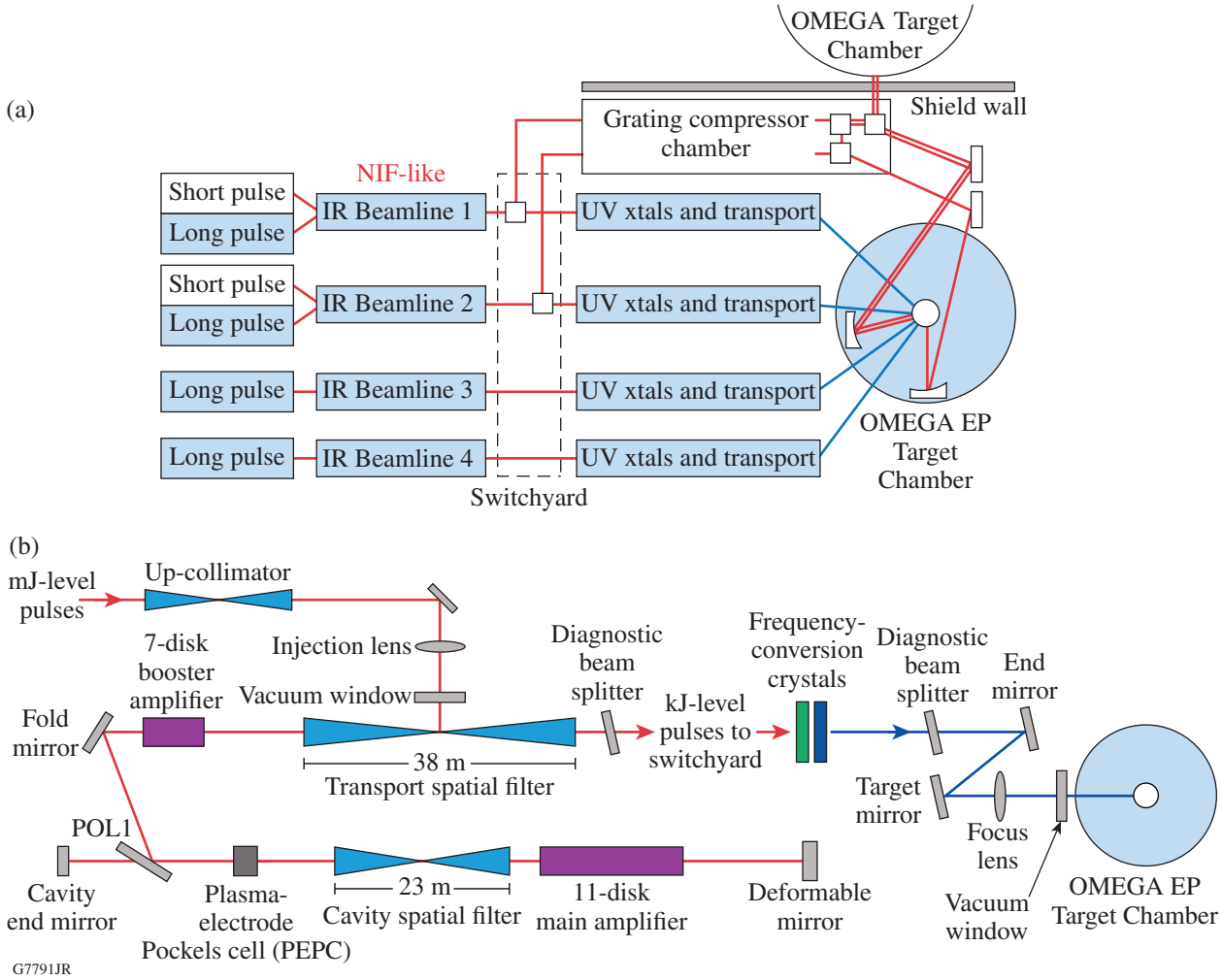


Figure 125.37
OMEGA EP Laser System configuration. (a) Beamlines 1 and 2 can be operated in either short-pulse or long-pulse mode, while Beamlines 3 and 4 are dedicated to long-pulse operation. (b) Each of the four beamlines uses a folded architecture and type-I/type-II frequency-conversion crystal design based on the NIF.

helped determine whether a user's energy requirements will be met without exceeding the $3\omega$ damage threshold using the current injected beam profile, or whether more time should be given to alignment and qualification activities. The rapid prediction capability that these tools provide has helped to ensure safe fluence levels while maintaining high operational efficiency. These simulation tools are described in **Simulation Tools for Operations**, p. 41.

## Near-Field Beam Improvements

Improved beam-shaping methods in both stages of apodization in the long-pulse front end have enhanced the efficiency of shot operations by providing consistently better beam profiles, therefore reducing the time required for pre-shot qualification. The following subsections describe (1) new apodizers that have been installed into both apodizing stages of Beamlines 3 and 4;[(a)] (2) a proof-of-concept experiment to smooth the $3\omega$ near-field beam by detuning the FCC's; and (3) a programmable spatial light modulator (PSLIM), which will be installed into the front end of Beamlines 3 and 4 during FY11.

### 1. First-Stage Apodizer

Since there is only a small amount of saturation in the beamline, small changes in the regen output beam's profile can produce large changes in the $3\omega$ beam. In practice, using the shape of the laser sources' regen output beam to precompensate for the approximately parabolic radial gain profile of the Nd:glass amplifiers has resulted in significant variations

[(a)]These upgrades will be implemented in the long-pulse front end of Beamlines 1 and 2 during FY11.

in 3$\omega$ beam quality. The day-to-day variations in regen beam quality and pointing make it necessary to adjust the centering of the regen beam profile into both the first-stage apodizer and the gain profile of the rod amplifier on shot day to optimize the 3$\omega$ beam profile, resulting in costly alignment delays. A new approach has been implemented that has significantly reduced the time required to optimize alignment. The regen output beam has been expanded at the location of the first apodizer to an approximately flat intensity distribution, and a new apodizer has been installed that shapes the beam from round to square and provides precompensation of the measured preamplifier radial gain using a binary mask.[7] The specified transmission profile combines a fourth-order polynomial fit to the measured small-signal radial gain with a square 40th-order super-Gaussian function. This has proven to be a much more robust design, providing better beam quality, greater ease of alignment, and greater reliability. Figure 125.38 shows that the measured transmission of the new apodizer matches the specified transmission within ~1%.

2. Second-Stage Apodizer

The first realization of the apodizer designed to precompensate beamline disk gain roll-off was a one-dimensional design [see Fig. 125.39(d)]. Following small-signal–gain measurements in Beamlines 3 and 4, an improved beam shaper that takes into account the beamline disk gain variations in two dimensions was designed and installed. The specified and measured transmission profiles for the new apodizer are shown in Figs. 125.39(a)–125.39(c). Figure 125.40 shows that a more uniform beam has been achieved after replacement of both front-end apodizers. The contrast of the beam, defined as the standard deviation of the fluence normalized to the average, was reduced from 16.8% to 12.6% with the installation of the new apodizers. The contrast was calculated over the 31-cm-square region shown overlaid on the beams in Fig. 125.40. The greater uniformity achieved within the overlaid region in Fig. 125.40(b) is attributed primarily to the first-stage apodizer, whereas the qualitative improvement in fill factor seen near the corners of the beam is attributed primarily to the second-stage apodizer.

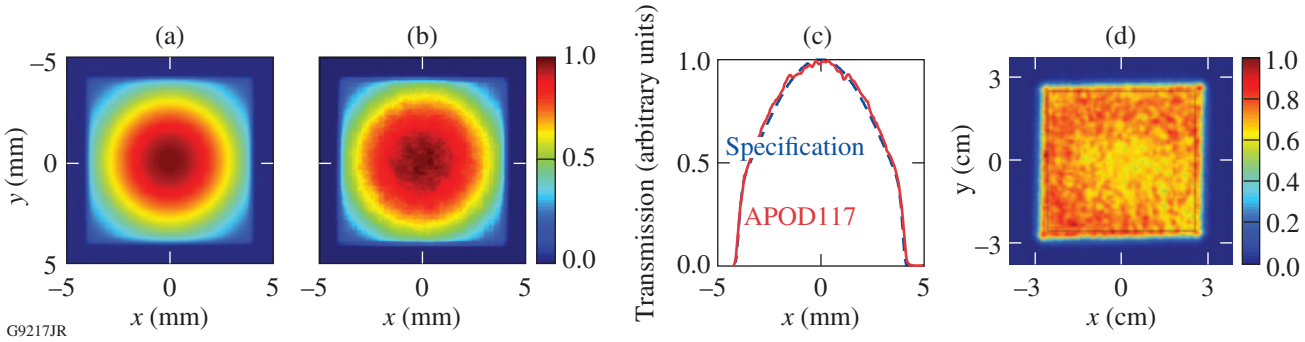


Figure 125.38
(a) Specified and (b) measured transmission of the new first-stage apodizer designed to precompensate the radial gain of the front-end Nd:glass amplifiers. Transmission lineouts are shown in (c) and the measured front-end output beam in (d).

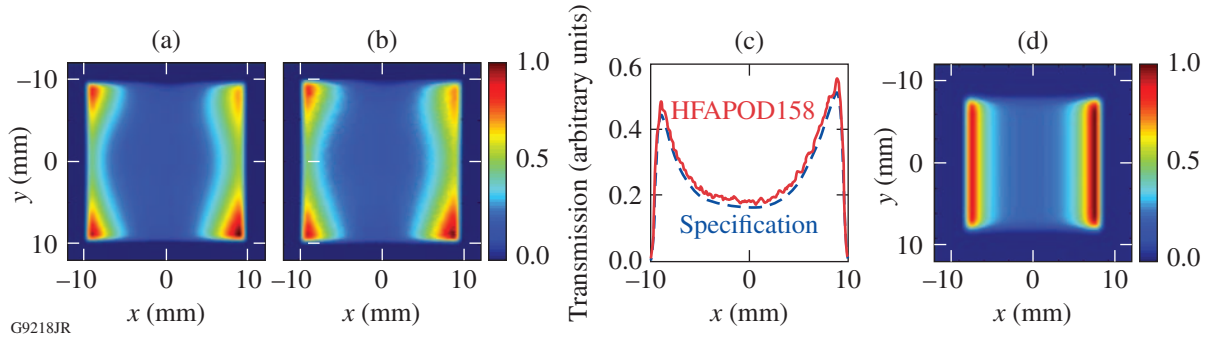


Figure 125.39
(a) Specified and (b) measured transmission of the new second-stage apodizer that precompensates the OMEGA EP beamline gain variation in two dimensions. Transmission lineouts are shown in (c). The previous one-dimensional apodizer design transmission is shown in (d).

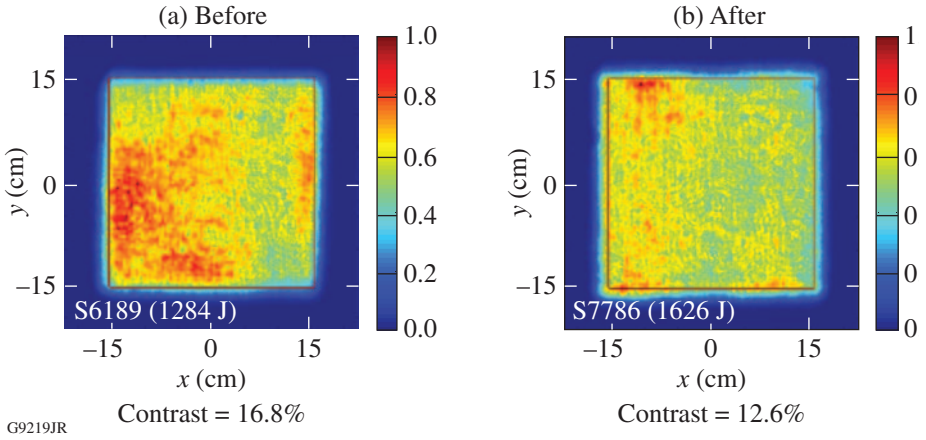


Figure 125.40
Normalized fluence of Beamline 4's 1$\omega$ output beams (a) before and (b) after installation of the new front-end apodizers. The contrast of the beam, defined as the standard deviation of the fluence normalized to the average and computed within the 31-cm × 31-cm area outlined in the figure, was reduced from 16.8% to 12.6% with the installation of the new apodizers.

3. UV Near-Field Beam Smoothing by FCC Detuning

Currently, the FCC's are angularly tuned to maximize the efficiency of the conversion process. When operated in this manner, the laser-damage thresholds of the current 3$\omega$ optics require that the 1$\omega$ laser intensity be maintained at a relatively low level (≤1 GW/cm$^2$). In this regime, small 1$\omega$ intensity variations produce large 3$\omega$ intensity variations, as shown in Fig. 125.41(a), causing the 3$\omega$ beam to be highly modulated. It has been proposed[8] that angularly detuning the FCC can reduce 3$\omega$ beam intensity modulations. Initial experiments on OMEGA EP have shown that by detuning the doubler crystal, the 3$\omega$ beam intensity modulation can be significantly reduced. The loss of conversion efficiency incurred by detuning the doubler is offset by increasing the 1$\omega$ energy into the FCC in order to maintain constant 3$\omega$ output energy [see Fig. 125.41(b)]. Measurements in Beamline 4 have shown a 13% reduction in peak 3$\omega$ fluence for the detuned FCC at nearly equivalent 3$\omega$ energy as the tuned FCC. Standard deviations of the 3$\omega$ beam fluence distributions were 21.2% and 14.7% for the tuned and detuned cases, respectively, indicating a significantly smoother beam for the detuned FCC, as shown in Fig. 125.42. This reduction in 3$\omega$ beam modulation should make it possible to deliver more energy to a target while maintaining peak 3$\omega$ intensities below the damage-threshold limit. To ensure that damage thresholds were not exceeded, this proof-of-concept experiment was performed at approximately half of the current 3$\omega$ energy limit for the 2-ns-square pulse shape used. The amount of increase in on-target energy that can be achieved will depend upon the reduction in peak fluence observed at energies approaching the 3$\omega$ damage threshold, which, in turn, will depend upon the level of saturation observed in the beamline. The utility of this beam-smoothing method on OMEGA EP will be explored in greater detail during FY11.

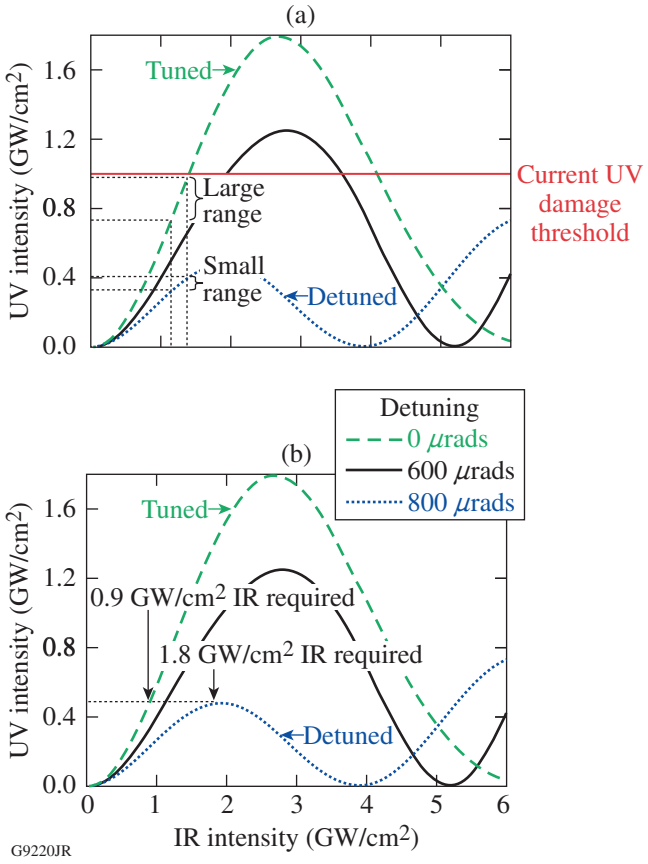


Figure 125.41
Simulated 3$\omega$ output versus 1$\omega$ input for the 11-mm–doubler, 9-mm–tripler OMEGA EP FCC design showing that (a) within the current operating regime of OMEGA EP, a detuned doubler can produce a smaller range of UV intensities for the same range of IR intensities than a tuned doubler; and (b) a detuned doubler requires more IR intensity to achieve the same UV intensity (or UV energy) as a tuned doubler.

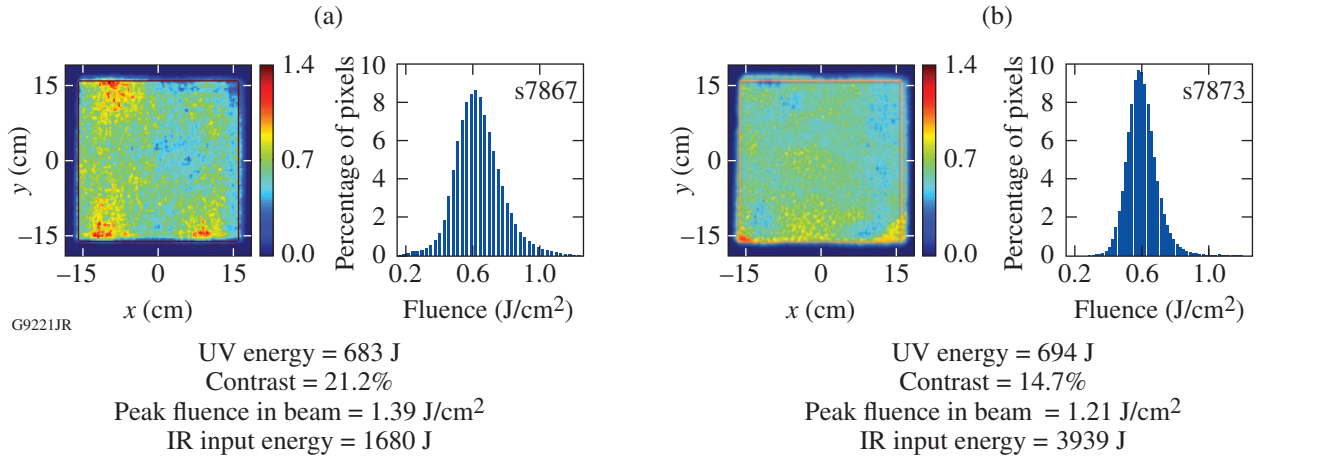


Figure 125.42
$3\omega$ near-field beams with (a) tuned and (b) detuned doubler measured on OMEGA EP Beamline 4 showing a significantly smoother beam for the detuned case.

4. Programmable Spatial Light Modulator (PSLIM)

A programmable spatial light modulator (PSLIM) will be installed into the front end of Beamlines 3 and 4 during FY11 to provide closed-loop correction of near-field beam amplitude. The PSLIM system shapes the laser beam's amplitude by using a liquid-crystal-on-silicon spatial light modulator that is based on an amplitude modulation carrier method.[9] It will be used primarily to improve the fill factor of the beam by the dynamic tuning of gain precompensation and to reduce near-field modulation by smoothing beam hot spots and edges.[10] Preliminary results for smoothing the beam at the location of the first apodizer in Beamline 3 are shown in Fig. 125.43.

**Simulation Tools for Operations**

The primary goal in the development of an operations simulation capability for OMEGA EP was to ensure UV system safety by predicting the $3\omega$ peak fluence of an OMEGA EP beamline with high spatial resolution (1 k × 1 k) in a time frame of 10 min or less using measured data from the daily injection qualification shot. A rapid prediction capability ensures that system operators will be prepared to shoot again within a qualification shot cycle if additional alignment corrections are required. Because of the combined time-critical and high-spatial-resolution requirements, a simplified model was chosen and its performance was characterized against actual measurements. The IR portion of the model incorporates the previously measured, spatially dependent small-signal gain of the beamline disk amplifiers, with gain saturation accounted for using the Frantz–Nodvik equations.[11] A one-dimensional version of the model is also available for high-resolution, temporal pulse–shaping simulations. Physical processes that are not included are free-space propagation, wavefront aberrations, and high-frequency spatial noise. As will be shown, by characterizing the model against measurements of current system performance, the model can be used as an efficient tool to determine the maximum-allowable $3\omega$ energy during

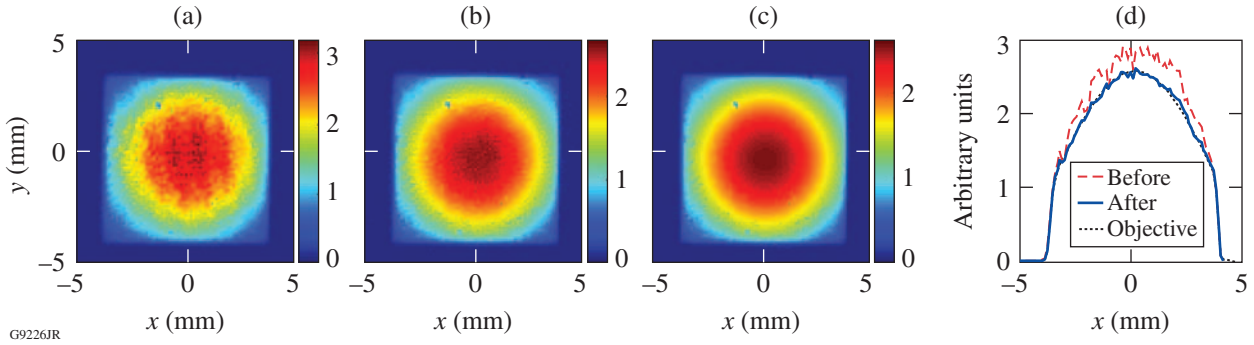


Figure 125.43
Initial results for fine-tuning the shape of the radial gain-precompensated beam using a programmable spatial light modulator (PSLIM) in the front end of Beamline 3: (a) before correction, (b) after correction. The objective map for the device is shown in (c) and lineouts in (d).

shot operations. Convergence of the model to the measured IR beamline energy is achieved by adjusting the per-disk loss to account for current system performance. The $3\omega$ beam and pulse are simulated using spline interpolation of data that have been generated from prior frequency-conversion simulations. A pc-based, MATLAB framework was used to provide a seamless interface to pre-shot alignment and analysis tools and to provide an intuitive environment for rapid development, testing, and deployment. A multiple-core, distributed computing capability can optionally be used. Model output predictions include $1\omega$ and $3\omega$ beamline output energies, near-field beam-fluence distributions, and pulse shapes. The model also has backward prediction capability, which is used to perform shot setup based on the requested $3\omega$ energy and pulse shape, and to calculate the maximum-allowable $3\omega$ energy and associated injection energy on a shot day.

Figure 125.44 compares simulated and measured square pulses for the $1\omega$ beamline output using the one-dimensional model. The agreement between the pulse shapes for $N$ points in time is characterized by their root-mean-square (rms) difference:

$$\text{rms difference} = \sqrt{\frac{1}{N}\sum_{i=1}^{N}\left[\text{sim}(i) - \text{meas}(i)\right]^2}\,, \qquad (1)$$

which is equal to 4% for the pulses shown in Fig. 125.44(a). The simulations used the regen output pulse from an injection shot taken on the same day [see Fig. 125.44(b)]; therefore, the rms difference represents the model's predictive capability and the regen shot-to-shot pulse stability. The inset in Fig. 125.44(a) lists the simulated and measured beamline output energies, 3589 J and 3540 J, respectively. Figure 125.45 compares simulated and measured ramped pulse shapes for both the $1\omega$ and $3\omega$ beamline outputs. The rms difference in Fig. 125.45 is 3.6% for the $1\omega$ pulse shape and 5.3% for the $3\omega$ pulse shape. Table 125.IV shows that the measured and predicted beamline energies calculated using the pulse-shape prediction tool agree to within ~3%.

Simulated $1\omega$ beamline output energies are compared with measurements in Fig. 125.46 for ~70 target shots taken during the third and fourth quarters of FY10. The simulations in Fig. 125.46 were performed using a 1-k × 1-k grid and 22 temporal slices and required ~7 min each. To avoid the additional computing time required for the temporal integration in the IR section of the beamline, a continuous-wave (cw) amplification model is also available. Figure 125.47(a) compares simulated, $1\omega$ beamline output energies with measured energies using the cw model; Fig. 125.47(b) shows the corresponding $3\omega$ on-target

Table 125.IV: Simulated and measured beamline output energies for Beamline 3 (shot 7799) using the pulse-shape–prediction tool. The regen pulse shape for a qualification shot taken on the same day was used in the simulation.

| | Simulation | Measurement |
|---|---|---|
| IR (J) | 1375 | 1416 |
| UV on-target (J) | 442 | 454 |

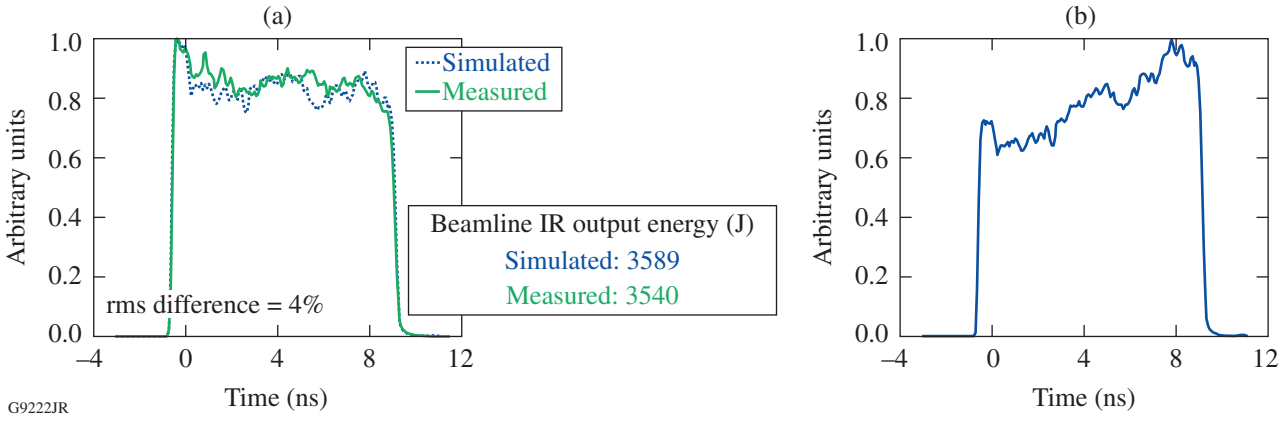


Figure 125.44
Simulated and measured ESG9901 square-pulse shapes are shown in (a) for the $1\omega$ output of Beamline 4. Beamline energies and the rms difference between simulated and measured pulse shapes are given in the figure. Simulations used the regen output pulse shape shown in (b) for an injection shot taken on the same day.

energies. In this case, the 3$\omega$ simulations used measured IR beamline output-pulse shapes. The agreement between the simulations and measurements is within ~5%, although an ~5% systematic offset is apparent in the region between 2 to 3 kJ in Figs. 125.46 and 125.47(a) and between 1 to 1.2 kJ in Fig. 125.47(b). This is suspected to be caused by a temporary calibration drift in the energy diagnostic used for these shots. These results demonstrate the model's capability to accurately predict beamline energy and pulse shape using the measured qualification shot data.

Simulated 3$\omega$ peak fluences for shots on OMEGA EP using a 1-k × 1-k grid and 22 temporal slices are compared with their corresponding measured values in Fig. 125.48. The simulated values are, on average, ~9% below the measurements and are generally well within 20%. The difference between the 9% and 20% levels corresponds to the 2-$\sigma$ distance for the fluence distribution formed by the difference between simulated and measured values. The systematic offset of the simulated peak fluence from the measured values suggests that allowable 3$\omega$ energies can be safely established using simulations that provide peak fluences less than or equal to 80% of the 3$\omega$ damage threshold. For OMEGA EP users requesting maximum 3$\omega$ energy on the first target shot of the day, the maximum-allowable energy is calculated in a two-step process: Prior to shot day, the 3$\omega$ energy limit is established based on the amount of modulation observed in the most recently measured 3$\omega$ near-field beam. This enables users to specify the entire laser configuration well in advance of the shot. On shot day, the maximum-allowable 3$\omega$ energy is calculated using the measured injected near-field beam to give a simulated peak fluence that is equal to 80% of the 3$\omega$ damage threshold. Simulations on shot day account for (1) changes in the injected near-field beam and (2) possible differences between the pre-shot-day and current-shot-day beamline configurations that may affect

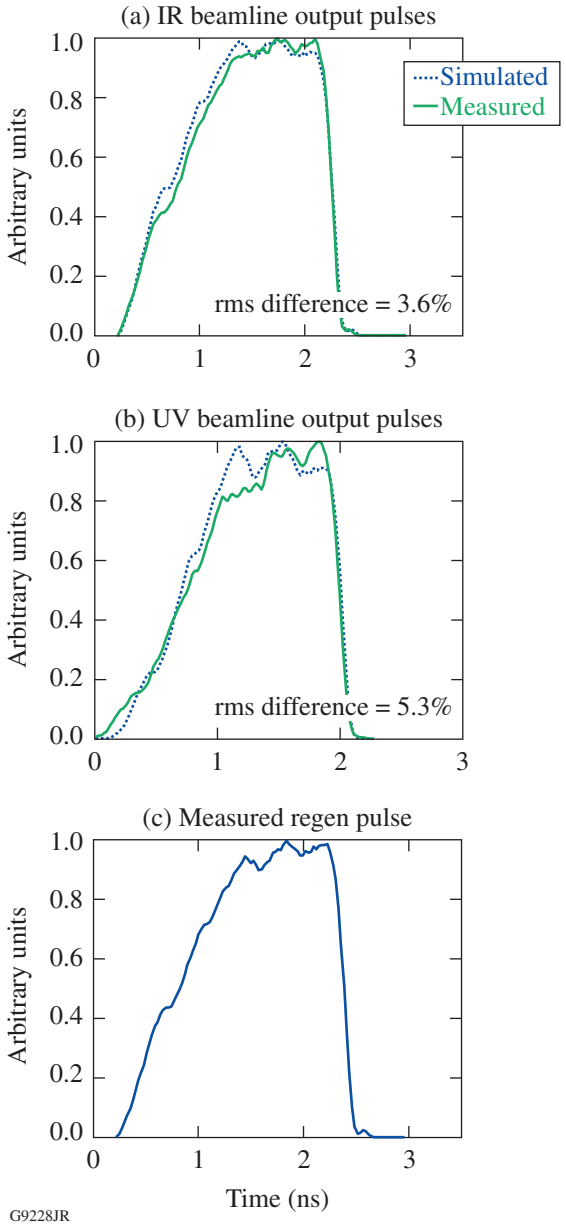


Figure 125.45
Simulated and measured ERM2001 ramped-pulse shapes are shown in (a) and (b) for Beamline 3's 1$\omega$ and 3$\omega$ outputs, respectively. The rms differences between simulated and measured pulse shapes are given in the figure. Simulations used the regen output-pulse shape shown in (c) for an injection shot taken on the same day.

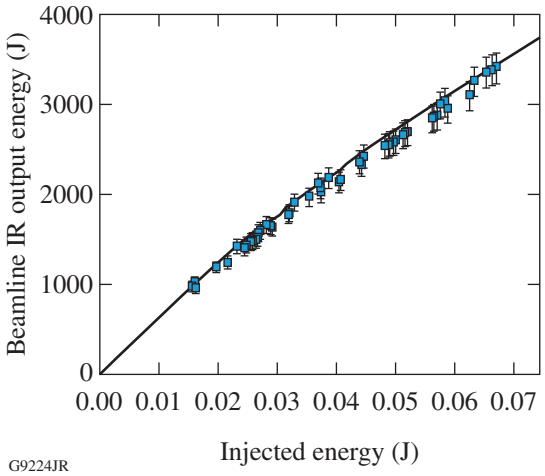


Figure 125.46
Simulated (line) and measured 1$\omega$ output energy versus injected energy of Beamline 4 with 16 laser slabs (9/7 main/booster amplifier configuration). Measurements represent the approximately 70 target shots taken during the third and fourth quarters of FY10.

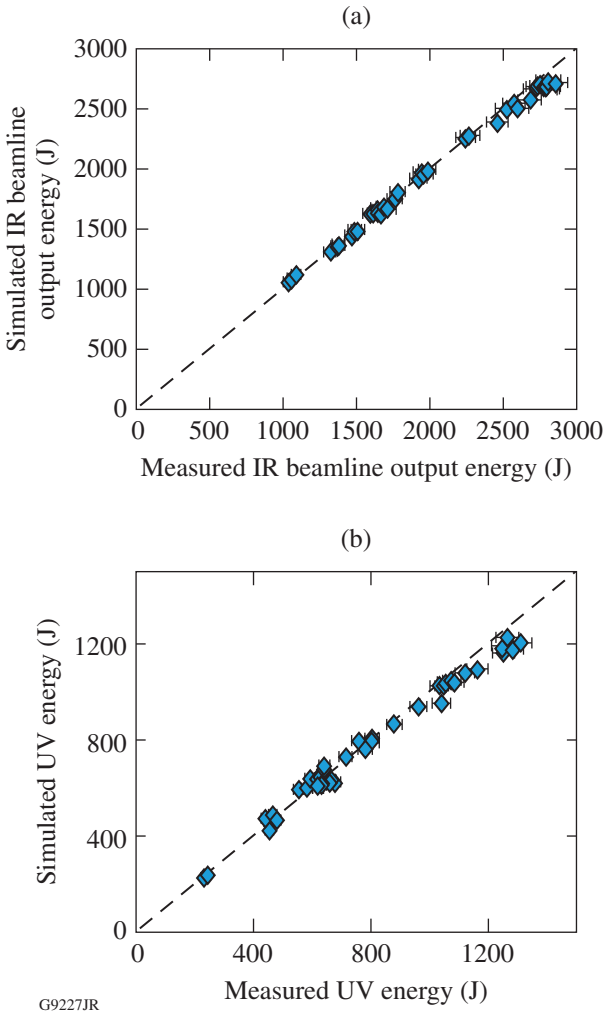


Figure 125.47
Simulated energies using the cw IR and UV beamline models versus measured energies: (a) 1$\omega$ Beamline 3 output and (b) corresponding 3$\omega$ on-target energy. The dashed line with slope of 1 is shown for reference.

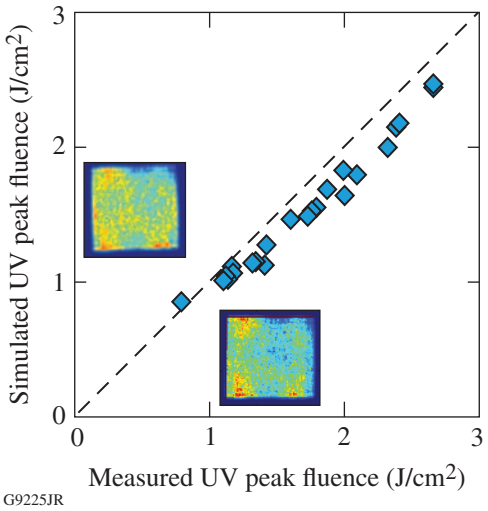


Figure 125.48
3$\omega$ peak fluence simulated by using the measured injected near-field beam is plotted against the corresponding measured peak fluence for several OMEGA EP target shots. A simulated and corresponding measured 3$\omega$ beam is also shown for one case. Simulated values were ~9% below measurements, on average (dashed line with slope of 1 is shown for reference). By characterizing the model's predictive capability, high-resolution, end-to-end beamline simulations were performed and facility direction provided to operators within a qualification shot cycle.

UV near-field modulation. This two-step process provides a shot-ready laser configuration and ensures that 3$\omega$ damage thresholds are not exceeded. Typically, only small adjustments to the injection-energy throttle setting are required to achieve, on the first shot, measured 3$\omega$ peak fluences that are between 85% and 95% of the 3$\omega$ damage threshold. Notably, no significant damage has been observed to date in the long-pulse section of the OMEGA EP beamlines.

## Summary

We have described several performance enhancements in the long-pulse section of OMEGA EP that have resulted in better beam quality, greater reliability, and improved efficiency during shot operations. The sensitivity to front-end, near-field beam quality that results from operation in a regime of low saturation has been reduced using new apodizer designs. These designs have significantly improved the near-field beam profile and reduced the time required to qualify the injected beam. Other methods to reduce beam modulation, such as FCC detuning and the implementation of a PSLIM, are also being pursued. We have described simulation tools used during shot operations that have provided rapid and accurate predictions of beamline performance, ensuring that laser-damage thresholds are not exceeded and providing facility direction to operators within a qualification shot cycle. Higher-damage-threshold UV transport optics have also been procured. Higher energies will allow for greater saturation, greater levels of beam smoothing, and greater on-target energy for a given peak fluence.

## ACKNOWLEDGMENT

The authors thank the OMEGA EP operations team for their contributions to the measurements reported here. This work was supported by the U.S. Department of Energy Office of Inertial Confinement Fusion under Cooperative Agreement No. DE-FC52-08NA28302, the University of Rochester, and the New York State Energy Research and Development Authority. The support of DOE does not constitute an endorsement by DOE of the views expressed in this article.

## REFERENCES


1. J. H. Kelly, L. J. Waxer, V. Bagnoud, I. A. Begishev, J. Bromage, B. E. Kruschwitz, T. J. Kessler, S. J. Loucks, D. N. Maywar, R. L. McCrory, D. D. Meyerhofer, S. F. B. Morse, J. B. Oliver, A. L. Rigatti, A. W. Schmid, C. Stoeckl, S. Dalton, L. Folnsbee, M. J. Guardalben, R. Jungquist, J. Puth, M. J. Shoup III, D. Weiner, and J. D. Zuegel, J. Phys. IV France **133**, 75 (2006).

2. T. Alger *et al.*, Lawrence Livermore National Laboratory, Livermore, CA, Report UCRL-ID-132680 (NIF-0014142), NTIS Order No. DE2002-791837 (1999). (Copies may be obtained from the National Technical Information Service, Springfield, VA 22161.)

3. Estimated to be 4 J/cm$^2$ with a 3-ns Gaussian pulse.

4. I. L. Bass *et al.*, in *High-Power Laser Ablation VI*, edited by C. R. Phipps (SPIE, Bellingham, WA, 2006), Vol. 6261, p. 62612A.

5. T. I. Suratwala *et al.*, "HF-Based Etching Processes for Improving Laser Damage Resistance of Fused Silica Optical Surfaces," to be published in the Journal of the American Ceramic Society.

6. See Fig. 1 of Ref. 5.

7. C. Dorrer and J. D. Zuegel, J. Opt. Soc. Am. B **24**, 1268 (2007).

8. R. S. Craxton, IEEE J. Quantum Electron. **QE-17**, 1771 (1981).

9. V. Bagnoud and J. D. Zuegel, Opt. Lett. **29**, 295 (2004).

10. S.-W. Bahk, E. Fess, B. E. Kruschwitz, and J. D. Zuegel, Opt. Express **18**, 9151 (2010).

11. L. M. Frantz and J. S. Nodvik, J. Appl. Phys. **34**, 2346 (1963).

# Publications and Conference Presentations

## Publications

B. Ciftcioglu, J. Zhang, R. Sobolewski, and H. Wu, "An 850-nm Normal-Incidence Germanium Metal–Semiconductor–Metal Photodetector With 13-GHz Bandwidth and 8-$\mu$A Dark Current," IEEE Photon. Technol. Lett. **22**, 1850 (2010).

A. S. Cross, J. P. Knauer, A. Mycielski, D. Kochanowska, M. Wiktowska-Baran, R. Jakieła, J. Domagała, Y. Cui, R. B. James, and R. Sobolewski, "(Cd,Mn)Te Detectors for Characterization of X-Ray Emissions Generated During Laser-Driven Fusion Experiments," Nucl. Instrum. Methods Phys. Res. A **624**, 649 (2010).

V. Yu. Glebov, T. C. Sangster, C. Stoeckl, J. P. Knauer, W. Theobald, K. L. Marshall, M. J. Shoup III, T. Buczek, M. Cruz, T. Duffy, M. Romanofsky, M. Fox, A. Pruyne, M. J. Moran, R. A. Lerche, J. McNaney, J. D. Kilkenny, M. J. Eckart, D. Schneider, D. Munro, W. Stoeffl, R. A. Zacharias, J. J. Haslam, T. Clancy, M. Yeoman, D. Warwas, C. J. Horsfield, J.-L. Bourgade, O. Landoas, L. Disdier, G. A. Chandler, and R. J. Leeper, "The National Ignition Facility Neutron Time-of-Flight System and Its Initial Performance," Rev. Sci. Instrum. **81**, 10D325 (2010) (invited).

S. X. Hu, V. N. Goncharov, P. B. Radha, J. A. Marozas, S. Skupsky, T. R. Boehly, T. C. Sangster, D. D. Meyerhofer, and R. L. McCrory, "Two-Dimensional Simulations of the Neutron-Yield in Cryogenic Deuterium-Tritium Implosions on OMEGA," Phys. Plasmas **17**, 102706 (2010).

I. V. Igumenshchev, D. H. Edgell, V. N. Goncharov, J. A. Delettrez, A. V. Maximov, J. F. Myatt, W. Seka, A. Shvydky, S. Skupsky, and C. Stoeckl, "Crossed-Beam Energy Transfer in Implosion Experiments on OMEGA," Phys. Plasmas **17**, 122708 (2010).

V. Kaushal, I. Iñiguez-de-la-Torre, H. Irie, G. Guarino, W. R. Donaldson, P. Ampadu, R. Sobolewski, and M. Margala, "A Study of Geometry Effects on the Performance of Ballistic Deflection Transistors," IEEE Trans. Nanotech. **9**, 723 (2010).

F. J. Marshall, T. DeHaas, and V. Yu. Glebov, "Charge-Injection-Device Performance in the High-Energy-Neutron Environment of Laser-Fusion Experiments," Rev. Sci. Instrum. **81**, 10E503 (2010).

P. M. Nilson, A. A. Solodov, J. F. Myatt, W. Theobald, P. A. Jaanimagi, L. Gao, C. Stoeckl, R. S. Craxton, J. A. Delettrez, B. Yaakobi, J. D. Zuegel, B. E. Kruschwitz, C. Dorrer, J. H. Kelly, K. U. Akli, P. K. Patel, A. J. Mackinnon, R. Betti, T. C. Sangster, and D. D. Meyerhofer, "Scaling Hot-Electron Generation to High-Power, Kilojoule-Class Laser-Solid Interactions," Phys. Rev. Lett. **105**, 235001 (2010).

S. Papernov, A. Tait, W. Bittle, A. W. Schmid, J. B. Oliver, and P. Kupinski, "Submicrometer-Resolution Mapping of Ultraweak 355-nm Absorption in $HfO_2$ Monolayers Using Photothermal Heterodyne Imaging," in *Laser-Induced Damage in Optical Materials: 2010*, edited by G. J. Exarhos, V. E. Gruzdev, J. A. Menapace, D. Ristau, and M. J. Soileau (SPIE, Bellingham, WA, 2010), Vol. 7842, Paper 78420A.

J. S. Ross, S. H. Glenzer, J. P. Palastro, B. B. Pollock, D. Price, G. R. Tynan, and D. H. Froula, "Thomson-Scattering Measurements in the Collective and Noncollective Regimes in Laser Produced Plasmas," Rev. Sci. Instrum. **81**, 10D523 (2010) (invited).

C. Stoeckl, M. Cruz, V. Yu. Glebov, J. P. Knauer, R. Lauck, K. Marshall, C. Mileham, T. C. Sangster, and W. Theobald, "A Gated Liquid-Scintillator-Based Neutron Detector for Fast-Ignitor Experiments and Down-Scattered Neutron Measurements," Rev. Sci. Instrum. **81**, 10D302 (2010).

W. Theobald, V. Ovchinnikov, S. Ivancic, B. Eichman, P. M. Nilson, J. A. Delettrez, R. Yan, G. Li, F. J. Marshall, D. D. Meyerhofer, J. F. Myatt, C. Ren, T. C. Sangster, C. Stoeckl, J. D. Zuegel, L. Van Woerkom, R. R. Freeman, K. U. Akli, E. Giraldez, and R. B. Stephens, "High-Intensity Laser-Plasma Interaction with Wedge-Shaped-Cavity Targets," Phys. Plasmas **17**, 103101 (2010).

## Forthcoming Publications

W. R. Donaldson, D. N. Maywar, J. H. Kelly, and R. E. Bahr, "Measurement of the Self-Phase-Modulation–Induced Bandwidth in a 30-kJ-Class Laser Amplifier Chain," to be published in the Journal of the Optical Society of America B.

D. H. Froula, S. H. Glenzer, N. C. Luhmann, and J. Sheffield, "Plasma Scattering of Electromagnetic Radiation: Theory and Measurement Techniques," to be published by Elsevier.

J. B. Oliver, P. Kupinski, A. L. Rigatti, A. W. Schmid, J. C. Lambropoulos, S. Papernov, A. Kozlov, J. Spaulding, D. Sadowski, Z. R. Chrzan, R. D. Hand, D. R. Gibson, I. Brinkley, and F. Placido, "Large-Aperture Plasma-Assisted Deposition of Inertial Confinement Fusion Laser Coatings," to be published in Applied Optics.

P. B. Radha, R. Betti, T. R. Boehly, J. A. Delettrez, V. N. Goncharov, I. V. Igumenshchev, J. P. Knauer, J. A. Marozas, F. J. Marshall, R. L. McCrory, D. D. Meyerhofer, S. P. Regan, T. C. Sangster, W. Seka, S. Skupsky, A. A. Solodov, C. Stoeckl, W. Theobald, J. A. Frenje, D. T. Casey, C. K. Li, and R. D. Petrasso, "Inertial Confinement Fusion Using the OMEGA Laser System," to be published in IEEE Transactions on Plasma Science.

P. B. Radha, C. Stoeckl, V. N. Goncharov, J. A. Delettrez, J. A. Frenje, I. V. Igumenshchev, J. P. Knauer, J. A. Marozas, R. L. McCrory, D. D. Meyerhofer, R. D. Petrasso, S. P. Regan, T. C. Sangster, W. Seka, and S. Skupsky, "Triple-Picket Warm Plastic-Shell Implosions on OMEGA," to be published in Physics of Plasmas.

W. Wang, T. B. Jones, and D. R. Harding, "On-Chip Double Emulsion Droplet Assembly Using Electrowetting-on-Dielectric and Dielectrophoresis," to be published in Fusion Science and Technology.

## Conference Presentations

S. P. Regan, R. Epstein, T. C. Sangster, D. D. Meyerhofer, B. A. Hammel, H. A. Scott, D. K. Bradley, D. Callahan, M. J. Edwards, M. J. Eckart, S. H. Glenzer, J. D. Kilkenny, O. L. Landen, N. B. Meezan, R. Prasad, V. A. Smalyuk, L. J. Suter, and R. C. Mancini, "Hydrodynamic Mix Experiments for NIF Implosions Based on Spectroscopic Observations of K-Shell Emission," 14th International Workshop on Radiative Properties of Hot Dense Matter, Marbella, Spain, 4–8 October 2010.

D. D. Meyerhofer, R. L. McCrory, R. Betti, T. R. Boehly, D. T. Casey, T. J. B. Collins, R. S. Craxton, J. A. Delettrez, D. H. Edgell, R. Epstein, K. A. Fletcher, J. A. Frenje, V. Yu. Glebov, V. N. Goncharov, D. R. Harding, S. X. Hu, I. V. Igumenshchev, J. P. Knauer, C. K. Li, J. A. Marozas, F. J. Marshall, P. W. McKenty, P. M. Nilson, S. P. Padalino, R. D. Petrasso, P. B. Radha, S. P. Regan, T. C. Sangster, F. H. Séguin, W. Seka, R. W. Short, D. Shvarts, S. Skupsky, J. M. Soures, C. Stoeckl, W. Theobald, and B. Yaakobi, "High-Performance Inertial Confinement Fusion Target Implosions on OMEGA," 23rd IAEA Fusion Energy Conference, Daejon, Korea, 11–16 October 2010.

W. Theobald, A. A. Solodov, C. Stoeckl, K. S. Anderson, R. Betti, T. R. Boehly, R. S. Craxton, J. A. Delettrez, J. A. Frenje, V. Yu. Glebov, H. Habara, F. J. Marshall, K. A. Tanaka, K. L. Marshall, D. D. Meyerhofer, P. M. Nilson, P. K. Patel, H. Chen, T. C. Sangster, W. Seka, N. Sinenian, F. Beg, and R. B. Stephens, "Fast-Ignition Integrated Experiments on OMEGA," 11th International Workshop on Fast Ignition of Fusion Targets, Shanghai, China, 17–21 October 2010.

J. H. Kelly and T. Z. Kosc, "Modeling the OMEGA Laser System at the University of Rochester Using Miró," 5th Miró User Meeting, Haut Carré, Talence, France, 18–19 October 2010.

W. Theobald, A. A. Solodov, C. Stoeckl, K. S. Anderson, R. Betti, T. R. Boehly, R. S. Craxton, J. A. Delettrez, J. A. Frenje, V. Yu. Glebov, H. Habara, K. A. Tanaka, F. J. Marshall, K. L. Marshall, D. D. Meyerhofer, P. M. Nilson, P. K. Patel, H. Chen, T. C. Sangster, W. Seka, N. Sinenian, F. Beg, and

R. B. Stephens, "Fast-Ignition Research at LLE," Japan–U.S. Ignitor and High Energy Density Physics Workshop, Osaka, Japan, 23–24 October 2010.

---

The following presentations were made at Frontiers in Optics, Rochester, NY, 24–28 October 2010:

L. Ji, W. R. Donaldson, and T. Y. Hsiang, "The Stability of the Active Mode-Locked Erbium-Doped Fiber Laser and Its Application in a Novel Electro-Optic Sampling System."

T. J. Kessler, H. Huang, J. B. Oliver, A. L. Rigatti, S. D. Jacobs, A. W. Schmid, and A. Kozlov, "Grating Development for High-Peak-Power CPA Laser Systems."

J. P. Leidner and J. R. Marciante, "Non-Adiabatically Tapered Multimode Interference Coupler for High-Power Single-Mode Semiconductor Lasers."

D. D. Meyerhofer, V. N. Goncharov, R. Betti, T. R. Boehly, T. J. B. Collins, R. S. Craxton, J. A. Delettrez, D. H. Edgell, R. Epstein, V. Yu. Glebov, D. R. Harding, S. X. Hu, I. V. Igumenshchev, J. P. Knauer, S. J. Loucks, J. A. Marozas, F. J. Marshall, R. L. McCrory, P. W. McKenty, P. M. Nilson, P. B. Radha, S. P. Regan, T. C. Sangster, W. Seka, R. W. Short, D. Shvarts, S. Skupsky, V. A. Smalyuk, J. M. Soures, C. Stoeckl, W. Theobald, B. Yaakobi, J. A. Frenje, D. T. Casey, C. K. Li, R. D. Petrasso, F. H. Séguin, S. P. Padalino, and K. A. Fletcher, "Inertial Confinement Fusion Research at the Laboratory for Laser Energetics."

J. Qiao, A. Kalb, T. Nguyen, D. Canning, and J. Price, "Development and Operation of Large-Aperture Tiled-Grating Compressors for High-Energy, Petawatt-Class Laser Systems."

J. E. Schoenly, W. Seka, and P. Rechmann, "Selective Near-UV Laser Ablation of Subgingival Dental Calculus at a 20° Irradiation Angle."

---

The following presentations were made at the 9th International Conference on Tritium Science and Technology, Nara, Japan, 24–29 October 2010:

J. E. Fair and W. T. Shmayda, "A Model for Removal of Surface-Bound Tritium Using Humid Air."

W. T. Shmayda and J. E. Fair, "Tritium Outgassing from Contaminated Metal Surfaces."

W. T. Shmayda, D. R. Harding, S. J. Brereton, and F. Javier, "Tritium Inertial Fusion: Extrapolation to Ignition Machines."

---

The following presentations were made at the 52nd Annual Meeting of the APS Division of Plasma Physics, Chicago, IL, 8–12 November 2010:

K. S. Anderson, R. Betti, R. S. Craxton, R. Nora, and L. J. Perkins, "A Plastic-Ablator Cryogenic Shock-Ignition Design for the NIF."

M. A. Barrios, D. E. Fratanduono, T. R. Boehly, D. D. Meyerhofer, D. G. Hicks, P. M. Celliers, and J. H. Eggert, "Precision Measurements of the Equation of State (EOS) of GDP Ablator Materials at ~1 to 10 Mbar Using Laser-Driven Shock Waves."

T. R. Boehly, M. A. Barrios, D. E. Fratanduono, V. N. Goncharov, S. X. Hu, T. J. B. Collins, J. A. Marozas, T. C. Sangster, D. D. Meyerhofer, P. M. Celliers, H. F. Robey, D. G. Hicks, J. H. Eggert, G. W. Collins, and R. Smith, "Shock-Timing Measurements in ICF Targets Filled with Cryogenic Deuterium."

D. T. Casey, J. A. Frenje, F. H. Séguin, M. Manuel, N. Sinenian, R. D. Petrasso, V. Yu. Glebov, P. B. Radha, T. C. Sangster, D. D. Meyerhofer, D. McNabb, A. Miles, P. Navratil, and S. Quaglioni, "Measurements of Down-Scattered and TT-Neutron Spectra Using the Magnetic Recoil Spectrometer (MRS) on OMEGA."

P. Y. Chang, G. Fiksel, M. Hohenberger, J. P. Knauer, R. Nora, R. Betti, F. H. Séguin, C. K. Li, M.-J. E. Manuel, and R. D. Petrasso, "Magnetized Spherical Implosions on the OMEGA Laser."

T. J. B. Collins, J. A. Marozas, S. Skupsky, P. W. McKenty, V. N. Goncharov, P. B. Radha, A. Shvydky, and M. M. Marinak, "Preparing for Polar Drive at the National Ignition Facility."

R. S. Craxton, L. Tucker, T. Mo, K. S. Anderson, R. Betti, L. J. Perkins, G. P. Schurtz, X. Ribeyre, and A. Casner, "A 96/96-Beam Polar-Drive Configuration for Shock Ignition on the NIF."

J. A. Delettrez, S. X. Hu, and A. Shvydky, "Numerical Investigation of the Effect of Two-Plasmon-Decay Preheat in Planar Rayleigh–Taylor Experiments."

D. H. Edgell, J. Magoon, T. C. Sangster, M. J. Shoup III, F. J. Marshall, C. Stoeckl, A. G. MacPhee, S. Burns, J. Celeste, M. J. Eckart, J. D. Kilkenny, J. Kimbrough, J. Parker, and T. Thomas, "South-Pole Bang-Time X-Ray Diagnostic for the NIF."

R. Epstein, S. P. Regan, F. J. Marshall, J. A. Delettrez, V. N. Goncharov, S. X. Hu, P. W. McKenty, G. Liu, D. D. Meyerhofer, P. B. Radha, T. C. Sangster, C. Stoeckl, W. Theobald, R. Tommasini, N. Landen, and A. J. MacKinnon, "Hard X-Ray Compton Radiography of Cryogenic Implosions on OMEGA."

G. Fiksel, R. Jungquist, C. Mileham, P. M. Nilson, W. Theobald, and C. Stoeckl, "Development of a Spherical Crystal X-Ray-Imaging Diagnostic for OMEGA and OMEGA EP."

D. E. Fratanduono, M. A. Barrios, T. R. Boehly, D. D. Meyerhofer, J. H. Eggert, R. Smith, D. G. Hicks, P. M. Celliers, and G. W. Collins, "The Refractive Index and Transparency of Lithium Fluoride Compressed to 800 GPa."

J. A. Frenje, D. T. Casey, C. K. Li, F. H. Séguin, R. D. Petrasso, R. Bionta, C. Cerjan, M. Eckart, S. W. Haan, S. P. Hatchett, H. Kather, J. D. Kilkenny, O. L. Landen, A. J. MacKinnon, M. J. Moran, J. R. Rygg, V. Yu. Glebov, T. C. Sangster, D. D. Meyerhofer, K. Fletcher, and R. Leeper, "First Measurements of the Absolute Neutron Spectrum Using the Magnetic Recoil Spectrometer (MRS) at the NIF."

D. H. Froula, V. N. Goncharov, S. X. Hu, J. F. Myatt, J. S. Ross, L. Divol, and S. H. Glenzer, "Ion-Acoustic Wave Instability from Laser-Driven Return Currents."

L. Gao, P. M. Nilson, W. Theobald, C. Stoeckl, C. Dorrer, T. C. Sangster, D. D. Meyerhofer, L. Willingale, and K. M. Krushelnick, "Measurements of Proton Generation with Intense, Kilojoule Laser Pulses on OMEGA EP."

V. Yu. Glebov, J. P. Knauer, T. C. Sangster, C. Stoeckl, E. J. Bond, J. A. Caggiano, T. J. Clancy, M. J. Eckart, J. D. Kilkenny, R. A. Lerche, J. McNaney, M. J. Moran, and D. H. Munro, "Neutron Time-of-Flight Diagnostic Performance During the National Ignition Facility's 2010 Campaign."

V. N. Goncharov, "Low-Adiabat, High-Compression Cryogenic Deuterium–Tritium Implosions on OMEGA" (invited).

M. Hohenberger, W. Theobald, S. X. Hu, K. S. Anderson, D. D. Meyerhofer, C. Stoeckl, T. R. Boehly, D. E. Fratanduono, R. Betti, A. Casner, X. Ribeyre, and G. Schurtz, "Shock-Ignition Studies on OMEGA."

S. X. Hu, V. N. Goncharov, T. R. Boehly, S. Skupsky, T. C. Sangster, D. D. Meyerhofer, and R. L. McCrory, "The Equation-of-State Dependence of Nonuniformity Growth in Cryogenic-DT Implosions on OMEGA."

I. V. Igumenshchev, V. N. Goncharov, P. M. Nilson, T. C. Sangster, C. K. Li, R. D. Petrasso, and M. G. Haines, "Study of Self-Generated Magnetic Fields in Implosion Experiments on OMEGA."

M. Manuel, C. K. Li, F. H. Séguin, J. A. Frenje, D. T. Casey, N. Sinenian, R. D. Petrasso, R. Betti, V. A. Smalyuk, J. Hager, and R. P. J. Town, "Using Proton Radiography to Measure Rayleigh–Taylor-Induced Magnetic Fields."

J. A. Marozas, T. J. B. Collins, and J. D. Zuegel, "Smoothing by Spectral Dispersion (SSD) for Multiple-Picket Pulses on OMEGA and the NIF."

F. J. Marshall, V. Yu. Glebov, P. W. McKenty, P. B. Radha, and A. Shvydky, "NIF-Relevant, Polar-Drive Irradiation Tests on OMEGA."

A. V. Maximov, J. F. Myatt, R. W. Short, W. Seka, and R. Yan, "Two-Plasmon-Decay Instability and Stimulated Brillouin Scattering in Direct-Drive ICF Plasmas."

P. W. McKenty, R. S. Craxton, F. J. Marshall, A. Shvydky, R. Epstein, A. M. Cok, J. A. Marozas, T. J. B. Collins, S. Skupsky, C. Stoeckl, T. C. Sangster, M. J. Bonino, R. T. Janezik, D. R. Harding, W. T. Shmayda, S. F. B. Morse, D. D. Meyerhofer, R. L. McCrory, A. Nikroo, J. D. Kilkenny, M. L. Hoppe, J. Fooks, A. J. MacKinnon, R. J. Wallace, D. K. Bradley, and G. A. Kyrala, "Evaluation of the First Polar-Drive, DT-Gas–Filled Target Implosions on the NIF."

D. D. Meyerhofer, S.-W. Bahk, J. Bromage, C. Dorrer, J. H. Kelly, B. E. Kruschwitz, S. J. Loucks, R. L. McCrory, S. F. B. Morse, J. Qiao, C. Stoeckl, and L. J. Waxer, "Status of the OMEGA EP Laser System."

J. F. Myatt, J. A. Delettrez, A. V. Maximov, R. W. Short, D. H. Edgell, W. Seka, D. F. Dubois, D. A. Russell, and H. X. Vu, "Two-Plasmon-Decay Preheat Calculations for OMEGA and Ignition-Scale Direct-Drive Inertial Confinement Fusion."

P. M. Nilson, A. A. Solodov, J. F. Myatt, W. Theobald, P. A. Jaanimagi, L. Gao, C. Stoeckl, R. S. Craxton, J. A. Delettrez, J. D. Zuegel, B. E. Kruschwitz, C. Dorrer, J. H. Kelly, K. U. Akli, P. K. Patel, A. J. MacKinnon, R. Betti, T. C. Sangster, and D. D. Meyerhofer, "Scaling Hot-Electron Generation to Long-Pulse, High-Intensity Laser–Solid Interactions" (invited).

R. Nora, R. Betti, K. S. Anderson, P. Y. Chang, and M. Hohenberger, "One-Dimensional Hydrodynamic Theory of Shock Ignition."

P. B. Radha, C. Stoeckl, J. P. Knauer, V. N. Goncharov, I. V. Igumenshchev, R. L. McCrory, D. D. Meyerhofer, T. C. Sangster, S. Skupsky, J. A. Frenje, and R. D. Petrasso, "The Effect of Nonuniformity Growth on Direct-Drive Plastic-Shell Implosions on the OMEGA Laser."

S. P. Regan, R. Epstein, T. C. Sangster, D. D. Meyerhofer, B. A. Hammel, H. A. Scott, D. K. Bradley, D. Callahan, M. J. Edwards, M. J. Eckart, S. H. Glenzer, J. D. Kilkenny, O. L. Landen, N. B. Meezan, R. Prasad, V. A. Smalyuk, and L. J. Suter, "Spectroscopic Observations of Ablator Mass Mixed into the Hot Spot of NIF Implosions."

H. Rinderknecht, "A CVD Diamond-Based Proton-Bang-Time Detector for OMEGA and the NIF."

M. Rosenberg, "Yield and Ion-Temperature Measurements in Exploding Pusher Experiments on OMEGA and the NIF."

T. C. Sangster, V. N. Goncharov, R. Betti, T. R. Boehly, J. A. Delettrez, D. H. Edgell, V. Yu. Glebov, S. X. Hu, J. P. Knauer, F. J. Marshall, R. L. McCrory, P. W. McKenty, D. D. Meyerhofer, P. B. Radha, S. P. Regan, S. Seka, S. Skupsky, C. Stoeckl, B. Yaakobi, J. A. Frenje, and D. T. Casey, "Areal Density and Ion-Temperature Measurements in Cryogenic-DT Implosions on OMEGA."

W. Seka, D. H. Froula, D. H. Edgell, R. E. Bahr, J. F. Myatt, J. A. Delettrez., R. S. Craxton, S. X. Hu, A. V. Maximov, and R. W. Short, "Competitive Laser–Plasma Interaction Processes Near Quarter Critical Relevant to Direct-Drive ICF."

R. W. Short, "Angular Dependence of Two-Plasmon Decay in Multibeam Direct-Drive Irradiation Geometries."

A. Shvydky, P. W. McKenty, F. J. Marshall, R. S. Craxton, J. A. Marozas, R. Epstein, S. Skupsky, and R. L. McCrory, "Numerical Investigation of NIF Diagnostic Commissioning Experiments on OMEGA."

N. Sinenian, J. A. Frenje, R. D. Petrasso, F. H. Séguin, C. K. Li, W. Theobald, and C. Stoeckl, "Observation of Fast Protons in Recent Electron Fast-Ignition Experiments on OMEGA."

A. A. Solodov, R. Betti, K. S. Anderson, J. F. Myatt, W. Theobald, and C. Stoeckl, "Controlling the Divergence of Laser-Generated Fast Electrons Through Resistivity Gradients in Fast-Ignition Targets."

C. Stoeckl, D. H. Edgell, C. Forrest, V. Yu. Glebov, J. P. Knauer, and T. C. Sangster, "Monte Carlo Simulations of Neutron Scattering in Current-Mode Neutron Time-of-Flight Detectors."

W. Theobald, A. A. Solodov, C. Stoeckl, K. S. Anderson, R. Betti, T. R. Boehly, R. S. Craxton, J. A. Delettrez, C. Dorrer, J. A. Frenje, V. Yu. Glebov, H. Habara, K. A. Tanaka, J. P. Knauer, F. J. Marshall, K. L. Marshall, D. D. Meyerhofer, P. M. Nilson, P. K. Patel, H. Chen, T. C. Sangster, W. Seka, N. Sinenian, T. Ma, F. N. Beg, E. Giraldez, and R. B. Stephens, "Initial Cone-in-Shell Target Fast-Ignition Experiments on OMEGA" (invited).

R. Yan, A. V. Maximov, and C. Ren, "Saturation of Two-Plasmon-Decay and Ion-Density Fluctuations."

---

D. D. Meyerhofer, K. S. Anderson, S.-W. Bahk, R. Betti, T. R. Boehly, J. Bromage, R. S. Craxton, C. Dorrer, J. A. Delettez, L. Gao, V. Yu. Glebov, P. A. Jaanimagi, J. H. Kelly, B. E. Kruschwitz, S. J. Loucks, F. J. Marshall, K. L. Marshall, R. L. McCrory, S. F. B. Morse, J. F. Myatt, P. M. Nilson, J. Qiao, T. C. Sangster, W. Seka, A. A. Solodov, C. Stoeckl, L. J. Waxer, W. Theobald, B. Yaakobi, J. D. Zuegel, J. A. Frenje, N. Sinenian, H. Habara, K. A. Tanaka, A. J. MacKinnon, H. Chen, P. K. Patel, F. N. Beg, T. Ma, K. U. Akli, R. B. Stephens, L. Willingale, and K. M. Krushelnick, "Initial Experiments on the OMEGA EP High-Energy Petawatt Laser System," International Symposium on Chirped Pulse Amplification, Quebec City, Canada, 17–21 November 2010.

---

D. R. Harding, T. B. Jones, Z. Bei, W. Wang, S. H. Chen, R. Q. Gram, M. Moynihan, and G. Randall, "Microfluidic Methods for Producing Millimeter-Size Fuel Capsules for Inertial Fusion," 2010 Materials Research Society Fall Meeting, Boston, MA, 29 November–3 December 2010.

J. M. Soures and R. L. McCrory, "The University of Rochester's Laboratory for Laser Energetics' Role in Inertial Fusion Energy Development," 31st Fusion Power Associates Annual Meeting and Symposium, Washington, DC, 1–2 December 2010.


1850
MELIORA
UNIVERSITY of
ROCHESTER